

Dissertation zur Erlangung des Doktorgrades

DER FAKULTÄT FÜR CHEMIE UND PHARMAZIE
DEPARTMENT CHEMIE UND BIOCHEMIE
DER LUDWIG-MAXIMILIANS-UNIVERSITÄT MÜNCHEN

**Application of density functional theory
and the random phase approximation
under periodic boundary conditions
employing Gaussian-type basis functions**

Martin Manfred Jakob Grundei

aus

Rosenheim, Deutschland

2023

Erklärung

Diese Dissertation wurde im Sinne von § 7 der Promotionsordnung vom 28.11.2011 von Herrn Prof. Dr. Christian Ochsenfeld betreut.

Eidesstattliche Versicherung

Diese Dissertation wurde eigenständig und ohne unerlaubte Hilfe erarbeitet.

Martin Grundei

München, den 29.05.2023

Dissertation eingereicht am: 23.02.2023

Erstgutachter: Prof. Dr. Christian Ochsenfeld

Zweitgutachter: Prof. Dr. Hubert Ebert

Mündliche Prüfung am: 24.05.2023

Danksagung

Diese Arbeit wurde am Department Chemie der Ludwig-Maximilians-Universität München im Arbeitskreis von Herrn Prof. Dr. Christian Ochsenfeld unter Anregung und Anleitung von Herrn Prof. Dr. Ochsenfeld und Herrn Dr. Asbjörn Burow verfasst.

Ich möchte Herrn Prof. Dr. Ochsenfeld für die Möglichkeit danken diese Arbeit in seinem Arbeitskreis zu verfassen, sowie für die interessante Themenstellung und die Unterstützung bei der schriftlichen Ausarbeitung.

Mein besonderer Dank gilt Herrn Dr. Asbjörn Burow, der mich meine ganze Arbeit hindurch unterstützt und maßgeblich beraten hat.

Des Weiteren möchte ich allen aus dem Arbeitskreis danken, die mir bei dieser Arbeit geholfen haben.

Abstract

This work presents a robust Random-Phase-Approximation (RPA) method to compute ground state energies not only for molecules but also for solids. A translation symmetry adapted Hartree kernel under periodic boundary conditions is derived using Bloch functions of local, atom-centered Gaussian-type basis functions and resolution of the identity (RI) factorization. Long-range Coulomb sums are evaluated in direct space using an adapted fast continuous multipole method (CFMM), which works for defined points in reciprocal space apart from Γ . The computational cost of this method scales as $\mathcal{O}(N^4 \log(N))$ with system size N and as $\mathcal{O}(N_k^2)$ with the number of sampled points k in reciprocal space N_k . Explicit treatment of 1D and 2D periodic materials avoids the need of full 3D calculations for chains or films. This method is implemented in the quantum chemistry package TURBOMOLE and adapts sparse density matrix storage and pre-screening of shell pairs to achieve further speedup.

As an addendum to these results a parallel implementation of the periodic electrostatic potential (ESP) is provided. This ESP implementation adopts the evaluation of the Coulomb lattice sums from density fitting (DF) accelerated CFMM present in the RIPER Code in TURBOMOLE. CPU parallelisation of the code yields a speedup of about 13 times for 16 cores compared to single core calculations.

This main part is accompanied by studies on the triphenyl triazin thiazole covalent organic framework (TTT-COF). COFs distinguish themselves from other polymers by their covalent connectivity, porosity, and crystallinity. The challenge of COF synthesis is to both yield a stable and a highly crystalline product with a minimum amount of structural defects. Therefore, a two step process is established for the synthesis of the TTT-COF. First, the triphenyl triazine imine COF (TTI-COF) is formed via a thermodynamically reversible order inducing step. Second, a post-synthetic topochemical conversion with elemental sulfur forms the aromatic sulfur rings of the TTT-COF. The TTT-COF exhibits enhanced chemical and electron stability compared to its precursor, allowing for an in-depth structural study via transmission electron microscopy (TEM). In particular, the TTT-COF displays one-dimensional defects, such as edge dislocations and grain dislocations introduced during the TTT-COF formation.

Contents

1	Introduction	1
2	Theory	5
2.1	Random Phase approximation	5
2.1.1	Adiabatic connection	5
2.1.2	Density fluctuation operators	7
2.1.3	Linear response theory	8
2.1.4	Fluctuation-dissipation theorem	15
2.1.5	ACFD correlation energy	17
2.1.6	Random phase approximation	18
2.2	Solids	20
2.2.1	Density functional theory and Kohn-Sham formalism	20
2.2.2	Crystal lattice	22
2.2.3	Basis functions under periodic boundary conditions	23
2.2.4	Density functional theory under periodic boundary conditions	25
2.2.5	Resolution of identity under periodic boundary conditions	28
2.2.6	Continuous Fast Multipole Method under Periodic boundary conditions	30
3	Publications and results	35
3.1	Random Phase Approximation for Periodic Systems Employing Direct Coulomb Lattice Summation	36
3.2	Topochemical conversion of an imine- into a thiazole-linked covalent organic framework enabling real structure analysis	56
3.3	Additional project: Implementation of the periodic electrostatic potential using local basis functions and the continuous fast multipole method	66
4	Conclusion and outlook	75
	Bibliography	77

Introduction

In quantum chemistry, there are different approaches to determine the ground state energy of molecular systems. One well-established method to do so is density functional theory (DFT), which employs the electron density for this purpose [1–5]. In doing so, it deliberately differs from Slater determinant based approaches such as Hartree-Fock, by substantially reducing the complexity of a Slater determinant to that of a density. The Hohenberg-Kohn theorem proves that the density functional of the (electronic) ground state energy of a given system exists, however the form of the exact functional is unknown. With the emergence of the Kohn-Sham (KS) approach, the electronic ground state energy could be approximated [1–5]. The remaining electron exchange correlation energy of the system [6], however, require further advanced approximations which gave rise to a wide variety of classes of density functionals, which vary strongly in accuracy [1, 3–5].

For a long time, it was unclear how the error in electron correlation energy estimation could be improved systematically besides functional approximations. The random phase approximation (RPA) offered a way to introduce such improvements in the estimation of the electron correlation energy [1, 7]. Historically, RPA has a long tradition. It was first introduced in the work of Bohm and Pines in the 1960s [8–10] and is one of the oldest non-perturbative methods. RPA re-emerged in the 2000s with the work of Furche [11], who reformulated RPA via the adiabatic-connection fluctuation dissipation theorem (ACFDT) by using the Bethe-Salpeter equation. The ACFDT allows to express the electron correlation energy in terms of the variables KS polarization propagator, Hartree kernel and dynamic frequency exchange kernel [1, 7, 11–14]. By neglecting the exchange correlation kernel, RPA emerged as a zero-order approximation to the exchange-correlation energy and is on the fifth rung of Jacob’s ladder for DFT [1, 7]. RPA is parameter-free, non-perturbative, and contains long range dispersion [15, 16]. Especially dispersion interactions prove difficult for many density functionals [17] and may require extensive parametrization due to semiempirical corrections [18, 19]. Remarkably, RPA is both applicable to DFT and Hartree-Fock [7, 12, 14] and can be extended even further [20].

Overall, RPA offers the opportunity to improve the accuracy of the already well-established DFT frameworks. Nevertheless, original calculations made by the formalism of Furche [11] are restricted to molecular systems. Transferring this approach from molecular to periodic systems is the next step. In order to do so, it comes naturally to apply already established DFT-formalisms, such as Bloch functions [21], to RPA. In contrast to a plane wave basis function approach, Bloch functions based on atom-centered local basis functions are used [22–28]. These Bloch functions allow for explicit treatment of any number of periodic directions in the system and direct spatial screening of local interactions [22–28].

The aim of the present work was to enable the calculation of RPA ground state correlation energy calculations for 1D (slabs), 2D (sheets), and 3D (crystals) periodic systems. To this end, a periodic RPA scheme was newly developed by utilizing the Hartree kernel and the polarization propagator. The first step was to introduce Bloch functions (already known from periodic DFT frameworks) to the periodic RPA formalism. The periodic Bloch functions were expanded to local Gaussian-type basis functions from molecular basis sets. This not only allowed for the explicit treatment of 1D and 2D systems in addition to 3D systems, but also reduces the number of basis functions compared to plane waves. In doing so, lattice sums over the complete crystal lattice were introduced, which, however, required additional treatment. In the case of RPA electron correlation energy this resulted in a particular evaluation of the two electron four center integrals in the Hartree kernel. Resolution of the identity (RI) for the Coulomb metric (known as well from DFT frameworks) allowed to reduce the computational cost of these integrals. Introducing standard Gaussian auxiliary basis functions, however, resulted in divergent terms at the Γ -point. To overcome these obstacles, charge projection (CP) [24] was used to eliminate the charged functions in the auxiliary basis set, which allowed for convergent calculations of the lattice sums over the integrals. The resulting lattice sums were evaluated using the continuous fast multipole method (CFMM) [24, 27, 29–35]. This method consists of two parts, an iterative scheme for the evaluation of the infinite periodic part of the lattice sum and a molecular part identical to molecular calculations. Taken together, the methods (Bloch functions, RI, CP, CFMM) allowed for a substantial speedup of the calculations and an overall scaling of $\mathcal{O}(N^4 \log(N))$. Implementation was programmed in TURBOMOLE using the existing periodic RI-DFT code RIPER as a basis. The paper **I** in chapter 3 details the implementation of this molecular and solid state implementation of RI-RPA in TURBOMOLE.

Additionally to this main part a conversion process of an imine- into a thiazole-linked covalent organic framework (COF) is characterized in this work. The examined imine- and thiazole-linked COFs consisted of 2D sheets stacked and kept in place by means of dispersion forces in the third dimension. The examined conversion enabled a novel insight into the crystalline nature of the material, including but not limited to crystal defects between and within the 2D sheets. The contribution to this work specifically consisted of 2D periodic DFT

calculations as a basis for the calculation of non-periodic, molecular nuclear magnetic resonance(NMR) shifts as shown in paper **II**, chapter 3.

Additional unpublished work is presented in part **III**, chapter 3.3. It introduces a scheme for calculating the periodic electrostatic potential (ESP) for the periodic DFT code RIPER in TURBOMOLE. The ESP can be considered as a fundamental part of quantum chemical calculations because it lays the foundation for solvation models [36, 37], may be used to align band structures for 3D systems[38, 39], may help in predicting the stability of organic cations[40], and may be used to derive atomic charges[41]. The ESP implementation described in chapter 3 employed CFMM to speed up the calculation.

2

Theory

2.1 Random Phase approximation

This chapter gives detailed insight of the derivation of the RPA following the adiabatic connection (AC) fluctuation-dissipation (FD) formalism of Furche and Eshuis [11, 20, 42–49] and is based upon the lecture notes of Burow [50] and standard textbooks [7, 12, 14]. This section forms the basis for paper **I** and stresses the fact, that the RPA formalism holds both for molecular orbitals and Bloch wave functions in the framework of density-functional theory (see section 2.2). The derivation starts with the AC formalism for the electron correlation energy leading to its exact expression in terms of excitation densities. The second part reformulates the AC correlation energy in terms of density fluctuations. The third section introduces the time-dependent linear response theory for the electron density followed by the derivation of the FD theorem in section 4 and the ACFD correlation energy in section 5. The last part concludes with the formula for the final RPA correlation energy.

2.1.1 Adiabatic connection

The idea behind the adiabatic connection is to avoid the calculation of the exact eigenstates of a system by instead solving a simpler, i.e. in the context of electron correlation, non-interacting system. Transition from the non-interacting to the fully interacting system is done by switching on the additional interaction contributions. This is done infinitely slow or adiabatically. In this section the adiabatic connection is used to derive an exact expression for the electron correlation energy [7, 14, 47, 50]. We start with the Hamiltonian of the form

$$\hat{H} = \hat{T} + \hat{V}_{\text{ext}} + \hat{V}_{\text{ee}} . \quad (2.1)$$

\hat{T} is the kinetic energy operator and \hat{V}_{ee} the electron-electron interaction operator. \hat{V}_{ext} is the operator for the external potential. We now introduce the coupling strength factor λ and rewrite equation 2.1 into the adiabatic Hamiltonian of the form [7, 47, 51–54]

$$\hat{H}^{(\lambda)} = \hat{T} + \hat{V}_{\text{ext}}^{(\lambda)} + \lambda \hat{V}_{ee}. \quad (2.2)$$

λ can assume any value between 0 and 1. At these boundaries the Hamiltonian respectively becomes the Hamiltonian for a system of non-interacting electrons $\lambda = 0$ or the fully interacting system $\lambda = 1$. $\hat{V}_{\text{ext}}^{(\lambda)}$ is chosen such that the adiabatic condition for the corresponding electron density $\rho^{(\lambda)}$

$$\rho^{(\lambda)}(x) = \rho^{(1)}(x) = \rho_0(x) \quad (2.3)$$

is satisfied for every $0 \leq \lambda \leq 1$. ρ_0 is consequently the electron density of the fully interacting system. $x = (\mathbf{r}, \sigma)$ denotes a combined space-spin coordinate with space \mathbf{r} and spin σ . The electronic ground state energy E_0 of the fully interacting system

$$E_0 = E_0^{(1)} = E_0^{(0)} + E_0^{(0 \rightarrow 1)} \text{ with } E_0^{(\lambda)} = \langle \Psi_0^{(\lambda)} | \hat{H}^{(\lambda)} | \Psi_0^{(\lambda)} \rangle \quad (2.4)$$

then consists of the ground state energy of a non-interacting system

$$E_0^{(0)} = \langle \Psi_0^{(0)} | \hat{H}^{(0)} | \Psi_0^{(0)} \rangle = \langle \Psi_0^{(0)} | \hat{T} + \hat{V}_{\text{ext}}^{(0)} | \Psi_0^{(0)} \rangle \quad (2.5)$$

and an additional correction term

$$E_0^{(0 \rightarrow 1)} = E_0^{(1)} - E_0^{(0)} = \int_0^1 \frac{\partial E_0^{(\lambda)}}{\partial \lambda} d\lambda. \quad (2.6)$$

Applying the Hellmann-Feynmann theorem [55] and the adiabatic condition 2.3 allows to reformulate equation 2.6

$$E_0^{(0 \rightarrow 1)} = \langle \Psi_0^{(0)} | \hat{V}_{\text{ext}}^{(1)} - \hat{V}_{\text{ext}}^{(0)} | \Psi_0^{(0)} \rangle + \int_0^1 \langle \Psi_0^{(\lambda)} | \hat{V}_{ee} | \Psi_0^{(\lambda)} \rangle d\lambda. \quad (2.7)$$

The complete ground state energy

$$E_0 = \langle \Psi_0^{(0)} | \hat{H} | \Psi_0^{(0)} \rangle + E_C \quad (2.8)$$

is now expressed in terms of an Hartree-Fock like term and an energy correlation term

$$E_C = \int_0^1 \langle \Psi_0^{(\lambda)} | \hat{V}_{ee} | \Psi_0^{(\lambda)} \rangle - \langle \Psi_0^{(0)} | \hat{V}_{ee} | \Psi_0^{(0)} \rangle d\lambda. \quad (2.9)$$

2.1.2 Density fluctuation operators

This section lays the foundation for the AC formalism and connects it with the time-dependent density response. We start with the electron-electron interaction operator in second quantization [12, 47]

$$\hat{V}_{ee} = \frac{1}{2} \sum_{\mathcal{P}\mathcal{Q}\mathcal{R}\mathcal{S}} \langle \mathcal{P}\mathcal{Q} | \mathcal{R}\mathcal{S} \rangle \hat{c}_{\mathcal{P}}^{\dagger} \hat{c}_{\mathcal{Q}}^{\dagger} \hat{c}_{\mathcal{S}} \hat{c}_{\mathcal{R}} . \quad (2.10)$$

\mathcal{P} , \mathcal{Q} , \mathcal{R} , \mathcal{S} are orbital indices. The orbitals are explicitly not restricted to molecular orbitals, they can either be single indices or compound indices as in the case of Bloch functions (see section 2.2.3). $\hat{c}_{\mathcal{P}}$ is the annihilation operator and removes an electron in orbital \mathcal{P} . Its adjoint $\hat{c}_{\mathcal{P}}^{\dagger}$ is the corresponding creation operator. As usual $\langle \mathcal{P}\mathcal{Q} | \mathcal{R}\mathcal{S} \rangle$ is the electron-electron repulsion integral in Dirac-notation. We now define the field operator

$$\hat{\psi}(x) = \sum_{\mathcal{P}} \varphi_{\mathcal{P}}^*(x) \hat{c}_{\mathcal{P}} , \quad (2.11)$$

where $\varphi_{\mathcal{P}}(x)$ is a single electron orbital. This definition allows to introduce the two-particle density operator

$$\hat{P}(x, x') = \frac{1}{2} \hat{\psi}^{\dagger}(x) \hat{\psi}^{\dagger}(x') \hat{\psi}(x') \hat{\psi}(x) \quad (2.12)$$

and reformulates the electron-electron interaction operator in terms of $\hat{P}(x, x')$

$$\hat{V}_{ee} = \int \frac{\hat{P}(x, x')}{|\mathbf{r} - \mathbf{r}'|} dx dx' . \quad (2.13)$$

Equation 2.12 can be reordered by the commutation and anti-commutation rules for creation and annihilation operators [12, 47]

$$\hat{P}(x, x') = \frac{1}{2} \left(-\delta(x - x') \hat{\psi}^{\dagger}(x) \hat{\psi}(x') + \hat{\psi}^{\dagger}(x) \hat{\psi}(x) \hat{\psi}^{\dagger}(x') \hat{\psi}(x') \right) \quad (2.14)$$

by exploiting the relation $\sum_{\mathcal{P}} \varphi_{\mathcal{P}}(x) \varphi_{\mathcal{P}}^*(x') = \delta(x - x')$. It is now obvious, that $\hat{P}(x, x')$ can be entirely rewritten in terms of the density operator

$$\hat{\rho}(x) = \hat{\psi}^{\dagger}(x) \hat{\psi}(x) . \quad (2.15)$$

Insertion of the density fluctuation operator

$$\Delta \hat{\rho}(x) = \hat{\rho}(x) - \rho(x) \quad (2.16)$$

and combining equations 2.9, 2.14, 2.15, and 2.16 yields

$$E_C = \frac{1}{2} \int_0^1 d\lambda \int \frac{\langle \Psi_0^{(\lambda)} | \Delta \hat{\rho}(x) \Delta \hat{\rho}(x') | \Psi_0^{(\lambda)} \rangle - \langle \Psi_0^{(0)} | \Delta \hat{\rho}(x) \Delta \hat{\rho}(x') | \Psi_0^{(0)} \rangle}{|\mathbf{r} - \mathbf{r}'|} dx dx' \quad (2.17)$$

This expression of the correlation energy can be further simplified by inserting the completeness of states

$$\sum_n |\Psi_n^{(\lambda)}\rangle \langle \Psi_n^{(\lambda)}| = \mathbf{1} \quad (2.18)$$

for all states n for any arbitrary λ . The integrals in equation 2.17 can thus be divided into

$$\langle \Psi_0^{(\lambda)} | \Delta \hat{\rho}(x) \Delta \hat{\rho}(x') | \Psi_0^{(\lambda)} \rangle = \sum_{n \neq 0} \rho_{0n}^{(\lambda)}(x) \rho_{n0}^{(\lambda)}(x') \quad (2.19)$$

containing the transition densities

$$\rho_{nm}^{(\lambda)}(x) = \langle \Psi_n^{(\lambda)} | \Delta \hat{\rho}(x) | \Psi_m^{(\lambda)} \rangle = \langle \Psi_n^{(\lambda)} | \hat{\rho}(x) | \Psi_m^{(\lambda)} \rangle = (\rho_{mn}^{(\lambda)}(x))^* . \quad (2.20)$$

The sum over all states in equation 2.19 deliberately excludes the ground state as the expectation value of the density fluctuation operator is zero. Equation 2.17 can now be expressed exclusively in terms of transition densities.

$$E_C = \frac{1}{2} \sum_{n \neq 0} \int_0^1 d\lambda \int \frac{\rho_{0n}^{(\lambda)}(x) \rho_{n0}^{(\lambda)}(x') - \rho_{0n}^{(0)}(x) \rho_{n0}^{(0)}(x')}{|\mathbf{r} - \mathbf{r}'|} dx dx' \quad (2.21)$$

For real transition densities $\rho_{n0}^{(\lambda)} = \rho_{0n}^{(\lambda)}$, i.e. in the molecular case, the AC correlation energy in equation 2.21 simplifies to [47]

$$E_C = \int_0^1 \sum_{n \neq 0} E_H[\rho_{0n}^{(\lambda)}] - E_H[\rho_{0n}^{(0)}] d\lambda \quad \text{with} \quad E_H[\rho] = \frac{1}{2} \int \frac{\rho(x) \rho(x')}{|\mathbf{r} - \mathbf{r}'|} dx dx' . \quad (2.22)$$

2.1.3 Linear response theory

Equation 2.21 will form the basis for connecting the linear response theory with the AC correlation theory. This section therefore focuses on the basics of the time-dependent linear response theory and introduces the spectral or Lehmann representation [7, 12] of the density-density response function.

Time-dependent Schrödinger equation

As a prerequisite we introduce two important pictures used in quantum chemistry, the Schrödinger picture and the interaction picture [12]. Starting point is the time-dependent

Schrödinger equation written as

$$i\hbar \frac{\partial}{\partial t} |\Psi(t)\rangle = \hat{H} |\Psi(t)\rangle, \quad (2.23)$$

where $\Psi(t)$ is the time-dependent wave function. In this so called Schrödinger picture \hat{H} is explicitly time-independent save for a possible time-dependent external field and the wave function

$$|\Psi(t)\rangle = e^{-i\hat{H}(t-t_0)/\hbar} |\Psi(t_0)\rangle \quad (2.24)$$

is defined by its initial state at time t_0 . If not stated otherwise we set $t_0 = 0$ in the following. In many cases the Hamiltonian can be decomposed into two time-independent parts \hat{H}_0 and \hat{H}'

$$\hat{H} = \hat{H}_0 + \hat{H}'. \quad (2.25)$$

Assuming that the time-independent solution to \hat{H}_0 is already established, the interaction picture allows to conveniently take the effect of \hat{H}' into account by

$$i\hbar \frac{d}{dt} |\Psi_I(t)\rangle = \hat{H}'(t) |\Psi_I(t)\rangle. \quad (2.26)$$

$\Psi_I(t)$, the wave function in the interaction picture, is derived from the Schrödinger picture by

$$\Psi_I(t) = e^{i\hat{H}_0 t/\hbar} |\Psi(t)\rangle. \quad (2.27)$$

An operator in the interaction picture $\hat{O}_I(t)$ consequently takes a more complicated form as in the Schrödinger picture \hat{O}_S

$$\hat{O}_I(t) = e^{i\hat{H}_0 t/\hbar} \hat{O}_S e^{-i\hat{H}_0 t/\hbar}. \quad (2.28)$$

Linear response

In the next step we introduce the basics of the linear response theory [7, 14, 56, 57]. The framework of the adiabatic connection from section 2.1.1 is adapted in this context and we insert the adiabatic Hamiltonian from 2.2 into the Schrödinger picture 2.23. Consider an observable A for the ground state wave function $\Psi_0^{(\lambda)}$. We now perturb the time-independent ground-state Hamiltonian $\hat{H}_0^{(\lambda)}$ by a time-dependent perturbation $\hat{H}_1^{(\lambda)}(t)$ at t_0 [7, 14]

$$\hat{H}^{(\lambda)} = \hat{H}_0^{(\lambda)} + \hat{H}_1^{(\lambda)}(t) \text{ with } \hat{H}_1^{(\lambda)}(t) = 0 \text{ for } t < t_0. \quad (2.29)$$

$\hat{H}_1^{(\lambda)}(t) = \hat{H}_1(t)$ is identical for every λ and should not be confused with \hat{H}' in equation 2.25: $\hat{H}_1(t)$ is a time-dependent perturbation applied to the time-independent Hamilton operator, whereas \hat{H}' is part of the ground state Hamilton operator. We assume, that \hat{H}_1 is sufficiently small so that \hat{H}_1 can be described by a small scalar Field F , which couples to an observable

B ,

$$\hat{H}_1^{(\lambda)}(t) = \hat{H}_1(t) = F(t)\hat{B} \text{ for } t \geq t_0. \quad (2.30)$$

We now define a time-evolution operator U [7]

$$\Psi^{(\lambda)}(t) = \hat{U}(t, t_0)\Psi^{(\lambda)}(t_0), \quad (2.31)$$

which acts on the initial state of the wave function $\Psi(t_0)$ in 2.23) and propagates it to time t . In the framework of linear response theory it is formally simpler to decompose \hat{U} into

$$\hat{U}(t, t_0) = e^{-i\hat{H}_0^{(\lambda)}(t-t_0)/\hbar}\hat{U}_1(t, t_0). \quad (2.32)$$

Combination of equation 2.31 with 2.32 and subsequent insertion into the time-dependent Schrödinger equation in the Schrödinger picture 2.23 yields

$$i\hbar\frac{d}{dt}\hat{U}_1(t, t_0) = e^{i\hat{H}_0^{(\lambda)}(t-t_0)/\hbar}F(t)\hat{B}e^{-i\hat{H}_0^{(\lambda)}(t-t_0)/\hbar}\hat{U}_1(t, t_0). \quad (2.33)$$

Equation 2.33 can be solved by iteration using the fact that the time evolution operator of the initial state or zeroth-order contribution must be the identity operator $\hat{U}(t_0, t_0) = \hat{1}$. The first order approximation of \hat{U}_1 becomes

$$\hat{U}_1(t, t_0) \approx 1 - \frac{i}{\hbar} \int_{t_0}^t F(t')\hat{B}(t-t')dt', \quad (2.34)$$

where $\hat{B}(t)$ is given in the interaction picture

$$\hat{B}(t) = e^{i\hat{H}_0 t/\hbar}\hat{B}e^{-i\hat{H}_0 t/\hbar}. \quad (2.35)$$

The complete time-evolution operator to first-order can now be constructed by equation 2.34 and 2.32

$$U(t, t_0) \approx e^{i\hat{H}_0^{(\lambda)}(t-t_0)/\hbar} \left\{ 1 - \frac{i}{\hbar} \int_{t_0}^t F(t')\hat{B}(t-t')dt' \right\}. \quad (2.36)$$

We now examine the effect of the perturbation on an observable A . Let

$$\langle A \rangle_0^{(\lambda)} = \langle \Psi_0^{(\lambda)} | \hat{A} | \Psi_0^{(\lambda)} \rangle \quad (2.37)$$

be the ground state expectation value of the observable for the unperturbed system and

$$\langle A \rangle^{(\lambda)} = \langle \Psi^{(\lambda)} | \hat{A}(t) | \Psi^{(\lambda)} \rangle \quad (2.38)$$

be the expectation value of the time-dependent system. As long as the perturbation \hat{H}_1 is sufficiently small the expectation value can be expanded via a series expansion dependent on

the field F

$$\langle A \rangle^{(\lambda)}(t) = \langle A \rangle_0^{(\lambda)} + \langle A \rangle_1^{(\lambda)}(t) + \langle A \rangle_2^{(\lambda)}(t) + \dots \quad (2.39)$$

The first order or linear response $\langle A \rangle_l^{(\lambda)} = \langle A \rangle_0^{(\lambda)} + \langle A \rangle_1^{(\lambda)}(t)$ can then be derived by insertion of the first order time-evolution operator 2.36 into 2.38

$$\langle A \rangle_l^{(\lambda)} = -\frac{i}{\hbar} \int_{t_0}^t dt' F(t') \langle \Psi_0^{(\lambda)} | [\hat{A}(t), \hat{B}(t')] | \Psi_0^{(\lambda)} \rangle. \quad (2.40)$$

Both operators $\hat{A}(t)$ and $\hat{B}(t)$ are given in the interaction picture. The linear response is commonly expressed in terms of the retarded response function [7, 12]

$$\chi_{AB}^{(\lambda)}(t, t') = -\frac{i}{\hbar} \theta(t - t') \langle \Psi_0^{(\lambda)} | [\hat{A}(t), \hat{B}(t')] | \Psi_0^{(\lambda)} \rangle \quad (2.41)$$

by insertion into equation 2.40

$$\langle A \rangle_l^{(\lambda)}(t) = \int_{-\infty}^{\infty} F(t') \chi_{AB}^{(\lambda)}(t, t') dt'. \quad (2.42)$$

The Heaviside step function $\theta(t - t')$ ensures that no system response occurs before the initial perturbation at time t' , hence the prefix 'retarded'. Note that the integral boundaries are modified: $\theta(t - t')$ allows to modify the upper integral bound, whereas the lower boundary can be set to $-\infty$ as long as $F(t')$ vanishes for $t < t_0$.

Response function and Lehmann representation

We will now transform the retarded response function into a more suitable form. We start by taking the relation [7]

$$\langle \Psi_0^{(\lambda)} | [\hat{A}(t), \hat{B}(t')] | \Psi_0^{(\lambda)} \rangle = \langle \Psi_0^{(\lambda)} | [\hat{A}(t - t'), \hat{B}] | \Psi_0^{(\lambda)} \rangle \quad (2.43)$$

into account. The response function in equation 2.41 is therefore only dependent on the relative time difference $t - t'$

$$\chi(t - t')^{(\lambda)} = -\frac{i}{\hbar} \theta(t - t') \langle \Psi_0^{(\lambda)} | [\hat{A}(t - t'), \hat{B}] | \Psi_0^{(\lambda)} \rangle. \quad (2.44)$$

It is thus advantageous to Fourier transform the response function from the time to the frequency domain ω [7, 12]

$$\chi_{AB}^{(\lambda)}(\omega) = \int_{-\infty}^{\infty} d(t - t') e^{i\omega(t-t')} \chi_{AB}^{(\lambda)}(t - t'). \quad (2.45)$$

This representation of the response function allows to conveniently express the linear response 2.42 in terms of the frequency

$$\langle A \rangle_l^{(\lambda)}(\omega) = F(\omega) \chi_{AB}^{(\lambda)}(\omega), \quad (2.46)$$

where $F(\omega)$ is the Fourier transform of the scalar field $F(t)$. To find an expression for $\chi_{AB}^{(\lambda)}(\omega)$ we start with the formulation in the time-domain in equation 2.41 and combine this with the completeness of states in 2.18

$$\chi(t-t')^{(\lambda)} = -\frac{i}{\hbar} \theta(t-t') \sum_{n \neq 0} \left[e^{-\frac{i}{\hbar}(E_n^{(\lambda)} - E_0^{(\lambda)})(t-t')} A_{0n}^{(\lambda)} B_{n0}^{(\lambda)} - e^{-\frac{i}{\hbar}(E_0^{(\lambda)} - E_n^{(\lambda)})(t-t')} B_{0n}^{(\lambda)} A_{n0}^{(\lambda)} \right] \quad (2.47)$$

with the following short hand notation

$$\begin{aligned} A_{nm}^{(\lambda)} &= \langle \Psi_n^{(\lambda)} | \hat{A} | \Psi_m^{(\lambda)} \rangle \\ B_{nm}^{(\lambda)} &= \langle \Psi_n^{(\lambda)} | \hat{B} | \Psi_m^{(\lambda)} \rangle. \end{aligned} \quad (2.48)$$

To simplify equation 2.47 we use

$$\int_{-\infty}^{\infty} e^{-i(\omega-\omega')(t-t')} d(t-t') = 2\pi \delta(\omega - \omega'), \quad (2.49)$$

where δ is the Dirac-distribution. Combination of equation 2.49 with the integral representation of the Heaviside step function [12]

$$\theta(t-t') = -\lim_{\eta \rightarrow 0^+} \int_{-\infty}^{\infty} \frac{1}{2\pi i} \frac{1}{\omega + i\eta} e^{-i\omega(t-t')} d\omega \quad (2.50)$$

results in the relation

$$\int_{-\infty}^{\infty} \theta(t-t') e^{i\omega(t-t')} d(t-t') = \lim_{\eta \rightarrow 0^+} \frac{-i}{\omega + i\eta}. \quad (2.51)$$

η is an infinitesimally small real frequency greater than zero and guarantees that the expression is analytic. Finally combining equation 2.51 and 2.47 with 2.45 yields the spectral or Lehmann-representation of the retarded response function [7, 12, 14, 47]

$$\chi^{(\lambda)}(\omega) = \frac{1}{\hbar} \lim_{\eta \rightarrow 0^+} \sum_{n \neq 0} \frac{A_{0n}^{(\lambda)} B_{n0}^{(\lambda)}}{\omega - \Omega_{n0}^{\lambda} + i\eta} - \frac{B_{0n}^{(\lambda)} A_{n0}^{(\lambda)}}{\omega + \Omega_{n0}^{\lambda} + i\eta}. \quad (2.52)$$

$\Omega_{n0}^{\lambda} = (E_n^{(\lambda)} - E_0^{(\lambda)})/\hbar$ is the excitation energy of the system divided by \hbar . In the following atomic units will be used, e.g., $\hbar \hat{=} 1$ is normalized to one and $\Omega_{n0}^{\lambda} = (E_n^{(\lambda)} - E_0^{(\lambda)})$. The poles

of $\chi^{(\lambda)}(x, x', \omega)$ are located in the lower complex plane at $\omega = \Omega_{n0}^\lambda - i\eta$ and $\omega = -\Omega_{n0}^\lambda - i\eta$ at the resonance frequencies, therefore the name 'spectral representation'.

The density-density response function

Following the formalism of linear response theory we now want to describe the first order perturbation of the density to the fully interacting system due to an external perturbing potential. We therefore set $\hat{A}(x, t) = \Delta\hat{\rho}(x, t)$ in equation 2.38 and $\hat{B}(x, t) = \Delta\hat{\rho}(x, t)$ in equation 2.30 and perturb by the scalar field $F(x, t) = v_1(x, t)$. The potential of the perturbed adiabatic Hamiltonian in equation 2.2 then becomes [7, 56]

$$v_0^{(\lambda)}(x, t) = v_0^{(\lambda)}(x) + v_1(x, t). \quad (2.53)$$

We keep the convention, that $v_1(x, t) = 0$ for $t < t_0$. The first order response of the density for the (partially) interacting system λ can now be written as

$$\rho_1^{(\lambda)}(x, t) = \int_0^\infty dt' \int dx' \chi^{(\lambda)}(x, t, x', t') v_1(x', t'). \quad (2.54)$$

The form of the density-density response function in atomic units according to 2.41 is

$$\chi^{(\lambda)}(x, t, x', t') = \chi_{\Delta\hat{\rho}\Delta\hat{\rho}}^{(\lambda)}(x, t, x', t') = -i\theta(t - t') \langle \Psi_0^{(\lambda)} | [\Delta\hat{\rho}(x, t), \Delta\hat{\rho}(x', t')] | \Psi_0^{(\lambda)} \rangle \quad (2.55)$$

The expression above can be reformulated in the more conventional Lehmann-representation by taking equation 2.20 and 2.52 into account

$$\chi^{(\lambda)}(x, x', \omega) = \lim_{\eta \rightarrow 0^+} \sum_{n \neq 0} \frac{\rho_{0n}^{(\lambda)}(x) \rho_{n0}^{(\lambda)}(x')}{\omega - \Omega_{n0}^\lambda + i\eta} - \frac{\rho_{0n}^{(\lambda)}(x') \rho_{n0}^{(\lambda)}(x)}{\omega + \Omega_{n0}^\lambda + i\eta}. \quad (2.56)$$

The form of the response function is normally non-analytical. An exception to this is the Kohn-Sham response function of the non-interacting system. Its derivation is straightforward by insertion of the Kohn-Sham determinant and evaluation of the transition densities in 2.56 [7, 47, 56]

$$\chi^{(0)}(x, x', \omega) = \lim_{\eta \rightarrow 0^+} \sum_{\mathcal{P}\mathcal{Q}} \sum_{\sigma} (f_{\mathcal{P}\sigma} - f_{\mathcal{Q}\sigma}) \delta_{\sigma\sigma'} \frac{\varphi_{\mathcal{P}}^*(x) \varphi_{\mathcal{Q}}(x) \varphi_{\mathcal{Q}}^*(x') \varphi_{\mathcal{P}}(x')}{\omega - (\varepsilon_{\mathcal{Q}} - \varepsilon_{\mathcal{P}}) - i\eta}. \quad (2.57)$$

No further restrictions are applied to the orbital indices \mathcal{P} and \mathcal{Q} of the Kohn-Sham orbitals φ and their orbital energies ε ; they may be either molecular orbitals or compound indices. $\delta_{\sigma\sigma'}$ ensures, that only compound coordinates x and x' with identical spin components contribute to $\chi^{(0)}$. $f_{\mathcal{P}\sigma}$ and $f_{\mathcal{P}\sigma}$ are occupation numbers of the Kohn-Sham ground state. An explicit spin dependency is included, so that the expression is both valid for open and closed shell cases. Nat-

urally the question arises if we can express the interacting response function entirely in terms of the non-interacting response function. We therefore examine the response function in more detail: According to the Runge-Gross [4, 7] and van Leeuwen theorem [7] there is a one-to-one correspondence between the fully-interacting time-dependent density $\rho_0(x, t) = \rho^{(1)}(x, t)$ and the time-dependent potential $v^{(1)}[\rho](x, t)$. Furthermore this density can be expressed in terms of a time-dependent non-interacting Kohn-Sham potential $v_s[\rho](x, t) = v^{(0)}[\rho](x, t)$ marking $\rho^{(1)}$ as a functional of both $v(x, t)$ and the time-dependent Kohn-Sham potential $v_s(x, t)$ [7]

$$\rho^{(1)} \equiv \rho^{(1)}[v^{(1)}(x, t)] \equiv \rho^{(1)}[v_s(x, t)]. \quad (2.58)$$

For any partially interacting system, this should hold as well. The linear response of any partially interacting system perturbed by v_1 can then be described as

$$\rho_l^{(\gamma)}(x, t) = \int_0^\infty dt' \int dx' \chi^{(0)}(x, t, x', t') v_1^{(\gamma)}(x', t'). \quad (2.59)$$

The linear effective potential

$$v_1^{(\lambda)}(x, t) = v_1(x, t) + \int dx \frac{\lambda \rho_1(x', t)}{|\mathbf{r} - \mathbf{r}'|} + v_{xc1}^{(\lambda)}(x, t) \quad (2.60)$$

contains the scaled electron-electron interaction potential. Its exchange-correlation part can be derived via

$$v_{xc1}^{(\lambda)}(x, t) = \int dt' \int dx' f_{xc}^{(\lambda)}(x, t, x', t') \rho_l^{(\lambda)}(x', t') \quad (2.61)$$

as long as the perturbation is sufficiently small. The exact form of the time-dependent exchange-correlation kernel [58–60]

$$f_{xc}^{(\lambda)}(x, t, x', t') = \left. \frac{\delta v_{xc}^{(\lambda)}(x, t)}{\delta \rho(x', t')} \right|_{\rho=\rho_0} \quad (2.62)$$

is not known *a priori*. By setting equation 2.54 equal to equation 2.59 we obtain

$$\int_0^\infty dt' \int dx' \chi^{(\lambda)}(x, t, x', t') v_1^{(\lambda)}(x', t') = \int_0^\infty dt' \int dx' \chi^{(0)}(x, t, x', t') v_1^{(\lambda)}(x', t'). \quad (2.63)$$

Insertion of equation 2.60 and 2.61 [7, 14] into 2.63 results in

$$\begin{aligned} \int dt_2 \int dx_2 \chi^{(\lambda)}(x_1, t_1, x_2, t_2) v_1(x_2, t_2) &= \int dt_2 \int dx_2 \chi^{(0)}(x_1, t_1, x_2, t_2) \\ &\left[v_1(x_2, t_2) + \int t_3 \int dx_3 \left\{ \frac{\lambda \delta(t_2 - t_3)}{|\mathbf{r}_2 - \mathbf{r}_3|} + f_{xc}^{(\lambda)}(x_2, t_2, x_3, t_3) \right\} \right. \\ &\left. \int dt_4 \int dx_4 \chi^{(\lambda)}(x_3, t_3, x_4, t_4) v_1(x_4, t_4) \right]. \quad (2.64) \end{aligned}$$

The response functions in the expression above are ground state properties of the corresponding systems and therefore independent of $v_1(x_2, t_2)$. This allows to further simplify the expression to

$$\begin{aligned} \chi^{(\lambda)}(x_1, t_1, x_2, t_2) = & \chi^{(0)}(x_1, t_1, x_2, t_2) + \int dx_3 \int dt_3 \int dx_4 \int dt_4 \chi^0(x_1, t_1, x_3, t_3) \\ & \left(\frac{\lambda \delta(t_3 - t_4)}{|\mathbf{r}_3 - \mathbf{r}_4|} + f_{xc}^{(\lambda)}(x_3, t_3, x_4, t_4) \right) \chi^{(\lambda)}(x_4, t_4, x_2, t_2). \end{aligned} \quad (2.65)$$

Equation 2.65 gives the final Dyson-like relation between the interacting and non-interacting response function. A more compact notation can be derived by applying the Fourier transformation to equation 2.65. We introduce the following short hand notation

$$(\mathbf{ab})_{xx'} = \int dx'' \mathbf{a}(x, x'', \omega) \mathbf{b}(x'', x', \omega). \quad (2.66)$$

and can then write the Dyson equation as [14, 43, 58, 59]

$$\chi^{(\lambda)} = \chi^{(0)} + \chi^{(0)} \mathbf{f}_{hxc}^{(\lambda)} \chi^{(\lambda)}. \quad (2.67)$$

For convenience we use the combined Hartree-exchange kernel

$$\mathbf{f}_{hxc}^{(\lambda)} = \lambda \mathbf{v} + \mathbf{f}_{xc} \quad (2.68)$$

and write the Hartree kernel as $(\mathbf{v})_{xx'} = v(x, x') = v(\mathbf{r}, \mathbf{r}') = \frac{1}{|\mathbf{r} - \mathbf{r}'|}$.

2.1.4 Fluctuation-dissipation theorem

We now link the density fluctuations occurring in the AC formalism to the response function. We therefore derive an expression of the fluctuation-dissipation theorem for the density response formalism. The fluctuation-dissipation theorem was first introduced by Callen and Welton [61], who applied it to electrical systems and extended it to, e.g., Brownian motions and pressure fluctuations in gases. We first decompose equation 2.56 into two contributions [50]

$$\chi^{(\lambda)}(x, x', \omega) = \lim_{\eta \rightarrow 0^+} \sum_{n \neq 0} \{ f_{\lambda, n}^+(x, x', \omega) - f_{\lambda, n}^-(x, x', \omega) \} \quad (2.69)$$

with

$$f_{\lambda, n}^+(x, x', \omega) = \frac{\rho_{0n}^{(\lambda)}(x) \rho_{n0}^{(\lambda)}(x')}{\omega - \Omega_{n0}^\lambda + i\eta} \quad \text{and} \quad f_{\lambda, n}^-(x, x', \omega) = \frac{\rho_{0n}^{(\lambda)}(x') \rho_{n0}^{(\lambda)}(x)}{\omega + \Omega_{n0}^\lambda + i\eta}. \quad (2.70)$$

Following the Cauchy integral theorem [62] we define a closed counterclockwise contour Γ in the complex frequency plane consisting of the contour on the imaginary axis c_i and the

half-circle on the 'left' side of the imaginary axis (see picture 2.1)

$$\begin{aligned} \oint_{\Gamma} \chi^{(\lambda)}(x, x', \omega) d\omega &= \int_{c_i} \chi^{(\lambda)}(x, x', \omega) d\omega + \int_{c_{\text{arc}}} \chi^{(\lambda)}(x, x', \omega) d\omega = \\ &= i \int_{-\infty}^{\infty} \chi^{(\lambda)}(x, x', iu) du + \int_{c_{\text{arc}}} \chi^{(\lambda)}(x, x', \omega) d\omega \end{aligned} \quad (2.71)$$

The second line of equation 2.71 follows by substituting $d\omega = diu = idu$, where u is the imaginary part of ω . The residues of $\chi^{(\lambda)}(x, x', \omega)$ are properly defined by the single poles according to the residue theorem, i.e.

$$\begin{aligned} \text{Res} (\chi^{(\lambda)}(x, x', \omega)) \Big|_{\omega=\Omega_{n0}^{\lambda}-i\eta} &= \text{Res} (f_{\lambda,n}^{+}(x, x', \omega)) \Big|_{\omega=\Omega_{n0}^{\lambda}-i\eta} \\ &= \rho_{0n}^{(\lambda)}(x) \rho_{n0}^{(\lambda)}(x') \end{aligned} \quad (2.72)$$

$$\begin{aligned} \text{Res} (\chi^{(\lambda)}(x, x', \omega)) \Big|_{\omega=-\Omega_{n0}^{\lambda}-i\eta} &= - \text{Res} (f_{\lambda,n}^{-}(x, x', \omega)) \Big|_{\omega=-\Omega_{n0}^{\lambda}-i\eta} \\ &= - \rho_{0n}^{(\lambda)}(x') \rho_{n0}^{(\lambda)}(x) . \end{aligned} \quad (2.73)$$

Following the Cauchy theorem the path integral over Γ is characterized by all enclosed poles and their residues, respectively,

$$\oint_{\Gamma} \chi^{(\lambda)}(x, x', \omega) d\omega = -2\pi i \sum_{n \neq 0} \rho_{0n}^{(\lambda)}(x') \rho_{n0}^{(\lambda)}(x) . \quad (2.74)$$

The integral

$$\int_{c_{\text{arc}}} \chi^{(\lambda)}(x, x', \omega) d\omega = \lim_{\eta \rightarrow 0^+} \sum_{n \neq 0} \left\{ \int_{c_{\text{arc}}} f_{\lambda,n}^{+}(x, x', \omega) d\omega - \int_{c_{\text{arc}}} f_{\lambda,n}^{-}(x, x', \omega) d\omega \right\} \quad (2.75)$$

can be solved by approximating [50]

$$\int_{c_{\text{arc}}} \frac{1}{\omega \pm \Omega_{n0}^{\lambda} - i\eta} d\omega \sim \int_{c_{\text{arc}}} \frac{1}{\omega} d\omega = \int_{\frac{1}{2}\pi}^{\frac{3}{2}\pi} i\phi d\phi = i\pi \quad (2.76)$$

This relation holds as long as $|\Omega_{n0}^{\lambda}|$ is finite and small compared to $|\omega|$ and η tends to zero. The path integral over c_{arc} can then be expressed as

$$\int_{c_{\text{arc}}} \chi^{(\lambda)}(x, x', \omega) d\omega = \sum_{n \neq 0} \left\{ i\pi \rho_{0n}^{(\lambda)}(x) \rho_{n0}^{(\lambda)}(x') - i\pi \rho_{0n}^{(\lambda)}(x') \rho_{n0}^{(\lambda)}(x) \right\} \quad (2.77)$$

Inserting equation 2.77 and 2.74 into 2.71 finally results in [50]

$$\begin{aligned}
& \int_{-\infty}^{\infty} \chi^{(\lambda)}(x, x', iu) du = \\
& = \sum_{n \neq 0} \left\{ -2\pi \rho_{0n}^{(\lambda)}(x') \rho_{n0}^{(\lambda)}(x) - \left\{ \pi \rho_{0n}^{(\lambda)}(x) \rho_{n0}^{(\lambda)}(x') - \pi \rho_{0n}^{(\lambda)}(x') \rho_{n0}^{(\lambda)}(x) \right\} \right\} = \\
& = -\pi \sum_{n \neq 0} \left\{ \rho_{0n}^{(\lambda)}(x) \rho_{n0}^{(\lambda)}(x') + \rho_{0n}^{(\lambda)}(x') \rho_{n0}^{(\lambda)}(x) \right\} = \\
& = -2\pi \sum_{n \neq 0} \text{Re} \left\{ \rho_{0n}^{(\lambda)}(x) \rho_{n0}^{(\lambda)}(x') \right\}. \tag{2.78}
\end{aligned}$$

Equation 2.78 links the response of the system to a time-dependent perturbation to the real part of transition density products and is therefore the fluctuation-dissipation theorem applied to density fluctuations. Note that for real transition densities $\rho_{n0}^{(\lambda)} = \rho_{0n}^{(\lambda)}$ equation 2.78 simplifies to the molecular expression [7, 14, 47].

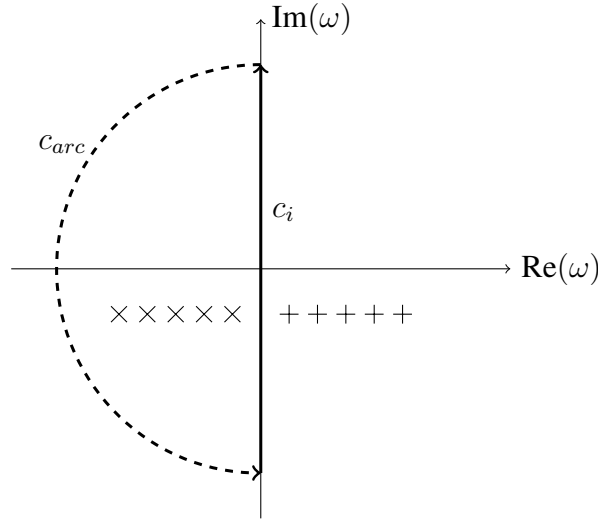


Figure 2.1: Integration path for the retarded response function $\chi^{(\lambda)}(x, x', \omega)$ in the frequency plane. The '+' mark simple poles of χ^λ stemming from the f^+ -term, the 'x' from the f^- -term. The contour $\Gamma = c_i + c_{\text{arc}}$ consists of two separate contours c_i and c_{arc} enclosing all poles in the left half of the complex plane. c_i is the integration path along the imaginary axis from $-\infty$ to ∞ and c_{arc} is the counter-clockwise half circle in the left half of the complex plane.

2.1.5 ACFD correlation energy

We now recall the adiabatic connection correlation energy from equation 2.21

$$E_C = \frac{1}{2} \sum_{n \neq 0} \int_0^1 d\lambda \int dx dx' \rho_{0n}^{(\lambda)}(x) \rho_{n0}^{(\lambda)}(x') v(\mathbf{r}, \mathbf{r}') - \rho_{0n}^{(0)}(x) \rho_{n0}^{(0)}(x') v(\mathbf{r}, \mathbf{r}'). \tag{2.79}$$

With equation 2.78 at hand, the final adiabatic-connection fluctuation dissipation (ACFD) correlation energy becomes

$$\begin{aligned}
E_C &= \text{Re}(E_C) = \frac{1}{2}E_C + \frac{1}{2}E_C^* = \\
&= \frac{1}{4} \sum_{n \neq 0} \int_0^1 d\lambda \int \left\{ 2\text{Re} \left(\rho_{0n}^{(\lambda)}(x) \rho_{n0}^{(\lambda)}(x') \right) v(\mathbf{r}, \mathbf{r}') - 2\text{Re} \left(\rho_{0n}^{(0)}(x) \rho_{n0}^{(0)}(x') \right) v(\mathbf{r}, \mathbf{r}') \right\} dx dx' = \\
&= -\frac{1}{2} \int_0^1 d\lambda \int dx dx' \int_{-\infty}^{\infty} \frac{du}{2\pi} \chi^{(\lambda)}(x, x', iu) v(\mathbf{r}, \mathbf{r}') - \chi^{(0)}(x, x', iu) v(\mathbf{r}, \mathbf{r}') . \tag{2.80}
\end{aligned}$$

However, this transformation comes with the cost of an additional integration over the frequency u , which has to be performed numerically [47, 63]. As the order of spatial and frequency as well as spin integration can be interchanged we can write this expression in a more compact form using the convention of 2.66

$$E_C = -\frac{1}{2} \int_0^1 d\lambda \int_{-\infty}^{\infty} \frac{du}{2\pi} \text{tr} \left\{ \mathbf{v} \left[\chi^{(\lambda)}(iu) - \chi^{(0)}(iu) \right] \right\} , \tag{2.81}$$

where $\text{tr} \{ \mathbf{A} \}$ denotes the trace over matrix \mathbf{A} .

2.1.6 Random phase approximation

So far no approximations have been made for the first order ACFD correlation energy. Equation 2.81 is still an exact expression. However, no analytical expression for the interacting density-density response function are known except for the simplest physical systems. We therefore have to approximate the interacting response function. The so called direct Random-Phase approximation sets the exchange-correlation kernel in equation 2.68 to zero [20]

$$f_{hxc}^{RPA} = \lambda \mathbf{v} . \tag{2.82}$$

The approximation is termed 'random-phase approximation' for historical reasons [8–10, 64] and might as well be named time-dependent Hartree approximation [14]. The Dyson equation 2.67 can now be solved analytically for the random-phase response function

$$\chi_{\text{RPA}}^{(\lambda)} = \left[(\chi^{(0)})^{-1} + \lambda \mathbf{v} \right]^{-1} \tag{2.83}$$

We now insert 2.83 into 2.81. The resulting first term can be reformulated by expanding the inverse of the matrices into a series expansion and regrouping it via the logarithm

$$\int_0^1 d\lambda \text{tr} \left[\mathbf{v} \chi_{\text{RPA}}^{(\lambda)}(iu) \right] = \int_0^1 d\lambda \text{tr} \left[\chi_{\text{RPA}}^{(\lambda)}(iu) \mathbf{v} \right] = -\text{tr} \left[\ln \left(1 + \chi^{(0)}(iu) \mathbf{v} \right) \right] . \tag{2.84}$$

The final RPA correlation energy thus reads [20, 43–49]

$$E_C^{\text{RPA}} = \frac{1}{2} \int_{-\infty}^{\infty} \frac{du}{2\pi} \text{tr} \left[\ln (1 + \chi^{(0)}(iu)\mathbf{v}) + \chi^{(0)}(iu)\mathbf{v} \right] , \quad (2.85)$$

It should be noted, that different approaches to the RPA exist. It is for example possible to derive an identical expression for E_C^{RPA} via the polarization propagator formalism [12, 13]. By using a diagrammatic approach the correlation energy can be expressed via the causal polarization propagator $\Pi^{(\lambda)}$ of coupled system λ

$$E_C = -\frac{1}{2} \int_0^1 d\lambda \int_{-\infty}^{\infty} \frac{du}{2\pi} \text{tr} \left\{ \mathbf{V} \left[\Pi^{(\lambda)}(iu) - \Pi^{(0)}(iu) \right] \right\} , \quad (2.86)$$

\mathbf{V} is the Coulomb kernel, $\Pi^{(0)}$ the KS-polarization propagator, which is used in publication I. One can use the Bethe-Salpeter equation [12, 14, 47, 65–67] as an analogue to the Dyson equation

$$\Pi^{(\lambda)}(iu) = \Pi^{(0)} + \Pi^{(0)}(iu) (\lambda\mathbf{V} + \mathbf{K}^{(\lambda)}(iu)) \Pi^{(\lambda)}(iu) . \quad (2.87)$$

\mathbf{K} denotes the XC-kernel. Alternative derivations employ the ring Coupled-Cluster approach [47, 68, 69], the plasmon equation [44], or the density-matrix-density-matrix response function [47, 65].

2.2 Solids

Ab initio quantum chemical methods play an integral part in the analysis of crystals and solids in chemistry. Advances both in theory as well as technology allow increasingly detailed insight in fields of catalysis and material science. Technological improvements, i.e., multi-core architectures and parallelization of code on graphical processors, open the door for more demanding calculations. The methodological challenges lie in the compromise between accuracy and (computational) demand. Highly accurate methods usually require a corresponding amount of mathematical operations resulting in an unfavorable scaling behavior. We can generally distinguish between two *ab initio* approaches in this context, wave-function based methods [6, 55] and density functional theory (DFT) [3, 4]. The first approach aims, as the name already implies, at solving the Schrödinger equation by approximating of the exact wave function. One of the most fundamental wave-function approaches is the Hartree-Fock or mean field approach [6, 55]. However, this method normally requires additional improvements to reach chemical accuracy. One favorable feature of the Fock-approach is, that it can be improved systematically to yield gradually more accurate results [6, 55]. This led to the 'gold standard' of numerical accuracy, the coupled-cluster approach, CCSD(T) coupled cluster with singles, doubles and perturbative triples excitations [6, 55, 70]. However the scaling behavior, i.e., the ratio between number of mathematical operations and system size with growing system size, inhibits the application to larger systems. An alternative to wave function based methods is DFT. DFT is based upon the electron density in contrast to the wave function, a reason for its comparable cheap computational cost [3, 4]. Density functionals designed for specific applications allow efficient treatment of electronic systems. For periodic systems, DFT may for example give insights into analysis of hydrogen storage materials [71] or zeolite supported chromium catalysts [72]. This chapter provides an overview of the general setup of periodic DFT calculation. It aims to outline the concepts and tools used to treat periodic boundary conditions (PBCs) with focus on the implementation in TURBOMOLE [73]. This section provides the basic theory for the original work in chapter 3 beginning with the concepts of density functional theory. The next two sections deal with the concept of crystal lattices and periodic basis functions under PBCs [21, 74]. The following section introduces periodic boundary conditions (PBCs) and Bloch-like Gaussian type orbitals (GTOs) in the DFT formalism [27, 28]. The last two sections deal with the adaption resolution of identity (RI) approach for periodic boundary conditions [24, 27, 75–78] and the continuous fast multipole method for infinite periodic systems [27, 29–35].

2.2.1 Density functional theory and Kohn-Sham formalism

This chapter recapitulates the standard DFT formalism as described in standard textbooks, e.g. Refs. [3–5]. As the name suggest, density functional theory relies on the determination of the

electron density instead of the electronic wave function. This leads to a significant reduction of variables (one position vector for the electron density in comparison to N_{el} electron coordinates for the wave function) and overall speedup of the method. The theoretical foundation for DFT was given by Hohenberg and Kohn [79], who directly established a one to one correspondence between the wave function and the electron density as well as the electron density and the external potential of a non-degenerate system. This finding can be rigorously extended to degenerate systems. It is therefore mathematically valid to replace the wave function by the electron density and vice versa [3–5]. The ground state energy [3–5]

$$E[\rho] = E_{el}[\rho] + E_{ext}[\rho] = T[\rho] + J[\rho] + E_{xc}[\rho] \text{ with } J[\rho] = E_H[\rho] + E_{ext} \quad (2.88)$$

can thus be written as a functional of the electron density ρ . The functional E_{el} contains the coupling between ρ and E_{ext} , the coupling between external potential and particles (electrons and nuclei in most cases). The single components of E_{el} are the kinetic energy T , the electronic Hartree or Coulomb interaction energy E_H and the exchange-correlation term E_{xc} . E_{xc} is defined by equation 2.88 and contains electron correlation and exchange energies. E_H and E_{ext} can be combined into the complete Coulomb interaction energy J . E_H and E_{ext} can be straightforwardly expressed as [3–5]

$$E_H[\rho] = \frac{1}{2} \iint dx dx' \rho(x) v(x, x') \rho(x'). \quad (2.89)$$

and

$$E_{ext}[\rho] = \int dx v_{ext}(x) \rho(x). \quad (2.90)$$

$v(x, x') = v(\mathbf{r}, \mathbf{r}') = \frac{1}{|\mathbf{r} - \mathbf{r}'|}$ is the Hartree kernel as introduced in section 2.1.3 and $v_{ext}(x)$ the external potential. Unfortunately the exact functional for the kinetic energy is not known. Kohn and Sham therefore formulated a different approach to T [2]. They proposed that for a given electron-electron-interacting system there exists a corresponding non-interacting system, whose ground state density is identical to the ground state density ρ_0 of the interacting system. This Kohn-Sham system is then expanded by a Kohn-Sham determinant Φ of orbitals ε . Φ is therefore a functional of ρ itself. The kinetic energy of the interacting system can thus be expressed by the non-interacting system as [2–5]

$$T = \langle \Phi | \hat{T} | \Phi \rangle, \quad (2.91)$$

where \hat{T} is the kinetic energy operator. The Kohn-Sham orbitals are constructed via a self-consistent field approach (SCF) out of a linear combination of atomic orbitals (LCAO) (see section 2.2.3 and 2.2.4). The Kohn-Sham ground state is characterized by the Kohn-Sham

potential

$$v_S[\rho](x) = v_{ext}(x) + v_H[\rho](x) + v_{xc}[\rho](x) \quad (2.92)$$

v_{ext} is the external potential from above, v_H the Hartree potential

$$v_H[\rho](x) = \int dx' v(x, x') \rho(x') \quad (2.93)$$

and v_{xc} the exchange-correlation potential

$$v_{xc}[\rho](x) = \frac{\delta E_{xc}[\rho]}{\rho(x)}. \quad (2.94)$$

v_{xc} has to be approximated by corresponding functionals. The complete Kohn-Sham equation in atomic units thus becomes

$$\left(-\frac{1}{2} \nabla^2 + v_s(x) \right) \varphi_i(x) = \varepsilon \varphi_i(x). \quad (2.95)$$

To determine the expansion coefficients C of the φ in terms of basis functions the SCF approach is necessary as v_s is itself dependent on ρ and consequently on the coefficients C . as v_s is itself dependent on ρ (see sections 2.2.3 and 2.2.4).

2.2.2 Crystal lattice

The three-dimensional periodic structure of crystals requires a systematic way of description. This section introduces the concept of the Bravais lattice to account for this translational symmetry. A three dimensional Bravais lattice is defined by all points accessible via the lattice translation vectors of the form [21, 22, 74]

$$\mathbf{L} = n_1 \mathbf{a}_1 + n_2 \mathbf{a}_2 + n_3 \mathbf{a}_3. \quad (2.96)$$

a_1 , a_2 and a_3 are the primitive vectors of the lattice and their corresponding prefactors n can assume any integer value. Leaving surface and similar effects aside the infinite Bravais lattice is a profound approximation for the interior of a macroscopic crystal. The concept of the Bravais lattice is however not confined to three dimensions. Lower dimensional periodic systems like films or nanowires may be analogously defined by a reduced set of lattice vectors. Let N_{dim} be the number of lattice vectors corresponding to the number of periodic directions then

$$\mathbf{L} = \sum_{N_{\text{dim}}}^l n_l \mathbf{a}_l. \quad (2.97)$$

Closely related to the concept of the Bravais lattice is the term of the primitive unit cell [21]. The primitive unit cell of a Bravais lattice is a volume of space, which does not overlap with any of its translated counterparts according to the Bravais lattice. As this definition allows to choose a multitude of possible geometries a more rigid and systematic definition is necessary in practical cases. The Wigner-Seitz unit cell is defined as the region of space closer to a chosen lattice point than to any other [21]. By filling the unit cell with atoms the final crystal lattice is constructed. It therefore combines the translation symmetry of the Bravais lattice with the point group symmetry of the single unit cell. Only special Bravais lattice and point group combinations are mathematically possible resulting in the 230 distinct space groups [21]. Each Bravais lattice is assigned a so called lattice in reciprocal space reciprocal lattice for short [21, 22, 74]. Given the definition of the (direct space) Bravais lattice the reciprocal lattice is defined as the lattice satisfying the relation

$$e^{i\mathbf{K}(\mathbf{L}+\mathbf{r})} = e^{i\mathbf{K}\mathbf{r}} . \quad (2.98)$$

\mathbf{K} is called the wave vector of the reciprocal lattice, i.e., the lattice vector of the reciprocal lattice [21, 22, 74]. The reciprocal lattice is therefore the set of all plane waves with the periodicity equal to the periodicity of the direct space Bravais lattice. It is in itself a Bravais lattice and its primitive vectors \mathbf{b}_i follow the relation [74]

$$a_i b_j = 2\pi \delta_{ij} . \quad (2.99)$$

For a three-dimensional Bravais lattice this results in the following primitive vectors

$$b_1 = 2\pi \frac{a_1 \times a_2}{\det(a_1 a_2 a_3)} \quad (2.100)$$

The Wigner Seitz cell in reciprocal space is called the first Brillouin zone (FBZ). This becomes especially important in the next sections as integration of the reciprocal space can normally be confined to the FBZ without loss of information [21, 74].

2.2.3 Basis functions under periodic boundary conditions

Following from the translation symmetry of crystals the single particle electron functions of a quantum chemical system have to fulfill special conditions, summarized under the Bloch theorem [21, 22, 74, 80]. It states that the translation of any wave function φ in accordance with the symmetry of the underlying Bravais lattice only leads to a change in phase

$$\varphi(\mathbf{r} + \mathbf{L}) = e^{i\mathbf{K}\mathbf{L}} \varphi(\mathbf{r}) . \quad (2.101)$$

φ might in this exemplary case be any single particle electronic wave function. The wave vector \mathbf{k} is often called crystal momentum [22]. Equivalently the electronic wave function can be expressed as combination of a lattice-periodic part u and a phase factor or plane wave part [21]

$$\varphi_{\mathbf{k}}(\mathbf{r}) = e^{i\mathbf{k}\mathbf{r}}u_{\mathbf{k}}(\mathbf{r}) . \quad (2.102)$$

Note that the expression above contains a wave vector \mathbf{k} , which can be seen as an additional 'quantum number'. To prove this point we apply Born von Karman periodic boundary conditions (PBCs) to a macroscopic but finite crystal [21]

$$\varphi(\mathbf{r}) = \varphi(\mathbf{r}_{N_i}\mathbf{a}_i) , \quad (2.103)$$

where N_i is equal or smaller to the number of primitive cells in this crystal direction. Then it directly follows from Bloch's Theorem that all \mathbf{k} have discrete values [21, 74]

$$\mathbf{k} = \sum_{i=1}^{N_{dim}} \frac{m_i}{N_i} \mathbf{b}_i . \quad (2.104)$$

m_i is an integer value and N_{dim} the number of periodic directions. The results from the Bloch theorem can be transferred to the constructions of basis sets. Under boundary conditions (PBC), two popular types of analytical basis functions, which fulfill the Bloch theorem, are *plane waves* and Bloch-like *local atom-centered basis functions*. *Plane waves* arouse early in the development of solid state physics since energy expressions resulting from this basis have a mathematically simple form and improvement of the basis is rather systematic, as the basis is orthogonal [22, 23]. In principle it expresses u in equation 2.102 by a linear combination of plane waves. A major drawback of *plane waves* is the large number of basis functions needed to describe atomic cores [22]. An accepted approach, that recovers efficiency, is the use of projector-augmented plane waves [81–86]. In this method part of the wave functions is replaced by a pseudo-potential, which reduces the number of basis functions significantly. Furthermore, as *plane waves* are inherently 3D periodic, 2D systems have to be treated as a crystal of slabs and may require additional decoupling schemes to prevent slab interactions.

The computational demand of plane wave methods for all-electron calculations and application in slabs, tubes, and molecules may be reduced by employing instead *atom-centered local basis functions*. They allow for explicit treatment of any number of periodic directions in the system and direct spatial screening of local interactions. All used methods in this work rely exclusively on *Gaussian type orbitals* (GTOs) as used in RIPER for this reason [24–28]. Speaking in terms of equation 2.102 the lattice periodic part u is now expanded in a linear combination of GTOs. Restructuring, summation over \mathbf{L} and normalization results in the form

of the basis functions used in paper **I** (see equation (25) to (27) in paper **I**)

$$\tilde{\varphi}_{\mathcal{P}}(\mathbf{r}) = \sum_{\mathbf{L}} \tilde{\varphi}_{\mathcal{P}}(\mathbf{r})^{\mathbf{L}} \text{ with } \tilde{\varphi}_{\mathcal{P}}(\mathbf{r})^{\mathbf{L}} = e^{i\mathbf{k}\mathbf{L}} \phi_{\mathcal{P}}^{\mathbf{L}}(\mathbf{r}), \quad (2.105)$$

where

$$\phi_{\mathcal{P}}^{\mathbf{L}}(\mathbf{r}) = \sum_{\mu} C_{\mu\mathcal{P}} \xi_{\mu}^{\mathbf{L}}(\mathbf{r}) \quad (2.106)$$

is a linear combination of atomic orbitals (LCAO) and $\mathcal{P} = (p, \mathbf{k}, \sigma)$ a compound index. $C_{\mu\mathcal{P}}$ are the expansion coefficients. p is the index of the contracted GTO, where μ indicates the primitive *Gaussian type Functions* (GTFs). Note that equation 2.105 and 2.106 are both valid for crystals and molecules and that the spin dependence is shifted to \mathcal{P} for clarity. The final functions are in general normalized with the number of unit cells N_{UC} within the crystal [27, 32, 86]

$$\varphi_{\mathcal{P}}(\mathbf{r}) = \frac{1}{N_{UC}} \tilde{\varphi}_{\mathcal{P}}(\mathbf{r}). \quad (2.107)$$

Disadvantages of GTOs are the *basis set superposition error* (BSSE) [87] and linear dependencies due to the construction of periodic functions out of GTOs [88]. Linear dependencies can be eliminated via design [88, 89] or projection of the basis set [90]. Use of carefully designed numerical local basis function (NAOs) can reduce BSSE and linear dependency by construction [91]. The full benefits from employing adaptive local basis sets were discussed by Schütt et al. [92]

2.2.4 Density functional theory under periodic boundary conditions

We can now combine the periodic GTOs in equations 2.105, 2.106 and 2.107 (or respectively the equivalent equations (25) until (27) in paper **I**) with the Kohn-Sham equation 2.95 from section 2.2.1. This ultimately results in the following matrix equation [27, 28, 32, 34]

$$\mathbf{F}_{\sigma}^{\mathbf{k}} \mathbf{C}_{\sigma}^{\mathbf{k}} = \mathbf{S}^{\mathbf{k}} \mathbf{C}_{\sigma}^{\mathbf{k}} \boldsymbol{\varepsilon}_{\sigma}^{\mathbf{k}}, \quad (2.108)$$

which is decoupled for every \mathbf{k} and σ . Once again the spin is given here as an extra index for clarity. $\mathbf{F}^{\mathbf{k}}$ is the Kohn-Sham matrix, $\mathbf{S}^{\mathbf{k}}$ the overlap matrix, $\boldsymbol{\varepsilon}^{\mathbf{k}}$ the one particle energy matrix of the atomic orbitals and $\mathbf{C}^{\mathbf{k}}$ the coefficient matrix all of them in reciprocal space. The real space matrices $\mathbf{M}^{\mathbf{L}}$ can be obtained via the Fourier transform of the reciprocal matrices $\mathbf{M}^{\mathbf{k}}$.

To prove this, consider a generic matrix element $M_{\mathcal{P}\mathcal{Q}}^{\mathbf{k}}$ with an operator \hat{O} [27, 34]

$$\begin{aligned}
M_{\mathcal{P}\mathcal{Q}}^{\mathbf{k}} &= \langle \varphi_{\mathcal{P}} | \hat{O} | \varphi_{\mathcal{Q}} \rangle = \left\langle \frac{1}{\sqrt{N_{UC}}} \sum_{\mathbf{L}'} \left(e^{i\mathbf{k}\mathbf{L}'} \phi_{\mathcal{P}}^{\mathbf{L}'} \right) \middle| \hat{O} \middle| \frac{1}{\sqrt{N_{UC}}} \sum_{\mathbf{L}} e^{i\mathbf{k}\mathbf{L}} \phi_{\mathcal{Q}}^{\mathbf{L}} \right\rangle = \\
&= \sum_{\mathbf{L}'} e^{-i\mathbf{k}\mathbf{L}'} \left\langle \frac{1}{\sqrt{N_{UC}}} \phi_{\mathcal{P}}^{\mathbf{L}'} \middle| \hat{O} \middle| \frac{1}{\sqrt{N_{UC}}} \sum_{\mathbf{L}} e^{i\mathbf{k}\mathbf{L}} \phi_{\mathcal{Q}}^{\mathbf{L}} \right\rangle = \\
&= \left\langle \frac{N_{UC}}{\sqrt{N_{UC}}} \phi_{\mathcal{P}}^{\mathbf{0}} \middle| \hat{O} \middle| \frac{1}{\sqrt{N_{UC}}} \sum_{\mathbf{L}} e^{i\mathbf{k}\mathbf{L}} \phi_{\mathcal{Q}}^{\mathbf{L}} \right\rangle = \\
&= \langle \phi_{\mathcal{P}}^{\mathbf{0}} | \hat{O} | \sum_{\mathbf{L}} e^{i\mathbf{k}\mathbf{L}} \phi_{\mathcal{Q}}^{\mathbf{L}} \rangle = \\
&= \sum_{\mathbf{L}} e^{i\mathbf{k}\mathbf{L}} \langle \phi_{\mathcal{P}}^{\mathbf{0}} | \hat{O} | \phi_{\mathcal{Q}}^{\mathbf{L}} \rangle = \\
&= \sum_{\mathbf{L}} e^{i\mathbf{k}\mathbf{L}} M_{\mathcal{P}\mathcal{Q}}^{\mathbf{L}} \tag{2.109}
\end{aligned}$$

Be aware that the indices \mathcal{P} and \mathcal{Q} in the equation above now explicitly exclude \mathbf{k} but can include the spin. The (real-space) Kohn-Sham matrix

$$\mathbf{F}_{\sigma}^{\mathbf{L}} = \mathbf{T}^{\mathbf{L}} + \mathbf{J}^{\mathbf{L}} + \mathbf{X}_{\sigma}^{\mathbf{L}} \tag{2.110}$$

consists of three different contributions, the kinetic energy matrix \mathbf{T} , the exchange-correlation matrix \mathbf{X} and the Coulomb matrix \mathbf{J} . The operators for the corresponding matrices are defined by the components of the KS-potential in equations 2.92, 2.93, 2.94 and 2.95. The kinetic energy operator in atomic units is [25]

$$\hat{t} = \frac{1}{2} \nabla^2 = \frac{1}{2} \Delta, \tag{2.111}$$

the Coulomb operator is [25]

$$\hat{j}[\rho] = \int \frac{\rho(\mathbf{r}') - \rho_n(\mathbf{r}')}{|\mathbf{r} - \mathbf{r}'|} d\mathbf{r}' \text{ with } \rho_n(r) = \sum_{a\mathbf{L}} Z_a \delta(\mathbf{r} - \mathbf{R}_a + \mathbf{L}) \tag{2.112}$$

and the exchange-correlation operator v_{xc} is defined via the density functional. Note that the Coulomb operator both contains the electron density ρ and the external charge distribution ρ_n , i.e., the interaction with the external potential of point charges a (atoms, ghost charges, etc.) with charges Z_a . The solution of equation 2.108 leads to the density matrix in reciprocal space [25, 27, 32]

$$D_{\mu\nu\sigma}^{\mathbf{k}} = \sum f_{p\sigma}^{\mathbf{k}} (C_{\mu p\sigma}^{\mathbf{k}})^* C_{\nu p\sigma}^{\mathbf{k}}. \tag{2.113}$$

$f_{p\sigma}$ are occupation numbers and either one or zero for occupied or unoccupied orbitals, μ, ν are indices of the primitive GTFs. The direct space density matrix is obtained via the integration

over the first Brillouin zone (FBZ) [27, 32]

$$D_{\mu\nu\sigma}^{\mathbf{L}} = \frac{1}{V_k} \int_{\text{FBZ}} D_{\mu\nu\sigma}^{\mathbf{k}} e^{i\mathbf{k}\mathbf{L}} d\mathbf{k}, \quad (2.114)$$

where V_k is the volume of the FBZ. For integration and summation over \mathbf{k} in the FBZ see equations (56) and (57) in paper I. Metallic systems may additionally require Fermi smearing in this context [93]. The complete energy per unit cell thus becomes

$$E^{\text{UC}} = \sum_{\mu\nu\sigma\mathbf{L}} D_{\mu\nu\sigma}^{\mathbf{L}} T_{\mu\nu}^{\mathbf{L}} + E_{xc} + J. \quad (2.115)$$

All equations are valid for molecules with $\mathbf{k} = \mathbf{0}$ and $\mathbf{L} = \mathbf{0}$. In TURBOMOLE the complete Fock matrix is constructed in direct space, transformed into reciprocal space and the SCF approach is used to solve equation 2.108. The density matrix in reciprocal space can then be re-transformed into direct space and to calculate the energy [27, 28, 32, 94]. However several issues arise due to the periodic nature of the electronic system. First, as shown in equation 2.114, integration over the complete FBZ has to be performed. In theory this would require an infinite number of \mathbf{k} points as an analytical evaluation is impossible. This problem can be solved by performing the integration on a grid of \mathbf{k} points i.e., a finite and carefully chosen number of \mathbf{k} -points. The grid used in this work [27] is based on the work of Monkhorst and Pack [74, 95, 96]. Special points of higher symmetry like the origin of the reciprocal lattice, the totally symmetric or Γ -Point, are subject of consideration as well [21]. Another problem for periodic calculations arises from the sums over all lattice vectors \mathbf{L} . For a 1D and 2D periodic system these lattice sums do not pose a problem. However, Stolarczyk and Piela [97] showed, that the lattice sums contained in equation 2.108 and 2.115 and the elements therein only converge for 3D periodic systems if the overall charge and dipole moment of the unit cell is zero. This makes a dipole correction to the unit cell necessary for 3D periodic systems [27, 33, 34]. The single components of equation 2.115 therefore require special attention in their evaluation. The Coulomb interaction J is efficiently treated via a multipole method [24, 27, 29–35] (see section 2.2.6) and accelerated by an adapted resolution of the identity (RI) [24, 27, 75–77, 98] approach (see section 2.2.5). E_{xc} can be treated by a hierarchical scheme [25]. Only T can be evaluated analogously to the molecular case [27].

For the following chapters E_{xc} containing true Fock-exchange is explicitly excluded. Treatment of the Fock-exchange requires additional treatment of finite size errors in the real space density matrix. These errors stem from an unphysical periodicity of the real space density matrix due to the use of finite k grids [99, 100]

$$D_{\mu\nu\sigma}^{\mathbf{L}} = D_{\mu\nu\sigma}^{\mathbf{L}+\mathbf{L}_{SC}}, \quad (2.116)$$

where \mathbf{L}_{SC} is a supercell vector in real space corresponding to the structure of the k grid in reciprocal space [99]. Truncation of the Coulomb interaction [101] or a Minimum Image Convention approach [102] overcomes this problem by avoiding the unphysical interactions [99].

2.2.5 Resolution of identity under periodic boundary conditions

For molecular calculations the resolution of identity (RI) [78, 103, 104] approach is a frequently used tool to reduce the computational cost for the Coulomb energy calculation by an order of magnitude. This section recalls the procedure to transfer this method to periodic systems as done in TURBOMOLE [24, 27, 75–77, 98]. It is therefore the foundation for section 2.2.6 and paper I. Consider the total Coulomb energy of a system

$$J = \frac{1}{2} (\rho^0 - \rho_n | \rho - \rho_n) , \quad (2.117)$$

where the complete ground state electron density

$$\rho_0 = \sum_{\mathbf{L}} \rho^{\mathbf{L}} \text{ with } \rho^{\mathbf{L}} = \sum_{\mu\nu\mathbf{L}'\sigma} D_{\mu\nu\sigma}^{\mathbf{L}'} \mu_{\mathbf{L}}(\mathbf{r}) \nu_{\mathbf{L}}(\mathbf{r} - \mathbf{L}') \quad (2.118)$$

is expressed as a sum over the single cell contributions $\rho^{\mathbf{L}}$. Be aware that $\mu_{\mathbf{L}} = \xi_{\mu}(\mathbf{r} - \mathbf{L} - \mathbf{R}_{\mu})$ with atomic position vector \mathbf{R}_{μ} . $\rho - \rho_n$ is the complete charge density for the crystal. The resolution of identity (RI) or density fitting approach replaces the electron density on the right part of the integral by a fitted density [24, 27, 75]

$$\rho_0 \approx \tilde{\rho} = \sum_{\mathbf{L}} \tilde{\rho}^{\mathbf{L}} \text{ with } \tilde{\rho}^{\mathbf{L}} = \sum_{\alpha} c_{\alpha} \alpha_{\mathbf{L}} = \mathbf{c}^T \boldsymbol{\alpha}_{\mathbf{L}} . \quad (2.119)$$

which is constructed out of a linear combination of atom-centered auxiliary GTOs α and the corresponding coefficients c_{α} . The error of the RI-approach is reduced by minimizing the Coulomb self-interaction

$$D = \left(\delta\rho^0 | \sum_{\mathbf{L}} \delta\rho^{\mathbf{L}} \right) = \left(\rho^0 - \tilde{\rho}^0 \left| \sum_{\mathbf{L}} \rho^{\mathbf{L}} - \tilde{\rho}^{\mathbf{L}} \right. \right) \quad (2.120)$$

of the residual density $\delta\rho^{\mathbf{L}} = \sum_{\mathbf{L}} \rho^{\mathbf{L}} - \tilde{\rho}^{\mathbf{L}}$ [24, 27, 75]. However, molecular RI basis sets contain functions with non-vanishing monopole moments, i.e., charged functions. These contributions result in divergent a lattice sum in equation 2.117 and 2.120. Instead of using crystal basis sets [89, 105], which circumvent these functions, TURBOMOLE uses a different

approach. The auxiliary density is split into two contributions

$$\tilde{\rho} = \tilde{\rho}_{\perp} + \tilde{\rho}_{\parallel} \text{ with } \int \tilde{\rho}_{\perp} dr = 0 \text{ and } \int \tilde{\rho}_{\parallel} dr = N_{el} \quad (2.121)$$

a charged part ρ_{\parallel} and an uncharged part ρ_{\perp} . N_{el} is the number of electrons. Each part has its own set of coefficients

$$\mathbf{c} = \mathbf{c}_{\perp} + \mathbf{c}_{\parallel} \text{ with } \tilde{\rho}_{\perp} = \mathbf{c}_{\perp}^T \alpha \text{ and } \tilde{\rho}_{\parallel} = \mathbf{c}_{\parallel}^T \alpha, \quad (2.122)$$

which together yield the original coefficient matrix. The coefficients are projected from the complete coefficient matrix by the projection matrices \mathbf{P}_{\parallel} and \mathbf{P}_{\perp}

$$\mathbf{c}_{\parallel} = \mathbf{P}_{\parallel} \mathbf{c} \text{ and } \mathbf{c}_{\perp} = \mathbf{P}_{\perp} \mathbf{c}. \quad (2.123)$$

Let \mathbf{q} be a charge vector of dimension N_{aux} containing all charges of the auxiliary densities. Then the projection matrices are defined via the normalized charge vector

$$\mathbf{n} = \frac{\mathbf{q}}{|\mathbf{q}|} \text{ with } \mathbf{q} = (q_1, q_2, \dots) \text{ and } q_{\alpha} = \int \alpha(\mathbf{r}) dr \quad (2.124)$$

as

$$\mathbf{P}_{\parallel} = \mathbf{n} \mathbf{n}^T \text{ and } \mathbf{P}_{\perp} = \mathbf{1} - \mathbf{n} \mathbf{n}^T. \quad (2.125)$$

The charged part of the auxiliary density can then be expressed as

$$\mathbf{c}_{\parallel} = \frac{N_{el}}{|\mathbf{q}|} \mathbf{n}. \quad (2.126)$$

The uncharged density can be solved by minimization of $\frac{\partial D}{\partial \mathbf{c}_{\perp}} = 0$, which leads to

$$(\mathbf{V}_{\perp} + \mathbf{P}_{\parallel}) \mathbf{c}_{\perp} = \boldsymbol{\varsigma} \text{ with } \mathbf{V}_{\perp} = \mathbf{P}_{\perp} \mathbf{V} \mathbf{P}_{\perp} \text{ and } \boldsymbol{\varsigma} = \left(\rho_0 - \tilde{\rho}_0 \left| \mathbf{P}_{\perp} \sum_{\mathbf{L}} \alpha_{\mathbf{L}} \right. \right). \quad (2.127)$$

The elements of \mathbf{V} contain the electron repulsion integrals of the form $V_{\alpha\beta} = (\alpha_0 | \sum_{\mathbf{L}} \beta_{\mathbf{L}})$, where β is an index for the auxiliary functions as well. Due to the charge projection, the charged part of the auxiliary basis set can be removed from the lattice sums. Using the RI-J approximation [106] the final Coulomb energy is then [24, 25]

$$J = \sum_{\mu\nu\mathbf{L}} D_{\mu\nu}^{\mathbf{L}'} J_{\mu\nu}^{\mathbf{L}} - \frac{1}{2} \left(\tilde{\rho}_0 + \rho_{n0} \left| \sum_{\mathbf{L}} \tilde{\rho}_{\mathbf{L}} - \rho_{n\mathbf{L}} \right. \right) \quad (2.128)$$

with the Coulomb matrix element

$$J_{\mu\nu}^{\mathbf{L}} = \left(\mu_0 \nu_{\mathbf{L}} \left| \sum_{\mathbf{L}'} \tilde{\rho}^{\mathbf{L}'} - \rho_n^{\mathbf{L}'} \right. \right). \quad (2.129)$$

2.2.6 Continuous Fast Multipole Method under Periodic boundary conditions

Evaluation of the Coulomb energy in equation 2.128 faces the serious problem of infinite lattice sums over \mathbf{L} . As a straight forward summation is slowly converging, an elaborate scheme has to be used to speed up summation. This section introduces the continuous fast multipole method (CFMM) as a solution to this problem as used in TURBOMOLE [73] for evaluation of the Coulomb matrix [24, 27, 29, 31–35]. This chapter is the prerequisite for the complex density adapted CFMM formalism in paper I, appendix A, as well as the calculation of the electrostatic potential in section 3.3. We start with the evaluation of a general Coulomb integral of the form $\sum_{\mathbf{L}} (\rho_1 | \rho_2^{\mathbf{L}})$ for the non-complex local charge density ρ_1 and periodic charge density $\rho_2^{\mathbf{L}}$, which typically arises for periodic calculations. The densities can in fact be point charges, shell pairs, auxiliary functions, additional ghost charges, etc. The FMM is based on the assumption, that the Coulomb interaction between two charge densities ρ_1 and ρ_2 can be evaluated via the multipole expansion [6, 27, 29]

$$J(\rho_1, \rho_2) = M^{\rho_1} \odot L^{\rho_2^{\mathbf{L}}} = \sum_{l=0}^{l_{max}} \sum_{m=-l}^l M_{lm}^{\rho_1} L_{lm}^{\rho_2^{\mathbf{L}}} \quad (2.130)$$

as long as the two charges are well-separated, i.e., as long as the sum of extents ϵ of both charges is smaller than the distance between the charge centers \mathbf{r}_1 and \mathbf{r}_2 , i.e.,

$$|\mathbf{r}_1 - \mathbf{r}_2| > \epsilon_P + \epsilon_q. \quad (2.131)$$

M^{ρ_1} is the multipole or external moment of ρ_1 and $L^{\rho_2^{\mathbf{L}}}$ the Taylor or local moment of $\rho_2^{\mathbf{L}}$ both evaluated at the same center of origin. Definition of extents and charge centers for GTOs and shellpairs can be found in the work of Lazarski et al. [27] The lattice sum is now divided into a crystal near field (CNF) and crystal far field (CFF) part

$$\sum_{\mathbf{L}} (\rho_1 | \rho_2^{\mathbf{L}}) = \sum_{\mathbf{L} \in \text{CFF}} (\rho_1 | \rho_2^{\mathbf{L}}) + \sum_{\mathbf{L} \in \text{CNF}} (\rho_1 | \rho_2^{\mathbf{L}}). \quad (2.132)$$

We first consider the evaluation of the CFF part, which follows the recurrence scheme of Kudin and Scuseria [31]. It defines a multipole to local operator (M2L) [6, 27, 29, 31],

$$L(\mathbf{r}' - \mathbf{r}) = \mathcal{L}(\mathbf{r}) \otimes M(\mathbf{r}'), \quad (2.133)$$

which transforms a multipole moment $M(\mathbf{r}')$ at expansion center \mathbf{r}' to a local moment L^ρ at expansion center $(\mathbf{r}' - \mathbf{r})$. $\mathcal{L}(\mathbf{r})$ is the uncontracted Taylor moment of a single point charge evaluated at the origin and positioned at \mathbf{r} . Let M^{ρ_2} be the multipole moment of the ρ_2^0 , who is located at the central unit cell. This unit cell is not necessarily identical to its crystallographic definition. Then the Taylor moment generated by all $\rho_2^{\mathbf{L} \in CFF}$ in the local cell can be calculated by [31]

$$L^{\rho_2^{\mathbf{L}}} = \sum_{\mathbf{L} \in CFF} \mathcal{L}(\mathbf{L}) \otimes M^{\rho_2} = \mathcal{L}^{CFF} \otimes M^{\rho_2}. \quad (2.134)$$

\mathcal{L}^{CFF} can be evaluated using a recurrence relation [31]. In the first step a $3 \times 3 \times 3$ supercell is constructed, which has the unit cell at its center (see paper I, appendix A, for a depiction of this process). Then the Taylor moment (\mathbf{L}) of every cell according to equation 2.134 is accumulated, which is in the CFF of the unit cell but in the near-field of the supercell. We call this region CFF' . In the next step the $3 \times 3 \times 3$ supercell is used as the new basis for the construction of a $3^2 \times 3^2 \times 3^2$ supercell. The corresponding (\mathbf{L}) are summed up and the process is repeated until convergence is reached. This procedure can be written as [31]

$$\mathcal{L}^{CFF} = \sum_{t=0}^{\infty} \mathcal{L}_t \quad (2.135)$$

$$\mathcal{L}_0 = \sum_{\mathbf{L} \in CFF'} \mathcal{L}(\mathbf{L}) \quad (2.136)$$

$$\mathcal{L}_{t+1} = \mathcal{U}_\theta(\mathcal{L}_t) \otimes \omega^{SC} + \mathcal{L}_0. \quad (2.137)$$

ω^{SC} contains the information for the translation of the multipole moments for the $3^1 \times 3^1 \times 3^1$ cell [31] and \mathcal{U}_θ is a rescaling operator, which stretches \mathcal{L}_t to the $(t + 1)$ th supercell. \mathcal{L}^{CFF} is computed only once during the SCF and is only dependent on the geometry of the unit cell. More information can be found in the literature especially for the TURBOMOLE implementation [24, 27, 29–35]. In paper I appendix A a revised CFMM method is shown adapted for the calculation of a complex ρ_2 . The remaining densities in the CNF are located in infinite, enclosed space. Therefore any molecular method can be used to speed up the calculation of the CNF. TURBOMOLE employs the molecular CFMM in this context, which should be outlined in the following section [27]. It is based on the boxing scheme of White and Head-Gordon [107] and is optimized for usage in crystals. It essentially divides the CNF into a hierarchical system of boxes, the so called octree (see figure 2.2). The boxes are constructed by defining a cubic box containing all ρ_1 and ρ_0 and dividing the box and its consecutive children boxes by half. Each division defines a new lower level of the octree. A box is defined as a parent to a one level lower box, if the lower box is contained within the parent box. The lower level box is called a child of the parent box. All boxes are then filled with the densities ρ_1 and ρ_0 in such a way, that each density is located within one box starting with the smallest low level boxes and rising in level until a sufficient large box is found. Aggregation of densities in specific

boxes is avoided by the introduction of a target number n_{tag} of densities per lowest level box. The octree is then replicated for every $\rho_{\mathbf{L} \neq 0}$ in the CNF and spread across the complete CNF. The CNF itself is then divided into a near-field (NF) and a far-field (FF) contribution. The FF contribution is then evaluated by the multiple expansion. This procedure is outlined below as depicted in [27]. In the first step the multipole expansion for ρ_1 and ρ_{20} are calculated for each box with regard to its box center. The multipole moment of ρ_{20} is translated upward the octree by a multipole to multipole (M2M) operator P (see figure 2.2a). After this step every parent box contains the complete information of the moments of its children and itself. In step 2 the multipole moments of $\rho_{2\mathbf{L}}$ are transformed into Taylor moments at centers of remote boxes at the same octree level (see figure 2.2b) by applying the multipole to local operator (M2L) Q . This is done for every non-well-separated box, whose parents are well separated. Two boxes i and j are well-separated if their cell center distance d_{ij} satisfies [27, 29]

$$d_{ij} \geq \text{WS} * \frac{\mathbf{D}_i - \mathbf{D}_j}{2}, \quad (2.138)$$

where WS is an integer well-separateness criterion and L_i the length of box i . This translation is also applied to every periodic image of the octree. Efficient grouping over Q for the periodic images allows for a significant speedup of the method [27]. The Taylor moments are then passed down the octree with the local to local operator (L2L) L (see figure 2.2c). Every box then contains all Taylor moments of higher level parent boxes for $\rho_{2\mathbf{L}}$ and $\mathbf{L} \in \text{FF}$. In the third step the Taylor moments of $\rho_{2\mathbf{L}}$ are contracted box-wise with the multipole moments of ρ_1 to yield the FF contributions for $(\rho_1 | \rho_2^{\mathbf{L}})$. The remaining NF contributions to $(\rho_1 | \rho_2^{\mathbf{L}})$ are calculated by direct integral evaluation in the last step of the CFMM. Originally the CFMM is used in TURBOMOLE to calculate the Coulomb matrix for the DFT energy [27]. It is combined with the RI approach in section 2.2.5, termed the density fitting accelerated CFMM (DF-CFMM) [27]. ρ_1 therefore contains the sum of screened shellpairs, whereas the periodic-density $\sum_{\mathbf{L}} \rho_2^{\mathbf{L}}$ contains the auxiliary functions from RI and the atomic charges. The RI approach combined with the replication of the octree for $\mathbf{L} \in \text{FF}$ allows for an efficient $\mathcal{O}(N)$ scaling calculation of the DFT energy. This method is adapted for the use of complex $\rho_{2\mathbf{L}}$ in paper I, appendix A, as well as the calculation of the electrostatic potential (ESP) in section 3.3, where $\rho_{2\mathbf{L}}$ now contain shell pairs and atomic charges, whereas ρ_1 contain the ESP point charges.

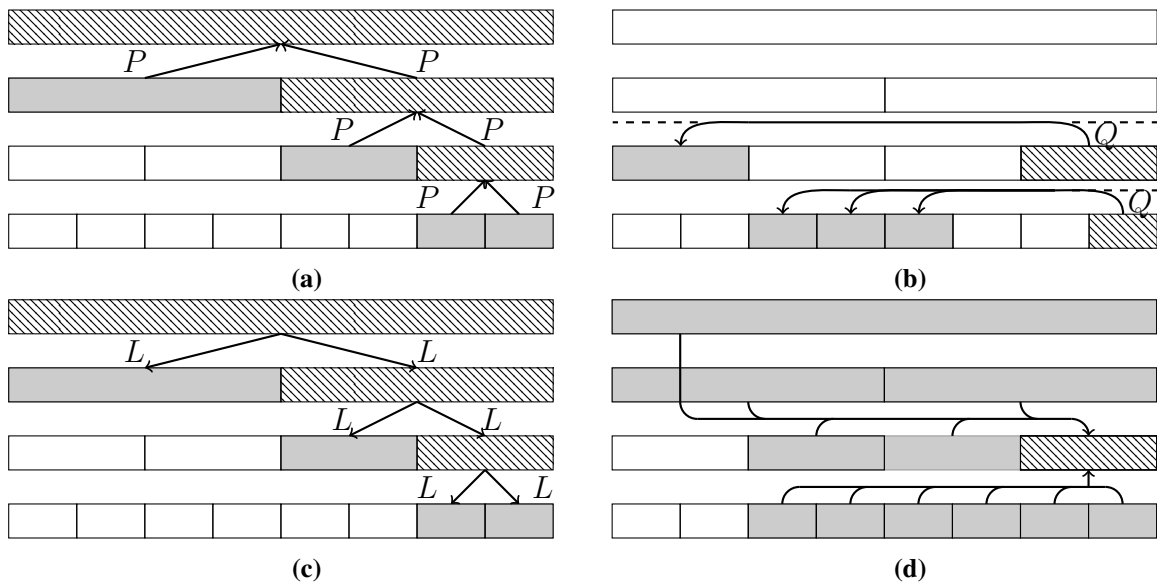


Figure 2.2: Scheme for the CFMM for the calculation of $(\rho_1 | \rho_2^L)$ (based on depictions in [27, 29]). The octree levels are represented by 1D box lines. A well-separateness (WS) criterion of $WS = 3$ is assumed. **(a)** Calculation of the multipole moments of ρ_1 and ρ_2^L and their shift upwards the octree with the M2M operator P . P is applied throughout the octree, however only one parent box (hatched) is exemplary shown for the upward shift for each octree level. **(b)** M2L translation by Q of the multipole moments of ρ_2^L for well-separated boxes with $WS = 3$. Dashed lines indicate translation to replicated octrees with $\mathbf{L} \neq \mathbf{0}$. Once again only one parent box is shown per level. **(c)** Downwards passing of Taylor moments via the L2L operator L . **(d)** Calculation of NF contributions to $(\rho_1 | \rho_2^L)$ for one box (hatched) for $WS = 3$.

3

Publications and results

The following chapter contains the original work of this thesis. Paper **I** is the central part of this work and focuses on the development of an RPA formalism under periodic boundary conditions. The primary work of the author of this thesis was the implementation and test of the Γ -point RPA implementation. In paper **II** the conversion of an imine- into a thiazole linked covalent organic framework is examined. The author of this thesis provides the periodic structure calculation in this context. Part **III** contains additional unpublished results about the periodic implementation of the electrostatic potential for RIPER in TURBOMOLE. Papers are given in their original formatting.

- I. Grundei, Martin M. J.; Burow, Asbjörn M.; Random Phase Approximation for Periodic Systems Employing Direct Coulomb Lattice Summation, *J. Chem. Theory Comput.* **2017**, 13, 1159–1175. ¹
- II. Haase, Frederik; Troschke, Erik; Savasci, Gökçen; Banerjee, Tanmay; Duppel, Viola; Dörfler, Susanne; Grundei, Martin M. J.; Burow, Asbjörn M.; Ochsenfeld, Christian; Kaskel, Stefan; Lotsch, Bettina V.; Topochemical conversion of an imine- into a thiazole-linked covalent organic framework enabling real structure analysis, *Nature Communications* **2018**, 9, 2600 ²
- III. Additional project: Implementation of the periodic electrostatic potential using local basis functions and the continuous fast multipole method

¹Reprinted (adapted) with permission. Copyright 2017 American Chemical Society.

²Published under the Creative Commons Attribution 4.0 International License, see <http://creativecommons.org/licenses/by/4.0/>. No changes made to the original article.

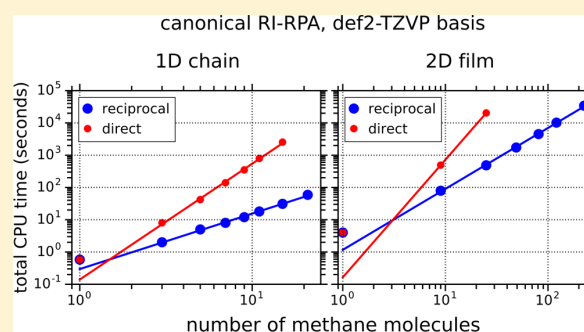
Random Phase Approximation for Periodic Systems Employing Direct Coulomb Lattice Summation

Martin M. J. Grundei and Asbjörn M. Burow*¹

Department of Chemistry, Ludwig-Maximilians-Universität (LMU) Munich, Butenandtstrasse 7, D-81377 Munich, Germany

S Supporting Information

ABSTRACT: A method to compute ground state correlation energies from the random phase approximation (RPA) is presented for molecular and periodic systems on an equal footing. The supermatrix representation of the Hartree kernel in canonical orbitals is translation-symmetry adapted and factorized by the resolution of the identity (RI) approximation. Orbital expansion and RI factorization employ atom-centered Gaussian-type basis functions. Long ranging Coulomb lattice sums are evaluated in direct space with a revised recursive multipole method that works also for irreducible representations different from Γ . The computational cost of this RI-RPA method scales as $O(N^4)$ with the system size in direct space, N , and as $O(N_k^2)$ with the number of sampled k -points in reciprocal space, N_k . For chain and film models, the exploration of translation symmetry with 10 k -points along each periodic direction reduces the computational cost by a factor of around 10–100 compared to equivalent Γ -point supercell calculations.



1. INTRODUCTION

An increasing number of recent works^{1–5} uses the random phase approximation (RPA) of the polarization propagator as an important component in developing improved orbital-based correlation energy functionals that remedy the shortcomings of traditional semilocal and hybrid density functional theory (DFT) approaches.

In fact, the RPA per se is one of the oldest nonperturbative methods for computing the ground state correlation energy of many-electron systems, and excellent reviews are found in the literature.^{6–8} In early works, RPA and equivalent methods were developed to calculate ground state correlation energies of the uniform electron gas and jellium models.^{9–17} Over the last decades, the concept of the adiabatic connection^{17–19} (AC) combined with the fluctuation–dissipation (FD) theorem^{20–22} led to a general and formally exact expression of the many-electron correlation energy. A recent classification of different ACFD formulations is discussed in ref 23. Using ACFD theory from the DFT perspective, the correlation energy may be expressed in terms of the causal polarization propagator,²⁴ which may be represented, via the Bethe–Salpeter equation,^{25,26} in terms of the Kohn–Sham (KS) polarization propagator, the Hartree kernel, and the dynamic (frequency-dependent) exchange–correlation kernel.^{27–32} If the exchange–correlation kernel is neglected in the propagator, then the RPA emerges as zero-order approximation to ACFD theory. In terms of accuracy, major benefits of RPA are the parameter-free inclusion of dispersive long ranging interactions and the nondivergent behavior for small gap systems and metals. RPA has been extensively tested for small systems,^{1,33–39} and unit

cells^{40–44} and RPA data of more complex systems^{45–52} were published in the last years (see also the citations in refs 6, 7, and 8). In summary, relative energies of conformers, molecular equilibrium structures, lattice constants, bulk moduli, and reaction energies improve in comparison to semilocal and hybrid DFT approximations though binding energies are underestimated compared to highly accurate reference data, and bond dissociation can exhibit nonphysical features, as often demonstrated for diatomics. Recent developments within RPA include analytical gradients,^{3,38,53} the implementation of quasi-relativistic two-component methods,⁵⁴ and low-scaling implementations.^{55–59}

Published works on developments and applications of ACFD correlation energy approximations beyond RPA increase rapidly and exceed the scope of the present work.^{60–66} In addition, there are approximations derived from ACFD theory, which impose stronger restrictions to the electronic degrees of freedom than RPA does and lead to very efficient methods to model dispersion effects.^{67–69} Probably one of the most applied models for van der Waals interactions in DFT calculations is Grimme’s dispersion correction.⁷⁰

RPA-based methods belong to the fifth rung in the Jacob’s ladder classification of DFT,⁷¹ and their computational demand is therefore much larger compared to popular DFT methods. Reducing this computational cost by clever transformations and evaluation schemes is a prerequisite to conducting practical RPA calculations. The conventional evaluation cost of RPA

Received: November 23, 2016

Published: February 9, 2017

employing the plasmon formula³² or a direct ring coupled cluster doubles approach⁷² (drCCD) scales as $O(N^6)$ with the system size N . This may be improved to $O(N^5)$ by using iterative sign function methods.³² Further reduction of the scaling behavior to $O(N^4)$ in the number of floating-point operations (FLOP) and to $O(N^3)$ in the required memory are achieved by the resolution of the identity (RI) technique based on the Coulomb-metric.^{40,73,74} Using Coulomb-metric RI, it was suggested that the amplitudes in the drCCD approach to RPA can also be obtained with $O(N^4)$ cost.⁷³ Effective linear scaling was recently demonstrated with a double Laplace transform ansatz combined with overlap-metric RI.⁵⁸ Large orbital basis sets are required for RPA correlation energies close to the complete basis set (CBS) limit.^{32,35} This is typical for correlated electronic structure methods⁷⁵ and leads to enormous prefactors in the computational cost. Explicitly correlated approaches circumvent this problem; excellent modern reviews are found in refs 76, 77, and 78. Existing RPA-F12 methods were established via the drCCD route.^{79,80}

Contemporary work on ACFD-RPA methods based on plane waves can be found in refs 81–83. RPA subject to periodic boundary conditions (PBC) is also part of implementations, which use projector augmented plane waves (PAW),⁴¹ grid-based PAW,⁴⁹ and orbital basis sets of Gaussian-type functions (GTF) mixed with grid-based auxiliary plane waves⁴² or with a grid-free analytical Fourier-transform variant.⁵⁹ These methods make use of RI in the plane wave basis and thus scale at most as $O(N^4)$ in the number of FLOP. Cubic scaling may be achieved^{55,59} and explicit use of virtual orbitals can be avoided.⁴⁴

There are attempts to make RI-RPA more efficient employing the local nature of GTF and other types of local atomic functions.^{58,59,84} RI techniques, also called density fitting, based on local basis functions were first developed to speed up the calculation of the Coulomb term in molecular self-consistent field (SCF) methods.^{85–88} Implementations of correlated approaches such as RI-MP2,⁸⁹ RI-CCSD,⁹⁰ and RI-RPA⁷³ followed later. In the rest of this article, we will only discuss Coulomb-metric RI if not stated otherwise and simply use the term “RI” from now on. It was shown that the RI error is quadratic in SCF Coulomb and RPA correlation energies.^{73,86,87} This means that the RI-approximated SCF Coulomb energy is a variational lower bound of the SCF Coulomb energy, as can be clearly seen, for example, from eq 44 in ref 91. The RI approximation to the RPA correlation energy is a variational upper bound neglecting RI effects in the underlying SCF reference.⁷³ In general, variational RI approaches are robust and yield accurate energies with moderately sized auxiliary basis sets.⁷³

Additional challenges arise for RI methods in solids due to the long-range lattice sums in the Coulomb-metric matrix^{91,92}

$$J_{PQ}(\mathbf{q}) = \sum_{\mathbf{L}} e^{i\mathbf{q}\cdot\mathbf{L}} \iint d^3r d^3r' \frac{\eta_P(\mathbf{r} - \mathbf{R}_P) \eta_Q(\mathbf{r}' - \mathbf{R}_Q - \mathbf{L})}{|\mathbf{r} - \mathbf{r}'|} \quad (1)$$

with local auxiliary functions η_Q centered on atomic positions $\mathbf{R}_Q + \mathbf{L}$ in direct lattice cells \mathbf{L} . A prerequisite for a well-defined \mathbf{J} matrix is a charge neutral auxiliary basis $\boldsymbol{\eta}$. We are aware of three approaches that directly construct charge neutral auxiliary functions based on local basis functions. Approach 1 mixes

atomic basis functions with nuclear delta functions of opposite charge.^{93–96} Approach 2 forms charge neutral linear combinations of charged GTF.⁹¹ Approach 3 employs a dual basis of charge neutral GTF and Poisson functions, however, truncates all charged s-type GTF.^{97,98} An indirect approach was introduced by Varga.⁹⁹

In this work, we develop a molecular and solid state implementation of RI-RPA employing GTF orbital and auxiliary basis sets using approach 2. Section 2.1 elaborates the RPA expressions introducing the Hartree kernel and KS polarization propagator in supermatrix representation. In section 2.2, the Hartree kernel is adapted to the translation symmetry of the crystal lattice. Next, the 4-index Hartree kernel is factorized into 3-index quantities employing RI in section 2.3. We generalize the periodic fast multipole method¹⁰⁰ to nonzero wave vectors in order to achieve accurate and efficient evaluation of Coulomb lattice sums, eq 1, and arrive at the final RI-RPA correlation energy in section 2.4. In the remaining sections, we provide details of the preliminary implementation, link our developments to other recent RPA methods, and discuss our results.

2. THEORY

2.1. Random Phase Approximation (RPA). We begin with a review of the basic definitions for RPA in two common representations, as this makes our work accessible to a broader readership. In the adiabatic connection formalism, the exact total nonrelativistic energy of the electronic ground state may be written as⁷

$$E = \langle \Phi_0 | \hat{H} | \Phi_0 \rangle + E^C \quad (2)$$

with the nonrelativistic physical Hamiltonian \hat{H} of the interacting many electron system, the ground state determinant Φ_0 built from the canonical KS orbitals, and the correlation energy E^C . We call the term $\langle \Phi_0 | \hat{H} | \Phi_0 \rangle$ briefly Hartree–Fock (HF) energy, E^{HF} . With the use of the zero-temperature fluctuation–dissipation theorem and the RPA,³¹ the following expression for the correlation energy is found,³⁰

$$E^{\text{CRPA}} = \frac{1}{2} \int_{-\infty}^{\infty} \frac{du}{2\pi} \text{Tr} \{ \ln [1 - v\chi_0(iu)] + v\chi_0(iu) \} \quad (3)$$

where

$$v(\mathbf{r}, \mathbf{r}') = 1/|\mathbf{r} - \mathbf{r}'| \quad (4)$$

represents the Coulomb operator and

$$\chi_0(\mathbf{r}, \mathbf{r}', iu) = \sum_{PQ} \sum_{\sigma} (f_{P\sigma} - f_{Q\sigma}) \times \frac{\varphi_{P\sigma}^*(\mathbf{r}) \varphi_{Q\sigma}(\mathbf{r}) \varphi_{Q\sigma}^*(\mathbf{r}') \varphi_{P\sigma}(\mathbf{r}')}{iu - (\varepsilon_{Q\sigma} - \varepsilon_{P\sigma})} \quad (5)$$

is the noninteracting or KS density–density response function at imaginary frequency iu with a real-valued frequency variable u .^{30,101} The asterisk (*) stands for complex conjugation. The occupation numbers $f_{p\sigma}$ of unrestricted spatial KS orbitals $\varphi_{p\sigma}$ at zero temperature are either zero or one for virtual and occupied orbitals, respectively. In this work, spins are denoted by indices σ, τ, \dots , orbitals have general indices P, Q, \dots , occupied orbitals have indices $\mathcal{I}, \mathcal{J}, \dots$, and virtual orbitals have indices $\mathcal{A}, \mathcal{B}, \dots$. The notation in eq 3 assumes a

matrix form for v and χ_0 , where the spatial arguments, \mathbf{r} and \mathbf{r}' , represent the matrix indices, e.g.,

$$\text{Tr}\{v\chi_0(iu)\} = \iint d^3r d^3r' v(\mathbf{r}, \mathbf{r}') \chi_0(\mathbf{r}', \mathbf{r}, iu) \quad (6)$$

Analogously, the logarithm in the integrand of eq 3 is expanded as a Taylor series of an additional perturbation parameter λ at $\lambda = 0$,

$$\text{Tr}\{\ln(1 - \lambda v\chi_0)\} = - \sum_{n=1}^{\infty} \frac{1}{n} \text{Tr}\{(v\chi_0)^n\} \lambda^n \quad (7)$$

with

$$\text{Tr}\{(v\chi_0)^n\} = \int \dots \int d^3r_1 \dots d^3r_{2n} v(\mathbf{r}_1, \mathbf{r}_2) \dots \chi_0(\mathbf{r}_{2n}, \mathbf{r}_1) \quad (8)$$

where iu is suppressed. This series is used with $\lambda = 1$ in eq 3, where linear terms cancel. Next, the space representation of the KS response function χ_0 , eq 5, is changed to the representation of occupied and virtual orbitals for the zero temperature case,

$$\begin{aligned} \chi_0(\mathbf{r}, \mathbf{r}', iu) = & - \sum_{I\mathcal{A}\sigma} \frac{\varphi_{I\sigma}^*(\mathbf{r}) \varphi_{\mathcal{A}\sigma}(\mathbf{r}) \varphi_{\mathcal{A}\sigma}^*(\mathbf{r}') \varphi_{I\sigma}(\mathbf{r}')}{\varepsilon_{\mathcal{A}\sigma} - \varepsilon_{I\sigma} - iu} \\ & - \sum_{I\mathcal{A}\sigma} \frac{\varphi_{\mathcal{A}\sigma}^*(\mathbf{r}) \varphi_{I\sigma}(\mathbf{r}) \varphi_{I\sigma}^*(\mathbf{r}') \varphi_{\mathcal{A}\sigma}(\mathbf{r}')}{\varepsilon_{\mathcal{A}\sigma} - \varepsilon_{I\sigma} + iu} \end{aligned} \quad (9)$$

Defining spatial orbital products

$$\Omega_{I\mathcal{A}\sigma}(\mathbf{r}) = \varphi_{I\sigma}^*(\mathbf{r}) \varphi_{\mathcal{A}\sigma}(\mathbf{r}) \quad (10)$$

and column vector \mathbf{b} formed by all products $\Omega_{I\mathcal{A}\sigma}^*$ and $\Omega_{I\mathcal{A}\sigma}$,

$$\mathbf{b}^T(\mathbf{r}) = (\dots, \Omega_{I\mathcal{A}\sigma}^*(\mathbf{r}), \dots, \Omega_{I\mathcal{A}\sigma}(\mathbf{r}), \dots) \quad (11)$$

eq 9 is represented by

$$\chi_0(\mathbf{r}, \mathbf{r}', iu) = \mathbf{b}^\dagger(\mathbf{r}) \mathbf{\Pi}_0(iu) \mathbf{b}(\mathbf{r}') \quad (12)$$

where the superscript \dagger denotes the adjoint operator and the matrix

$$\mathbf{\Pi}_0(iu) = \begin{pmatrix} \boldsymbol{\pi}^-(iu) & \mathbf{0} \\ \mathbf{0} & \boldsymbol{\pi}^+(iu) \end{pmatrix} \quad (13)$$

represents the KS polarization propagator in canonical orbitals with the submatrices^{24,64}

$$\boldsymbol{\pi}^\pm(iu) = -(\boldsymbol{\Delta} \pm iu\mathbf{1})^{-1} \quad (14)$$

containing matrix elements

$$\Delta_{I\mathcal{A}\sigma, \mathcal{J}\mathcal{B}\tau} = \delta_{I\mathcal{J}} \delta_{\mathcal{A}\mathcal{B}} \delta_{\sigma\tau} (\varepsilon_{\mathcal{A}\sigma} - \varepsilon_{I\sigma}) \quad (15)$$

Equation 12 is then inserted into eq 8,

$$\text{Tr}\{(v\chi_0)^n\} = \int \dots \int d^3r_1 \dots d^3r_{2n} v(\mathbf{r}_1, \mathbf{r}_2) \dots \mathbf{b}^\dagger(\mathbf{r}_{2n}) \mathbf{\Pi}_0 \mathbf{b}(\mathbf{r}_1) \quad (16)$$

Note that this integral is a scalar number c and that $c = \text{Tr}\{c\}$. Using the invariance of the trace of a matrix product under cyclic permutation and defining the Hartree kernel matrix

$$\mathbf{V} = \iint d^3r_1 d^3r_2 \mathbf{b}(\mathbf{r}_1) v(\mathbf{r}_1, \mathbf{r}_2) \mathbf{b}^\dagger(\mathbf{r}_2) \quad (17)$$

the integral from eq 16 becomes

$$\text{Tr}\{(v\chi_0(iu))^n\} = \text{Tr}\{(\mathbf{V}\mathbf{\Pi}_0(iu))^n\} \quad (18)$$

This finally means that eq 3 may be written in a supermatrix formalism,

$$E^{\text{CRPA}} = \frac{1}{2} \int_{-\infty}^{\infty} \frac{du}{2\pi} \text{Tr}\{\ln[\mathbf{1} - \mathbf{V}\mathbf{\Pi}_0(iu)] + \mathbf{V}\mathbf{\Pi}_0(iu)\} \quad (19)$$

We should mention that the Taylor series expansion used in this derivation may not converge. As an alternative there is a rigorous proof that the trace of the logarithm of $\mathbf{1} - \mathbf{V}\mathbf{\Pi}_0$ is invariant with cyclic permutation within the matrix product $\mathbf{V}\mathbf{\Pi}_0$. This proof is conducted using

$$\text{Tr}[\ln(\mathbf{1} - \mathbf{V}\mathbf{\Pi}_0)] = \ln[\text{Det}(\mathbf{1} - \mathbf{V}\mathbf{\Pi}_0)] \quad (20)$$

and Sylvester's determinant identity,¹⁰²

$$\text{Det}(\mathbf{1} - \mathbf{b}\mathbf{v}\mathbf{b}^\dagger\mathbf{\Pi}_0) = \text{Det}(\mathbf{1} - \mathbf{v}\mathbf{b}^\dagger\mathbf{\Pi}_0\mathbf{b}) \quad (21)$$

The same argument applies to the Taylor series used in Appendix C.

Published work evaluates RPA correlation energies in the space representation, eq 3,³⁰ reciprocal space representation,^{41,49} or using particle-hole representations.^{23,28} Superoperators and their supermatrix representations have a long tradition in propagator theory.^{24,103} The supermatrix formalism in terms of orbitals was also presented for related approaches, for example, for the RPA-renormalized many-body perturbation theory⁶⁴ and the GW method.¹⁰⁴

2.2. Translation Symmetry in the Hartree Kernel. The Hartree kernel \mathbf{V} is defined by eqs 17, 11, and 10 yielding the form

$$\mathbf{V} = \begin{pmatrix} \mathbf{V}_{11} & \mathbf{V}_{12} \\ \mathbf{V}_{12}^* & \mathbf{V}_{11}^* \end{pmatrix} \quad (22)$$

The elements of submatrices in \mathbf{V} are electron repulsion integrals (ERI), in Mulliken notation,

$$\begin{aligned} V_{11, I\mathcal{A}\sigma, \mathcal{J}\mathcal{B}\tau} &= (\mathcal{A}I\sigma | \mathcal{J}\mathcal{B}\tau) \quad \text{and} \\ V_{12, I\mathcal{A}\sigma, \mathcal{J}\mathcal{B}\tau} &= (\mathcal{A}I\sigma | \mathcal{B}\mathcal{J}\tau) \end{aligned} \quad (23)$$

The formalism presented above is valid for any molecule or crystal. Explicit use of translation symmetry in crystals is achieved by turning the general orbital quantum number \mathcal{P} into a combination of band index p and wave vector \mathbf{k} ,

$$\mathcal{P} \equiv (p, \mathbf{k}) \quad (24)$$

This pair of quantum numbers appears in the normalized KS orbitals in Bloch's form,¹⁰⁵

$$\varphi_{p\mathbf{k}\sigma}(\mathbf{r}) = \frac{1}{\sqrt{N_{\text{UC}}}} \tilde{\varphi}_{p\mathbf{k}\sigma}(\mathbf{r}) \quad (25)$$

with unnormalized Bloch functions¹⁰⁶

$$\tilde{\varphi}_{p\mathbf{k}\sigma}(\mathbf{r}) = \sum_{\mathbf{L}} e^{i\mathbf{k}\cdot\mathbf{L}} \varphi_{p\mathbf{k}\sigma}^{\mathbf{L}}(\mathbf{r}) \quad (26)$$

where summation of direct lattice translation vectors \mathbf{L} is carried out over all N_{UC} unit cells of the crystal. The cell functions

$$\varphi_{p\mathbf{k}\sigma}^{\mathbf{L}}(\mathbf{r}) = \sum_{\mu} C_{\mu p\mathbf{k}\sigma} \xi_{\mu}^{\mathbf{L}}(\mathbf{r}) \quad (27)$$

are expanded in N real-valued GTF $\xi_{\mu}^{\mathbf{L}} \equiv \xi_{\mu}(\mathbf{r} - \mathbf{R}_{\mu} - \mathbf{L})$ centered at atomic positions \mathbf{R}_{μ} in a single cell \mathbf{L} . Translation symmetry

in the Hartree kernel elements, eq 23, is explored using the Bloch orbitals,

$$(\mathcal{A}I\sigma|\mathcal{J}B\tau) = \frac{1}{N_{UC}^2} \sum_{L_1 L_2 L_3 L_4} e^{i(-k_a \cdot L_1 + k_i \cdot L_2 - k_j \cdot L_3 + k_b \cdot L_4)} \times (\phi_{a k_a \sigma}^{L_1*} \phi_{i k_i \sigma}^{L_2} |\phi_{j k_j \tau}^{L_3*} \phi_{b k_b \tau}^{L_4}), \quad (28)$$

where ERI of cell functions are invariant under translation, that is,

$$(\phi_{a k_a \sigma}^{L_1*} \phi_{i k_i \sigma}^{L_2} |\phi_{j k_j \tau}^{L_3*} \phi_{b k_b \tau}^{L_4}) = (\phi_{a k_a \sigma}^{0*} \phi_{i k_i \sigma}^{L_2-L_1} |\phi_{j k_j \tau}^{L_3-L_1*} \phi_{b k_b \tau}^{L_4-L_1}) \quad (29)$$

In contrast to Mulliken notation, which implies complex conjugation for indices I, \mathcal{A} and J, \mathcal{B} , we show explicitly complex conjugation in ERI, if symbols of orbitals and basis functions such as $\tilde{\varphi}$ and ϕ are used. The expression in eq 28 is rearranged to¹⁰⁷

$$(\mathcal{A}I\sigma|\mathcal{J}B\tau) = \delta_{0, -k_a + k_i - k_j + k_b} \frac{1}{N_{UC}} (\phi_{a k_a \sigma}^{0*} \tilde{\varphi}_{i k_i \sigma} | \tilde{\varphi}_{j k_j \tau}^* \tilde{\varphi}_{b k_b \tau}), \quad (30)$$

using eq 29 and the identity¹⁰⁸

$$\frac{1}{N_{UC}} \sum_{\mathbf{L}} e^{i\mathbf{k} \cdot \mathbf{L}} = \delta_{\mathbf{k}\mathbf{K}} \quad (31)$$

where \mathbf{K} is a lattice vector of reciprocal space. In the present work, wave vectors are always mapped into the first Brillouin zone (FBZ) so that only $\mathbf{K} = \mathbf{0}$ is employed. Introducing exciton vectors,

$$\mathbf{q} = \mathbf{k}_a - \mathbf{k}_i \quad \text{and} \quad \mathbf{q}' = \mathbf{k}_b - \mathbf{k}_j \quad (32)$$

the Hartree kernel \mathbf{V} is reduced to integrals assigned to a single reference unit cell $\mathbf{L} = \mathbf{0}$ and is represented in terms of exciton vector blocks $\mathbf{V}_{11}(\mathbf{q}, \mathbf{q}')$ and $\mathbf{V}_{12}(\mathbf{q}, \mathbf{q}')$ with elements

$$\begin{aligned} V_{11, I\mathcal{A}\sigma J\mathcal{B}\tau}(\mathbf{q}, \mathbf{q}') &= (\mathcal{A}I\sigma|\mathcal{J}B\tau) \\ &= \delta_{0, -\mathbf{q}+\mathbf{q}'} \frac{1}{N_{UC}} (\phi_{a k_a + \mathbf{q}\sigma}^{0*} \tilde{\varphi}_{i k_i \sigma} | \tilde{\varphi}_{j k_j \tau}^* \tilde{\varphi}_{b k_b + \mathbf{q}'\tau}) \end{aligned} \quad (33)$$

$$\begin{aligned} V_{12, I\mathcal{A}\sigma J\mathcal{B}\tau}(\mathbf{q}, \mathbf{q}') &= (\mathcal{A}I\sigma|\mathcal{B}J\tau) \\ &= \delta_{0, -\mathbf{q}-\mathbf{q}'} \frac{1}{N_{UC}} (\phi_{a k_a + \mathbf{q}\sigma}^{0*} \tilde{\varphi}_{i k_i \sigma} | \tilde{\varphi}_{j k_j \tau}^* \tilde{\varphi}_{b k_b + \mathbf{q}'\tau}) \end{aligned} \quad (34)$$

Since for any nonzero \mathbf{q} there is a corresponding $-\mathbf{q}$ in the FBZ, the \mathbf{q} -blocks in \mathbf{V} are arranged symmetrically around $\mathbf{q} = \mathbf{0}$ leading to block diagonal and block antidiagonal submatrices \mathbf{V}_{11} and \mathbf{V}_{12} , see Figure 1.

The Hartree kernel matrix is the Hartree contribution to the orbital rotation Hessian matrices, usually called \mathbf{A} and \mathbf{B} in the literature,¹⁰¹ used in the eigenvalue problem of time-dependent DFT (TDDFT).¹⁰⁹ For periodic polymers, the Hartree kernel in terms of occupied and virtual orbitals was already presented by ref 110. In contrast to our result, which contains a sign switch between \mathbf{q} and \mathbf{q}' in \mathbf{V}_{12} for nonvanishing elements, the corresponding contribution in the orbital rotation Hessian \mathbf{B} seems to be missing in eq 32 of ref 110. This sign switch is not relevant for the numerical results of ref 110 because single particle excitations were restricted to direct transitions ($\mathbf{q} = \mathbf{q}' = \mathbf{0}$) in order to neglect vibronic effects in TDDFT calculations. For the RPA correlation energy, however, the sign is important as all exciton vectors must be included.

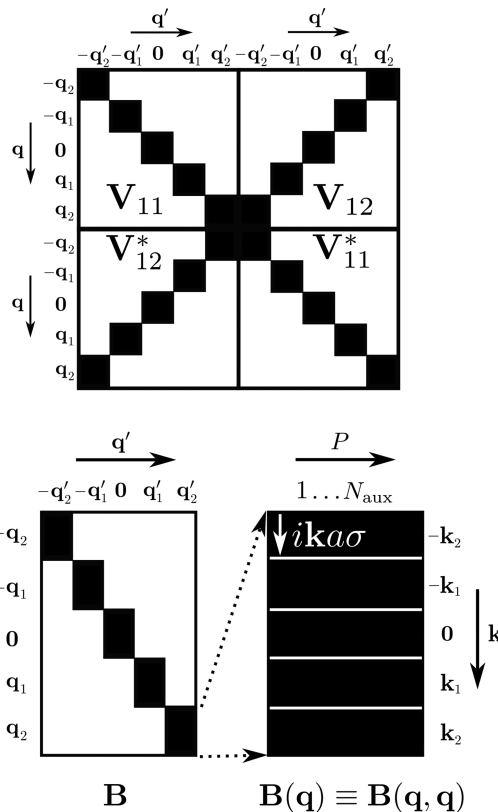


Figure 1. Structures of the Hartree kernel matrix \mathbf{V} (top) and the \mathbf{B} matrix (bottom). Black rectangles represent nonzero blocks $\mathbf{V}_{11}(\mathbf{q}, \mathbf{q}')$, $\mathbf{V}_{12}(\mathbf{q}, -\mathbf{q}')$, and $\mathbf{B}(\mathbf{q}, \mathbf{q}')$. White area represents zero blocks.

2.3. Density Fitting for Bloch Functions. The RI method can be used to factorize the 4-index integrals, eqs 33 and 34, into 3-index integrals reducing the effort to evaluate Hartree kernel-dependent quantities. Our derivation follows a strategy which is called density fitting. The densities to be fitted are the Bloch orbital products $\Omega_{\mathcal{J}B\tau}$ between orthogonal occupied and virtual states, cf. eq 10, appearing in the Hartree kernel elements, eq 23. These products represent Bloch functions of exciton vectors \mathbf{q}' and are charge neutral densities,

$$\int d^3r \Omega_{\mathcal{J}B\tau}(\mathbf{r}) = 0 \quad (35)$$

Therefore, it is sufficient to fit each Bloch orbital product

$$\Omega_{\mathcal{J}B\tau}(\mathbf{r}) \approx \tilde{\Omega}_{\mathcal{J}B\tau}(\mathbf{r}) = \sum_P d_P^{\mathcal{J}B\tau} \eta_{P\mathbf{q}'}(\mathbf{r}) \quad (36)$$

by a linear combination of charge neutral auxiliary Bloch basis functions of the corresponding exciton vector,

$$\eta_{P\mathbf{q}'}(\mathbf{r}) = \frac{1}{N_{UC}} \sum_{\mathbf{L}} e^{i\mathbf{q}' \cdot \mathbf{L}} \eta_P^{\mathbf{L}}(\mathbf{r}) \quad (37)$$

If $\mathbf{q}' \neq \mathbf{0}$ within the FBZ, then the Bloch function is charge neutral for any of the N_{aux} atom-centered auxiliary GTF η_P . For $\mathbf{q}' = \mathbf{0}$, the Bloch function carries charge when function η_P has a net charge as explained in Appendix A. The two cases, zero and nonzero exciton vectors, must be treated differently in order to obtain correct results for the Coulomb lattice sums.

The discussion on evaluation of Coulomb lattice sums is left within [Appendix A](#).

Next, the fitting coefficients $d_p^{\mathcal{J}B\tau}$ are determined from minimization of the real-valued Coulomb-norm of the residual Bloch functions,

$$D = (\Omega_{\mathcal{J}B\tau}^* - \tilde{\Omega}_{\mathcal{J}B\tau}^* \Omega_{\mathcal{J}B\tau} - \tilde{\Omega}_{\mathcal{J}B\tau}) \quad (38)$$

The norm may be reduced to a single reference cell similar to [eq 30](#),

$$\begin{aligned} N_{\text{UC}} D &= (\phi_{b_{\mathbf{k}+\mathbf{q}'\tau}^0}^* \tilde{\varphi}_{j_{\mathbf{k}\tau}} | \tilde{\varphi}_{j_{\mathbf{k}\tau}}^* \tilde{\varphi}_{b_{\mathbf{k}+\mathbf{q}'\tau}} \\ &- \sum_P (d_P^{\mathcal{J}B\tau})^* (\tilde{\eta}_{P\mathbf{q}}^* | \tilde{\varphi}_{j_{\mathbf{k}\tau}}^* \phi_{b_{\mathbf{k}+\mathbf{q}'\tau}^0} \\ &- \sum_Q d_Q^{\mathcal{J}B\tau} (\phi_{b_{\mathbf{k}+\mathbf{q}'\tau}^0} | \tilde{\varphi}_{j_{\mathbf{k}\tau}} \tilde{\eta}_{Q\mathbf{q}'}) \\ &+ \sum_{PQ} (d_P^{\mathcal{J}B\tau})^* d_Q^{\mathcal{J}B\tau} (\eta_P^0 | \tilde{\eta}_{Q\mathbf{q}'})) \end{aligned} \quad (39)$$

where functions $\tilde{\eta}_{P\mathbf{q}'}$ are defined by [eq 37](#), however, without the $1/N_{\text{UC}}$ normalization prefactor. The stationary condition

$$\frac{dD}{dd_P^{\mathcal{J}B\tau}} = 0 \Leftrightarrow \frac{dD}{d(d_P^{\mathcal{J}B\tau})^*} = 0 \quad (40)$$

yields the $\mathbf{d}^{\mathcal{J}B\tau}$ vector of optimal fitting coefficients,

$$\mathbf{J}(\mathbf{q}') \mathbf{d}^{\mathcal{J}B\tau} = \boldsymbol{\gamma}^{\mathcal{J}B\tau} \quad (41)$$

with \mathbf{J} matrix and $\boldsymbol{\gamma}$ vector elements

$$J_{PQ}(\mathbf{q}') = (\eta_P^0 | \tilde{\eta}_{Q\mathbf{q}'}) \quad (42)$$

$$\gamma_P^{\mathcal{J}B\tau} = (\tilde{\eta}_{P\mathbf{q}'}^* | \tilde{\varphi}_{j_{\mathbf{k}\tau}}^* \phi_{b_{\mathbf{k}+\mathbf{q}'\tau}^0}) \quad (43)$$

$\mathbf{J}(\mathbf{q})$ is positive definite and Hermitian and can thus be decomposed by Cholesky factorization

$$\mathbf{J}(\mathbf{q}) = \mathbf{\Lambda}^\dagger(\mathbf{q}) \mathbf{\Lambda}(\mathbf{q}) \quad (44)$$

into a matrix product containing the upper triangular matrix $\mathbf{\Lambda}$, for which

$$\mathbf{\Lambda}(-\mathbf{q}) = \mathbf{\Lambda}^*(\mathbf{q}) \quad (45)$$

The factorization of \mathbf{J} is used to solve [eq 41](#) for the fitting coefficients from [eq 36](#),

$$\mathbf{d}^{\mathcal{J}B\tau} = \mathbf{\Lambda}^{-1}(\mathbf{q}') (\mathbf{\Lambda}^{-1}(\mathbf{q}'))^\dagger \boldsymbol{\gamma}^{\mathcal{J}B\tau} \quad (46)$$

It is shown in [Appendix B](#) that this solution to the RI-approximation yields

$$V_{11, I\mathcal{A}\sigma\mathcal{J}B\tau}^{\text{RI}}(\mathbf{q}, \mathbf{q}') = \frac{1}{N_{\text{UC}}} \sum_P B_{ika\sigma P}(\mathbf{q}) \delta_{\mathbf{q}\mathbf{q}'} B_{jk'\tau P}(\mathbf{q}') \quad (47)$$

with matrix elements

$$B_{ika\sigma P}(\mathbf{q}) = (\phi_{a_{\mathbf{k}+\mathbf{q}\sigma}^0} | \tilde{\varphi}_{i_{\mathbf{k}\sigma}} | \sum_Q (\mathbf{\Lambda}^{-1}(\mathbf{q}))_{QP} \tilde{\eta}_{Q\mathbf{q}}) \quad (48)$$

The exciton vector blocks $\mathbf{B}(\mathbf{q}) \equiv \mathbf{B}(\mathbf{q}, \mathbf{q})$ form the \mathbf{q} -block diagonal \mathbf{B} matrix, [Figure 1](#). Each \mathbf{q} -block is a rectangular matrix, where the first dimension runs over all combinations of $ika\sigma$ and the second dimension runs over all P . In [Appendix B](#), the outcome presented above is derived for all submatrices of

the Hartree kernel, [eq 22](#), leading to the entire translation-symmetry adapted and RI-approximated Hartree kernel,

$$\mathbf{V} \approx \mathbf{V}^{\text{RI}} = \frac{1}{N_{\text{UC}}} \mathbf{B} \mathbf{B}^\dagger \quad (49)$$

where \mathbf{B} is defined as

$$\mathbf{B} = \begin{pmatrix} \mathbf{B} \\ \mathbf{B}^* \bar{\mathbf{I}} \end{pmatrix} \quad (50)$$

For N_k wave vectors in the FBZ, the $\bar{\mathbf{I}}$ matrix is a \mathbf{q} -block antidiagonal matrix of order $N_k \times N_{\text{aux}}$ containing unit submatrices \mathbf{I}_{aux} of order N_{aux}

$$\bar{\mathbf{I}} = \begin{pmatrix} \mathbf{0} & \dots & \mathbf{I}_{\text{aux}} \\ \vdots & \ddots & \vdots \\ \mathbf{I}_{\text{aux}} & \dots & \mathbf{0} \end{pmatrix} \quad (51)$$

2.4. RPA Correlation Energy Per Unit Cell. The RI Hartree kernel factorized in terms of \mathbf{B} leads to the RI-RPA correlation energy per unit cell, see [Appendix C](#),

$$\begin{aligned} E_{\text{UC}}^{\text{CRIRPA}} &= \frac{1}{2} \int_{-\infty}^{\infty} \frac{du}{2\pi} \frac{1}{N_k} \sum_{\mathbf{q}} \text{Tr} \{ \ln(\mathbf{I}_{\text{aux}} + \mathbf{Q}(u, \mathbf{q})) \\ &- \mathbf{Q}(u, \mathbf{q}) \} \end{aligned} \quad (52)$$

with the complex square matrix

$$\mathbf{Q}(u, \mathbf{q}) = \frac{2}{N_k} \mathbf{B}^\dagger(\mathbf{q}) \mathbf{G}(u, \mathbf{q}) \mathbf{B}(\mathbf{q}) \quad (53)$$

of order N_{aux} for which

$$\mathbf{Q}(u, -\mathbf{q}) = \mathbf{Q}^*(u, \mathbf{q}) \quad (54)$$

As the diagonal matrix

$$\mathbf{G}(u, \mathbf{q}) = \mathbf{\Delta}(\mathbf{q}) [\mathbf{\Delta}^2(\mathbf{q}) + u^2 \mathbf{1}]^{-1} \quad (55)$$

with $\mathbf{\Delta}$ from [eq 15](#) is real, the \mathbf{Q} matrix is Hermitian, and the trace in [eq 52](#) is thus real. In [Appendix C](#), the derivation of [eq 52](#) converts sums over discrete wave vectors to integrals,

$$\sum_{\mathbf{k}}^{\text{FBZ}} \rightarrow \frac{N_{\text{UC}}}{V_k} \int_{\text{FBZ}} d^3k \quad (56)$$

with volume V_k of the first FBZ. Subsequently, the integrals are approximated by numerical integration on a finite equispaced grid within the FBZ,

$$\int_{\text{FBZ}} d^3k \rightarrow \frac{V_k}{N_k} \sum_{\mathbf{k}} \quad (57)$$

where N_k is the total number of wave vectors on the grid.

3. IMPLEMENTATION

All equations in the present work are valid for molecules and crystals. If only the $\mathbf{0}$ contributions are left from all summations over direct lattice vectors \mathbf{L} and wave vectors \mathbf{k} and \mathbf{q} , and if the total number of unit cells and wave vectors is $N_{\text{UC}} = N_k = 1$, then the expression of the molecular RI-RPA energy published in [ref 73](#) is recovered.

The algorithm to evaluate \mathbf{B} is schematically shown in [Figure 2](#). Lattice sums in the 2- and 3-index ERI of \mathbf{J} and \mathbf{B} , [eqs 42](#) and [48](#), are evaluated as explained in [Appendix A](#). In short, the crystal near field (CNF) part is evaluated by direct integration.

- a) **Local moments of CFF** (cf. appendix A)
- Compute multipole moments $M[\eta_p^0]$
 - If Γ : charge projection, $M[\eta_p^0] \times P_{\perp PQ}$
 - Compute local moments $L[\tilde{\eta}_{PQ}^{CFF}]$
- b) **B(q) matrix, CFF contribution**
- Loop \mathbf{k} & blocks of occ. orb. i & prescreened shellpairs $\xi_\mu^0 \xi_\nu^L$:
 - Compute multipole moments $M[\xi_\mu^0 \xi_\nu^L]$
 - Loop \mathbf{q} :
 - Contract $M[\xi_\mu^0 \xi_\nu^L] \times L[\tilde{\eta}_{PQ}^{CFF}] \rightarrow (\xi_\nu^L \xi_\mu^0 | \tilde{\eta}_{PQ}^{CFF})$
 - Contract and accumulate half transformed integrals:

$$e^{i\mathbf{k}\cdot\mathbf{L}} \times (\xi_\nu^L \xi_\mu^0 | \tilde{\eta}_{PQ}^{CFF}) \times C_{\nu i\mathbf{k}} \rightarrow (\xi_\mu^0 \tilde{\varphi}_{i\mathbf{k}} | \tilde{\eta}_{PQ}^{CFF})$$
 - Write half-transform of current block to disk
- c) **B(q) matrix, CNF contribution**
- Loop \mathbf{k} & blocks of occ. orb. i :
 - Compute half-transform $(\xi_\mu^0 \tilde{\varphi}_{i\mathbf{k}} | \tilde{\eta}_{PQ}^{CNF})$ via direct integration of individual contributions $(\xi_\mu^0 \xi_\nu^L | \eta_p^0)$
 - Loop \mathbf{q} :
 - If Γ : charge projection, $(\xi_\mu^0 \tilde{\varphi}_{i\mathbf{k}} | \tilde{\eta}_{PQ}^{CNF}) \times P_{\perp PQ}$
 - Read CFF contribution of half-transform from disk & $(\xi_\mu^0 \tilde{\varphi}_{i\mathbf{k}} | \tilde{\eta}_{PQ}^{CFF}) + (\xi_\mu^0 \tilde{\varphi}_{i\mathbf{k}} | \tilde{\eta}_{PQ}^{CNF}) \rightarrow (\xi_\mu^0 \tilde{\varphi}_{i\mathbf{k}} | \tilde{\eta}_{PQ})$
 - Find \mathbf{k}' on grid within FBZ equivalent to $\mathbf{k} + \mathbf{q}$
 - $C_{\mu a\mathbf{k}'}^* \times (\xi_\mu^0 \tilde{\varphi}_{i\mathbf{k}} | \tilde{\eta}_{PQ}) \rightarrow (\phi_{a\mathbf{k}'}^* | \tilde{\varphi}_{i\mathbf{k}} | \tilde{\eta}_{PQ})$
 - $(\phi_{a\mathbf{k}'}^* | \tilde{\varphi}_{i\mathbf{k}} | \tilde{\eta}_{PQ}) \times \Lambda_{PQ}^{-1}(\mathbf{q}) \rightarrow B_{i\mathbf{k}aQ}(\mathbf{q})$
 - Write block of **B(q)** to disk

Figure 2. Algorithm for **B** matrix, eq 48. Einstein's sum convention is used. Spin and multipole indices are suppressed. Γ means $\mathbf{q} = \mathbf{0}$.

The long-range part of the lattice sums, the crystal far field (CFF), is calculated by multipole methods. The implementation can be readily used for systems of all periodic dimensions (0D to 3D) in the Γ -point approximation. The wave vector implementation is restricted to 1D and 2D systems, as the correction of quadrupole and second electric moments required for 3D systems is not yet available in our program. Strategies to implement such corrections were already published for SCF methods.¹¹¹ The subsequent evaluation of the correlation energy from the **Q** matrix is straightforward because the molecular and periodic implementations just differ by wave vector loops and complex valued matrix algebra employed in the latter case. The frequency integral is approximated by numerical integration over a finite grid of u . The optimal frequency points are determined for the Γ -point with the procedure outlined in ref 73 and are used for all wave vectors. The trace of the logarithm is computed efficiently by Cholesky factorization of the positive definite Hermitian matrix⁴²

$$1_{\text{aux}} + \mathbf{Q}(u, \mathbf{q}) = \mathbf{U}^\dagger(u, \mathbf{q}) \mathbf{U}(u, \mathbf{q}) \quad (58)$$

using the real diagonal elements of upper triangle **U**,

$$\text{Tr}[\ln(1 + \mathbf{Q}(u, \mathbf{q}))] = 2 \ln\left(\prod_p U_{pp}(u, \mathbf{q})\right) \quad (59)$$

Inversion symmetry of the Bravais lattice is used within the DFT¹¹² and RI-RPA implementations. The number of FLOP in the contraction of **B** with **G**, eq 53, increases as $O(N_{\text{aux}}^2 N_{\text{occ}} N_{\text{virt}} N_k)$ and represents the bottleneck of the calculation in large systems, where N_{occ} and N_{virt} denote the numbers of occupied and virtual orbitals, respectively. Referring to eq 52, this contraction is performed N_k times. The computational demand of the **B** matrix in GTF basis with increasing basis set size N grows as $O(N^3)$. This lowers to $O(N^2)$ in the asymptotic regime, as the GTF products are prescreened by an overlap criterion. The transformation of **B** into the canonical orbital basis scales as $O(N^4)$. The effort with increasing number of wave vectors grows as $O(N_k^2)$. While RI-RPA calculations within our prototype implementation can be currently conducted only on a single core, the underlying RI-DFT program may run in parallel threads on shared-memory machines using the OpenMP application programming interface.¹¹² Our RI-RPA program is implemented in a developer version of the Turbomole program suite.¹¹³

4. COMPARISON TO RELATED METHODS

At this point, it is instructive to compare our work with published similar approaches. Our work presents a quartic scaling

canonical Coulomb-metric RI-RPA method comparable to the molecular approach of Eshuis et al.,⁷³ which evaluates the **Q** matrix, eq 53, directly from matrices in orbital basis, eqs 48 and 55. The relationship between this and two recently published low-scaling RI-RPA approaches based on GTF from Schurkus et al.⁵⁸ and Wilhelm et al.⁵⁹ is ideally discussed in the Γ -point approximation. The latter schemes use the overlap-metric RI approximation for molecules⁵⁸ and Γ -point⁵⁹

$$\mathbf{B} = \mathbf{S}^{(3)} \mathbf{T} \quad (60)$$

instead of eq 48. The overlap RI is one of the RI variants already discussed in ref 88. **B** is defined using the 3-index overlap

$$S_{i\sigma p}^{(3)} = \sum_{\mathbf{L}\mathbf{L}'} \int d^3r \phi_{i\sigma}^0(\mathbf{r}) \phi_{a\sigma}^{\mathbf{L}}(\mathbf{r}) \eta_p^{\mathbf{L}'}(\mathbf{r}) \quad (61)$$

and the lower triangular matrix **T** from Cholesky factorization of matrix $\mathbf{S}^{-1} \mathbf{J} \mathbf{S}^{-1}$ with **J** from eq 42 and 2-index overlap matrix

$$S_{PQ} = \sum_{\mathbf{L}} \int d^3r \eta_p^{\mathbf{L}}(\mathbf{r}) \eta_Q^{\mathbf{L}}(\mathbf{r}) \quad (62)$$

This definition of **B** is used throughout this section and can be used to define the overlap RI Hartree kernel via **B** with eq 49 leading to expressions for **Q** matrix and correlation energy that are formally identical to eqs 53 and 52. The evaluation of this overlap RI-RPA energy expression still scales as $O(N^4)$.

The scaling of RI-RPA calculations in the GTF representation was further reduced by a combination of the overlap-metric approach with the “double Laplace transform”,

$$(\Delta^2 + u^2 \mathbf{1})^{-1} = \int_0^\infty d\tau \frac{\sin(u\tau)}{u} e^{-\tau\Delta} \quad (63)$$

where imaginary time τ is introduced.⁵⁸ A reduced scaling is achieved by inserting the **G** matrix, eq 55, represented by this transform into the **Q** matrix of eq 53 together with GTF expansions of real Γ -orbitals, cf. eqs 26 and 27, which appear in the $S_{i\sigma p}^{(3)}$ elements. This allows the representation of the **Q** matrix in the imaginary frequency domain,

$$\mathbf{Q}(u) = \int_0^\infty d\tau \frac{\sin(u\tau)}{u} \mathbf{Q}(\tau) \quad (64)$$

as a transform of **Q** in the imaginary time domain,

$$\mathbf{Q}(\tau) = \mathbf{T}^\dagger \tilde{\mathbf{P}}(\tau) \mathbf{T} \quad (65)$$

where

$$\tilde{P}_{PQ}(\tau) = -2 \sum_{\sigma} \sum_{\mu\kappa\lambda} S_{\mu\nu P}^{(3)} \frac{d}{d\tau} [D_{\mu\kappa\sigma}^{\text{occ}}(\tau) D_{\nu\lambda\sigma}^{\text{virt}}(\tau)] S_{\kappa\lambda Q}^{(3)} \quad (66)$$

contains the pseudodensity matrices^{114,115} as defined in refs 58 and 59. Equation 64 of the present work represents eq 11 in ref 58 and integration by parts with respect to τ leads to the “INT” form of ref 58. This integrated double Laplace transform is equivalent with the cosine transformation in eq 23 of ref 59, which was used earlier in the PAW method.⁵⁵ The sparsity of the 3-index overlap in eq 66 leads to cubic scaling implementations of RPA.⁵⁹ Wilhelm et al. showed that the deviation in absolute correlation energies between overlap and Coulomb RI-RPA is in the range of 70 μ hartree for 32 water molecules in a periodic box. In addition, Schurkus and co-workers made use of sparse pseudodensity matrices leading to a linear scaling algorithm for matrix \tilde{P} .⁵⁸

The evaluation of the Coulomb-metric matrix J , eq 42, appearing in Coulomb RI- and overlap RI-RPA is challenging for periodic systems because it contains long-range lattice summations, which diverge for matrix elements between charged s -type GTF. Wilhelm et al. and our work present two different schemes to circumvent this difficulty.

The Γ -point implementation of Wilhelm et al. employs formally a plane wave auxiliary basis. In contrast to the conventional Gaussians and plane waves approach (GPW) in the preceding work,⁴² the approach of Wilhelm et al. is grid-free, represents J in a Hermite Gaussian basis, J_{H_i, H_j} , and uses an analytical expansion of the plane wave electrostatic potential in terms of a secondary auxiliary Gaussian-type basis. As result, the number of terms evaluated for each matrix element J_{H_i, H_j} depends on the number of reciprocal lattice vectors up to a cutoff and the number of secondary auxiliary GTF. As this approach is based on the GPW approach, the Γ -point matrix of J must be calculated on the reciprocal lattice and only 3D-periodic calculations can be conducted.

Our approach evaluates J directly in the representation of charge projected auxiliary GTF η . See Appendix A for an explanation and citations of charge projected GTF and the following multipole methods. The number of terms evaluated for a single matrix element, J_{PQ} , depends on the number of calculated ERI in the crystal near field and the number of multipole moments for the crystal far field expansion, which is of $O(l_{\text{max}}^2)$ with maximum multipole order l_{max} . In the crystal near field, the ERI ($\eta_p^0 \eta_Q^L$) are collectively calculated for all η_Q^L in the local far field of η_p^0 with an atom-centered multipole method. l_{max} of the atom-centered multipole expansion is the l -moment of the GTF η_p^0 , which is much smaller than l_{max} used for the crystal far field. In this way, the number of directly evaluated ERI and the computational demand are further reduced. On the Γ -point, evaluation of J is possible for 0D to 3D-periodic systems.

In terms of general applicability, all approaches discussed above do not yet serve as practical schemes to compute RPA correlation energies of metals for mainly two reasons. First, all these approaches rely on integer occupation numbers, dividing orbitals into occupied (hole) and virtual (particle) states. This assumption was made in the transition from eq 5 to eq 9. On the contrary, metals are typically treated by use of fractional occupations which do not allow the definition of a single set of holes and particles. In the moment, we are not aware of any

practical RPA implementation in the particle–hole scheme, eq 19, employing fractional occupations. Second, diffuse GTF with exponents close to or below 0.1 au in the orbital expansion may be required to describe the quasi-free electrons in a metal. This leads to nearly linear dependencies between Bloch basis functions, which may yield, for example, convergence problems in the underlying SCF-DFT calculations. GTF basis sets optimized for solids may help in this situation.^{116,117}

If the orbital basis is expanded in plane waves, the Coulomb operator and the response function are represented in reciprocal lattice vectors \mathbf{K} . The response function is then evaluated similarly to the direct space representation in eq 5, that is, all orbital contributions are contracted with orbital occupations into elements $\chi_{0, \mathbf{K}\mathbf{K}'}(\mathbf{q}, i\omega)$.⁴⁰ This representation is convenient for metals, as a distinction into holes and particles is not necessary.⁴¹ In addition, a cubic scaling RPA method was reported⁵⁵ and the orthogonal plane wave basis also prevents linear dependencies. Major drawbacks may appear in terms of efficiency for less dense and lower dimensional systems. All electron calculations with relaxed core orbitals are practically prohibitive^{118,119} and calculations in 0D–2D periodicity can only be accomplished by a decoupling scheme.¹²⁰

5. COMPUTATIONAL DETAILS

All levels of electronic structure theory used in the present work, i.e., DFT, RPA, and Møller–Plesset perturbation theory of second order¹²¹ (MP2), employ RI factorization in Coulomb terms. The prefix “RI” is thus implied if it is not explicitly mentioned. DFT calculations employ the generalized gradient approximation of Perdew, Burke, and Ernzerhof¹²² (PBE) and, in selected cases, Grimme’s dispersion correction.⁷⁰ All DFT and MP2 results are obtained from calculations performed with Turbomole revision 7.1.^{112,113,123} Triple- ζ valence basis sets with polarization functions¹²⁴ (TZVP), augmented quadruple- ζ basis sets¹²⁵ (QZVPPD), and Dunning’s correlation consistent triple- ζ to quintuple- ζ valence basis sets¹²⁶ (cc-pVXZ, X = T, Q, 5) are used as orbital basis sets. Dunning’s augmented (aug) basis sets are used in addition.¹²⁷ Corresponding auxiliary basis sets are used in DFT, MP2, and RPA calculations.^{128–131} DFT calculations employ grid sizes 3 and 5 in the numerical integration of the exchange–correlation term.¹³² DFT energies are converged within 10^{-7} hartree, if the KS reference state is used for RPA calculations. Hartree–Fock energies of the infinite 1D chains are obtained with a preliminary implementation of the Fock exchange¹³³ and always use 15 k -points. RPA correlation energy calculations are performed employing 60 to 150 frequency points.⁷³ As explained for the underlying DFT implementation in ref 112, Γ -centered uniform grids similar to the Monkhorst–Pack grids¹³⁴ are used for wave vectors \mathbf{q} and \mathbf{k} . Calculations of crystal far field contributions use a maximum multipole order $l_{\text{max}} = 20$. Core orbitals are not frozen in the correlation energy calculations, as this feature is still missing in our preliminary RPA program. Molecular RPA energies from our implementation were checked against the reference implementation from ref 73; both implementations yield virtually the same correlation energies.

The timings shown in Figure 7 are obtained from calculations performed on Intel Xeon E5–2667 3.2 GHz processors with 25 MB cache and 256 GB memory on a CentOS 7–2 system working with a Samsung SM863 series solid state drive.

Energies are obtained from supercells in the Γ -point approach and primitive cells using a corresponding wave vector grid. For this purpose, an n -fold supercell is defined as a cell

comprising n primitive cells along each periodic direction. Similarly, an n -fold equispaced wave vector grid consists of n wave vectors along each reciprocal lattice direction in the FBZ.

Figure 3 shows primitive cells of crystal models from the present work. For methane and naphthalene, the structures of

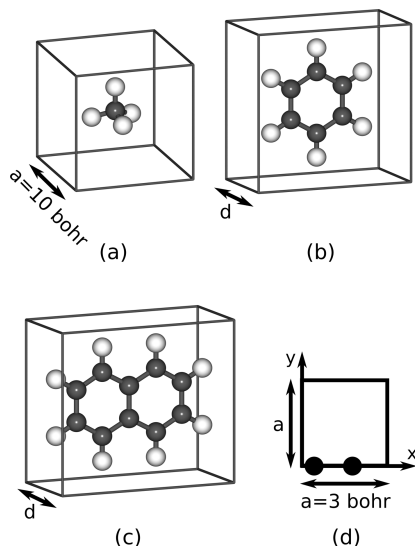


Figure 3. Periodic models: (a) cubic methane; stacking 1D chains of (b) benzene and (c) naphthalene in eclipsed conformation; (d) unit cell for Figure 8 containing two atoms at 0.2 and 1.6 bohr along x .

the single molecules are optimized using the PBE/TZVP method. The molecular structure of benzene is taken from ref 135, which is a result of CCSD(T)/cc-pVQZ and experimental data. Coordinates of the structures can be found in the Supporting Information. All monomer geometries do not vary in our calculations.

All energies are counterpoise corrected by the Boys–Bernardi scheme.¹³⁶ For periodic systems, counterpoise corrected monomer energies are obtained from 0D calculations, which include a finite array of ghost molecules from the periodic environment centered about the monomer. The selected sizes of the ghost arrays lead to energy corrections converged within chemical accuracy. For the methane models, a 5-fold ghost array is used. Benzene and naphthalene chains employ 11-fold ghost arrays. In addition, the basis extrapolation of ref 75 is applied in selected cases.

6. RESULTS AND DISCUSSION

6.1. Errors Due to RI and Charge Projection. We start our discussion with an investigation of numerical errors introduced by the RI approximation and the charge projection of the auxiliary basis functions in the SCF Coulomb energy and RPA correlation energy. For test systems of all periodic dimensions using TZVP basis sets for orbital expansion and universal auxiliary basis sets, RI errors in absolute SCF Coulomb energies are in the range of 0.013 kcal/mol (21 μ hartree) and per atom.⁹¹ These errors are comparable to typical errors of robust RI schemes.¹²⁹ Errors in RPA correlation energies introduced by RI are calculated and discussed by Eshuis et al.⁷³ They found maximum RI errors of 100 μ hartree in absolute correlation energies for small molecules using aug-cc-pVQZ basis sets. If dense extended systems are considered, then the RI errors

may decrease further because the nonorthogonal auxiliary GTF form a basis closer to the CBS limit.

In the present work, we address the overall impact of charge projection on RI-RPA energies. This can be tested with molecules and, therefore, the 24 weakly interacting dimers of the A24 set are taken from Řezáč et al.,¹³⁷ for which highly accurate CCSD(T) energy benchmarks at the CBS limit exist. In our test, charge projection is switched on or off in the Coulomb energy of the SCF procedure that determines KS orbitals and orbital energies and in the subsequent RI-RPA energy calculation. RI-RPA energies are affected by charge projections indirectly through the orbitals and their energies and directly in the RI-approximated Hartree kernel. The results are shown in Table 1 and demonstrate that effects from charge projection of

Table 1. Absolute Deviations (abs. dev.) [kcal/mol] between Calculations Employing Charge Projected and Unprojected Auxiliary Basis Sets for RPA Correlation Energies [ΔE^{CRPA}], Total RPA Energies [ΔE^{RPA}], and Interaction Energies [ΔE_b]. The A24 Test Set and QZVPPD Orbital Basis Sets Are Used

	ΔE^{CRPA}	ΔE^{RPA}	ΔE_b
max. abs. dev.	6.7×10^{-4}	3.4×10^{-3}	1.7×10^{-3}
mean abs. dev.	1.6×10^{-4}	1.5×10^{-3}	6.6×10^{-4}

at most 2×10^{-3} kcal/mol are negligible compared to the mean absolute error of 0.4 kcal/mol in RPA interaction energies. The RPA interaction errors are obtained from aug-cc-pVQZ/SZ extrapolated RI-RPA correlation energies compared to the CCSD(T)/CBS benchmarks. All RI-RPA interaction energies from the A24 set represent upper bounds with respect to the CCSD(T) reference, see Figure 4. The small influence of the

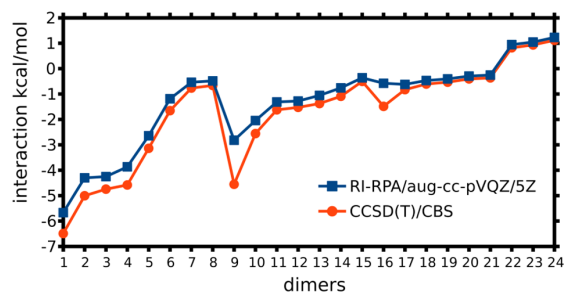


Figure 4. Interaction energies for the A24 set. CCSD(T)/CBS data are taken from ref 137.

charge projection is not surprising, as it reduces the rank of the original basis, N_{aux} effectively by one.⁹¹ As this reduction corresponds to the removal of a single charged GTF combination that should not contribute to the fit of charge neutral distributions, the rank reduction should not affect the final Coulomb energies unless the auxiliary basis set size is comparably small.

6.2. Methane Models. Turning to periodic systems, RPA/TZVP correlation binding energies are investigated for methane crystal models comprising up to 64 methane molecules in the unit cell. All models represent supercells obtained from the unit cell shown in Figure 3. Table 2 summarizes the results for increasing size of n -fold supercells at the Γ -point and, alternatively, for increasing density of n -fold wave vector grids.

Table 2. Correlation Contribution to RPA/TZVP Binding Energies [kcal/mol] per Molecule for Methane Crystal Models from Calculations Employing k-Point Sampling and Γ -Point Supercell Approach

n	1D	2D	3D
mol ^a	-232.2276	-232.2686	-232.3290
1	-0.2164	-0.6716	5.1282 ^b
2	-0.1458 ^b	-0.3464 ^b	0.2713 ^b
3	-0.1058	-0.2483	-0.1527 ^b
4	-0.0954 ^b	-0.2243 ^b	-0.2651 ^b
5	-0.0918	-0.2159	
7	-0.0896 ^c	-0.2103 ^c	
9	-0.0890 ^c	-0.2086 ^c	
11	-0.0888 ^c	-0.2079 ^c	
15	-0.0886 ^c	-0.2074 ^c	
21	-0.0885 ^c		

^aCounterpoise corrected RPA correlation energy [kcal/mol] of the CH₄ molecule in the gas phase. ^bOnly Γ -point supercell. ^cOnly k-point sampling.

Energies for $n = 1-5$ are calculated with the supercell approach, and odd $n = 1-21$ for 1D and 2D systems are calculated with the wave vector approach. Since correlation energies in hartree agree at least in the first nine digits between these two approaches, Table 2 shows one value for each n and periodicity. For 1D and 2D systems, the dispersive binding is numerically converged within 10^{-3} kcal/mol for $n = 15$. For the 3D system, the interaction is predicted to be repulsive for the smallest n , which is physically wrong. As explained in Appendix A, only the Γ -point approximation is currently available for the 3D case. The computational demand of the supercell approach on the Γ -point becomes quickly prohibitive for increasing n , and the 3D system is thus investigated until $n = 4$, for which the dispersive binding is already stronger than for the 2D system. In Figure 5, the RPA correlation energy changes are plotted

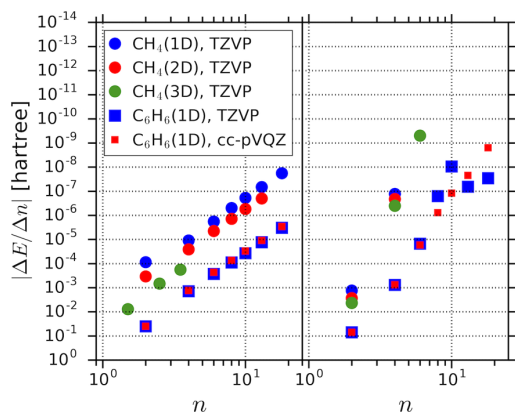


Figure 5. Energy convergence with number of wave vectors, n , along each periodic direction. Left: RPA correlation energy. Right: Total PBE energy. Values below 10^{-10} hartree are not shown.

against n and decrease algebraically, while the total DFT energy changes converge much faster to zero.

6.3. Benzene and Naphthalene Models. Next, we investigate the total energy binding curves for weakly bound stacked aromatic molecules in oligomers and infinite chains. In our discussion, we stick to well-ordered, highly symmetric structures in order to provide results that can be easier com-

pared and benchmarked with very accurate methods from present literature and future work.

Figure 6 shows the binding curves of the benzene dimer and Table 3 lists equilibrium parameters subject to the symmetry constraints. All binding energies are normalized to a single monomer for direct comparison among oligomers and chains. As expected, the semilocal PBE functional predicts an unphysical unbound system. The missing mid and long range dispersion interactions can be included with Grimme's dispersion correction,^{70,138} yielding a binding energy and an equilibrium spacing that agree with the CCSD(T) reference data¹³⁹ within 0.1 kcal/mol and 0.1 Å. A QCISD(T) calculation provides values very close to this reference.¹⁴⁰ The MP2 method overbinds compared to the reference. RPA/TZVP underbinds significantly, while aug-cc-pVTZ/QZ basis set extrapolation yields only 0.2 kcal/mol underbinding and a spacing that deviates 0.03 Å from the reference.

For a selected near equilibrium spacing, 4.02 Å, interaction energies of the tetramer and octamer, Figure 6, are calculated on the RPA/TZVP level. The interaction per benzene ring changes by -0.2 kcal/mol from the dimer to the tetramer and by -0.1 kcal/mol from the tetramer to the octamer. The binding energies of all oligomers represent upper bounds for the value of the periodic chain.

Turning to the infinite benzene chain, Figure 6 and Table 3, the binding energy per monomer is merely 0.1 kcal/mol stronger than in the octamer at the RPA/TZVP level. We conclude that the major part of binding in this system originates from rather local contributions. Figure 6d shows that the system is dispersion bound as the HF and the correlation contributions to the binding are repulsive and attractive, respectively. In the limit of large spacings, intermolecular interactions vanish in agreement with the physical expectation. The basis set extrapolated RPA binding energy is 0.7 kcal/mol weaker than the PBE-D value. PBE-D and RPA predict that the spacing in the chain is virtually the same as in the dimer. For the chain with an intermonomer distance of 3.18 Å, the convergence behavior of RPA correlation for n -fold supercells and wave vector grids is investigated in Table 4. To obtain values that are numerically reliable in the range of chemical accuracy, $n \geq 7$ should be used. The supercell and k-point approach agree within 2×10^{-7} hartree. Figure 5 illustrates the energy changes with n . Some of the PBE energy changes below 10^{-7} hartree look scattered as they are close to the SCF convergence threshold.

In comparison to benzene, the naphthalene models exhibit a larger contact area between the molecules, a smaller molecular orbital energy gap (e.g., 3.4 vs 5.1 eV for PBE/TZVP), and a higher molecular isotropic polarizability (e.g., 118 vs 66 au for PBE/TZVP). This leads to an increase of intermolecular mid and long-range correlation. Total energy binding curves of the 1D chain are shown in Figure 6 and more equilibrium data are provided in Table 3. The PBE-D and RPA methods employing TZVP basis sets predict approximately the same equilibrium spacing of at least 3.92 Å for the dimer and the chain. In the dimer case, the basis set extrapolation for RPA shortens this stacking distance to 3.83 Å. An available CCSD(T) result yields 3.88 Å.¹⁴¹ The trends in the binding energies are similar to those found for the benzene models.

Comparing benzene and naphthalene results with each other, the equilibrium spacing decreases in the range from -0.02 to -0.13 Å for the dimers and similarly for the chains, where RPA results exhibit the largest changes. The binding increases by around 1 and 2 kcal/mol from the benzene to the naphthalene

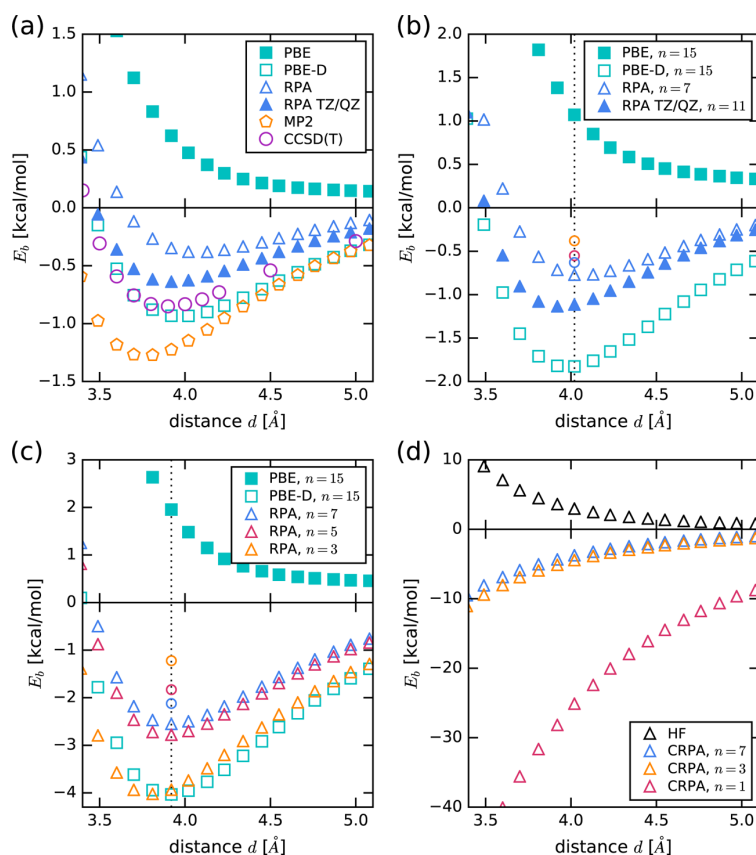


Figure 6. Binding energies per molecule for (a) benzene dimer, (b) periodic benzene chain, and (c) periodic naphthalene chain. Circles on dotted lines: dimer (orange), tetramer (red), and octamer (blue). (d) HF and RPA correlation contributions for periodic benzene chain. TZVP basis employed except for estimated CCSD(T)/aug-cc-pVQZ* from ref 139 and for aug-cc-pVTZ/QZ (a), and cc-pVTZ/QZ (b), basis set extrapolation (TZ/QZ).

Table 3. Intermonomer Equilibrium Spacings d [Å] and Binding Energies E_b per Monomer [kcal/mol]

structure	method	d	E_b
C_6H_6 (dimer)	Est. CCSD(T)/aug-cc-pVQZ* ^a	3.90	-0.85
	QCISD(T)/CBS ^b	3.92	-0.83
	PBE-D/TZVP	3.97	-0.94
	MP2/TZVP	3.77	-1.28
	RPA/TZVP	4.08	-0.38
	RPA/aug-cc-pVTZ/QZ ^c	3.93	-0.64
C_6H_6 (1D)	PBE-D/TZVP	3.98	-1.83
	RPA/TZVP ^d	4.07	-0.78
	RPA/cc-pVTZ/QZ ^e	3.94	-1.14
$C_{10}H_8$ (dimer)	Est. CCSD(T)/ha-cc-pVTZ ^f	3.88	-1.98
	PBE-D/TZVP	3.92	-2.02
	RPA/TZVP	3.95	-1.23
	RPA/aug-cc-pVTZ/QZ ^c	3.83	-1.64
$C_{10}H_8$ (1D)	PBE-D/TZVP	3.92	-4.03
	RPA/TZVP ^d	3.93	-2.55

^aEstimate taken from ref 139; structure from ref 135. ^bTaken from ref 140; QCISD(T)/aug-cc-pVTZ-optimized structure. ^cContains HF/aug-cc-pVQZ binding energy. ^d $n = 7$. ^eContains HF/TZVP binding energy; correlation part with $n = 11$. ^fEstimate taken from ref 141; CCSD(T)/ha-cc-pVDZ-optimized structure.

dimer and chain, respectively. The relative and absolute deviations of RPA binding from the reference decrease for the more extended π -system of naphthalene. The stacking

Table 4. RPA/TZVP Correlation Energies [hartree] of 1D Benzene Chain in Wave Vector and Supercell Approach for $a = 6.0$ bohr (3.18 Å)

n	k -points	supercell
1	-1.7956140	-1.7956140
3	-1.7163669	-1.7163671
5	-1.7136192	-1.7136193
7	-1.7130752	-1.7130754
9	-1.7128945	
11	-1.7128202	
15	-1.7127674	
21	-1.7127476	

models discussed in this work provide upper bounds for graphite, for which a layer spacing of 3.42 Å and a binding of 0.88 kcal/mol per C atom was found with RPA and in experiment for the AA layered conformation.¹⁴²

6.4. Timings. For large systems, the bottleneck in our implementation is the $O(N^4)$ step of the \mathbf{B} matrix contraction with \mathbf{G} (see eq 53). In most calculations performed with the preliminary implementation for the present work, however, the calculation of the CNF contribution to lattice sums in the \mathbf{B} matrix requires also a major part of the CPU time. The CPU timings observed, Figure 7, agree with the formal scaling behavior predicted in section 3 for the number of primitive cells in direct space, N , and with respect to the number of wave

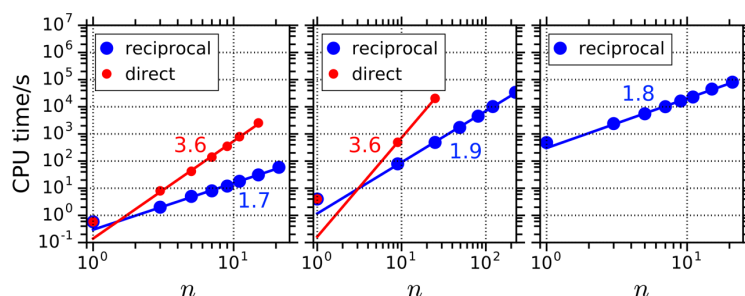


Figure 7. CPU times on single core for RPA correlation energy calculations versus n (total number of primitive cells in *direct* space and wave vectors in *reciprocal* space). Colored digits x indicate $O(N^x)$ scaling. From left to right (structure/orbital basis): $\text{CH}_4(1\text{D})/\text{TZVP}$, $\text{CH}_4(2\text{D})/\text{TZVP}$, $\text{C}_6\text{H}_6(1\text{D})/\text{cc-pVQZ}$.

vectors, N_k . We observe $O(N^{3.6})$ scaling in direct space and $O(N_k^{1.9})$ scaling in reciprocal space.

6.5. Coulomb-Metric Matrix. Characteristic plots of the Coulomb-metric matrix $J(\mathbf{q})$, eqs 42 and 77, for a line and a square lattice are shown in Figure 8. Our illustration is restricted to matrix elements J_{PQ} defined with s- and p-functions.

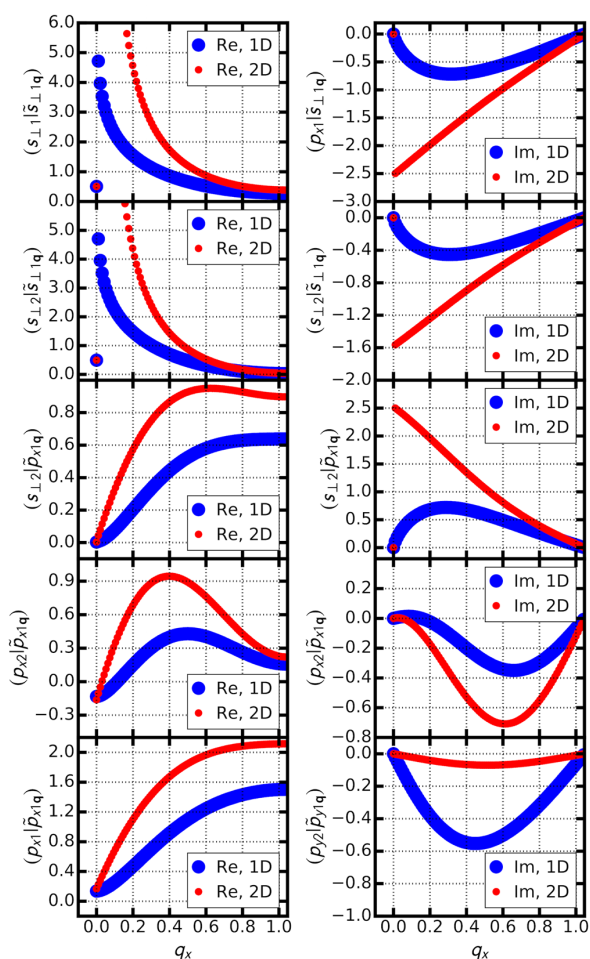


Figure 8. $J(q_x, 0, 0)$ matrix [hartree] plotted for $q_x \in [0, \pi/a]$. Elements are shown for one s- and one p-type GTF (exponent 0.6 au) centered about each of two atoms for a line (1D) and square (2D) lattice, see Figure 3.

Features shared by all matrix elements are the vanishing gradient of the real part on the FBZ boundary and the vanishing imaginary part at the Γ -point and FBZ boundary. In the 1D and 2D systems, the real parts of matrix elements between unprojected s-functions exhibit a singularity at Γ , which is cured by the charge projection at Γ leading merely to a discontinuity. In the 1D system, cusps are not visible. In the 2D system, however, matrix elements between s- and p-functions exhibit a cusp at Γ , which turns into a discontinuity due to charge projected s-functions at Γ . In addition, cusps without discontinuity at Γ may appear in J_{PQ} elements between p-functions in the 2D system. The plots suggest that the Coulomb-metric matrix as a function of the exciton vector \mathbf{q} represents a smooth differentiable function except for the region around Γ .

7. CONCLUDING REMARKS

We developed and implemented a canonical orbital RI-RPA method that describes molecules and crystals on an equal footing employing local auxiliary basis functions and a recursive multipole method in direct space. Since auxiliary *atomic orbitals* were used, this method lays the groundwork for introducing molecular effectively linear scaling atomic orbital RI-RPA methods⁵⁸ into solid state calculations. As one ingredient of the underlying theory, we established the Hartree kernel under PBC in its RI-factorized translation-symmetry adapted supermatrix representation.

For the investigated models, the use of translation symmetry led to computational speedups of typically 10–100. We provided numerical proof that the wave vector and Γ -point supercell approaches yield equivalent results. Our results obtained for stacks of aromatic molecules confirmed previous findings of molecular RPA studies on weakly bound dimers: structural parameters were accurately predicted,^{3,38} and basis set extrapolation toward the CBS limit was obligatory for evaluation of binding energies, which were systematically underestimated.³⁵ We observed that Bloch orbitals of longer wavelengths have a much larger effect on intermolecular correlation energies than on total SCF energies.

Existing recursive multipole methods were previously developed for long-range interactions in Coulomb terms of SCF methods, where lattice sums of the totally symmetric electronic ground state density and nuclear point charge arrays were evaluated.^{100,112,143} Our modified recursive multipole method ensures numerically converged values of Coulomb lattice sums and works also for Bloch orbitals belonging to other irreducible representations than the totally symmetric representation Γ . To use auxiliary GTF for RI factorizations in solid state

methods, we demonstrated that divergent elements in the Coulomb-metric matrix were avoided for Γ , when charged auxiliary basis functions were projected to charge neutral linear combinations. Therefore, solid state post-SCF methods with nonlocal correlation contributions, e.g., RPA, MP2, and coupled cluster methods may now be accelerated employing the GTF-based RI approximation and the recursive multipole method.

APPENDIX A

Coulomb Lattice Summation

Lattice sums of Coulomb interaction integrals

$$\phi_K = \sum_{\mathbf{L} \in K} e^{i\mathbf{q}\cdot\mathbf{L}} (\zeta^0 \rho^{\mathbf{L}}) \quad (67)$$

must be evaluated for $\mathbf{J}(\mathbf{q})$ and $\mathbf{B}(\mathbf{q})$ from eqs 42 and 48, where ζ^0 and $\rho^{\mathbf{L}}$ represent local distribution functions assigned to cells $\mathbf{0}$ and \mathbf{L} , respectively. The sum of \mathbf{L} reaches over the entire crystal. The evaluation is conducted by a direct summation of contributions from groups of cells \mathbf{L} around the central cell $\mathbf{0}$ for a very large finite array K in real space. The size of this array is chosen large enough to yield a converged value for ϕ_K within a given threshold. The nonzero wave vectors in our electronic structure calculations are chosen to yield Bloch phase factors, $e^{i\mathbf{q}\cdot\mathbf{L}}$, which are periodic on finite n -fold supercells.¹¹² In this way, the lattice sum ϕ_K is always equivalent to lattice sums with $\mathbf{q} = \mathbf{0}$ defined on a supercell lattice. Therefore, the rules of convergence^{100,144–147} known for $\mathbf{q} = \mathbf{0}$ can be applied to ϕ_K within our restricted wave vector set. In 1D and 2D systems, ϕ_K is absolutely convergent if ζ^0 exhibits arbitrary values in its multipole moments and $\rho^{\mathbf{L}}$ is charge neutral,^{100,146}

$$\int d^3r \rho^{\mathbf{L}}(\mathbf{r}) = 0 \quad (68)$$

Absolute convergence in this context means that the grouping of \mathbf{L} in eq 67 is irrelevant and thus $\phi_K \rightarrow \phi$ becomes independent of the specific choice K . In 3D systems, absolute convergence toward ϕ for ζ^0 with arbitrary moments is achieved with cell images $\rho^{\mathbf{L}}$, which exhibit zero charge, dipole, and quadrupole moments ($\omega_m = 0$ for $l = 0-2$ and $m = 0, \dots, \pm l$). ϕ can still change for variations in images $\rho^{\mathbf{L}}$ that keep the periodic distribution ρ unchanged and keep all $\omega_{0-2,m} = 0$ because ϕ depends also on the trace of the second electric moment tensor of $\rho^{\mathbf{L}}$.¹¹¹ If this trace is zero, then ϕ belongs to the Ewald limit.¹⁴⁴ Alternatively, if the local function ζ^0 is charge neutral, then $\omega_{0-1,m} = 0$ in $\rho^{\mathbf{L}}$ are sufficient to obtain the Ewald limit for ϕ in 3D systems without quadrupole and second moment correction.

The integrals defining $\mathbf{J}(\mathbf{q})$ and $\mathbf{B}(\mathbf{q})$ contain auxiliary Bloch functions, eq 37, as periodic distribution functions. The charge of an unnormalized auxiliary Bloch function is determined by

$$z_{p\mathbf{q}} = \int d^3r \tilde{m}_{p\mathbf{q}}(\mathbf{r}) = z_p \sum_{\mathbf{L}} e^{i\mathbf{q}\cdot\mathbf{L}} \quad (69)$$

$$= N_{\text{UC}} \times \delta_{\mathbf{q}\mathbf{K}} \times z_p \quad (70)$$

where

$$z_p = \int d^3r \eta_p^{\mathbf{L}}(\mathbf{r}) \quad (71)$$

is the charge of a single auxiliary GTF.

At $\mathbf{q} = \mathbf{0}$, the Bloch function is charged if the GTF is charged. This charge can be corrected to zero by replacing the auxiliary GTF basis by a projected one,

$$\eta_{\perp p}^{\mathbf{L}}(\mathbf{r}) = \sum_{\mathbf{Q}} P_{\perp p\mathbf{Q}} \eta_{\mathbf{Q}}^{\mathbf{L}}(\mathbf{r}) \quad (72)$$

The concept of the charge projection

$$\mathbf{P}_{\perp} = \mathbf{1} - \mathbf{nn}^T \quad (73)$$

is explained in detail in ref 91. The normalized charge vector \mathbf{n} of N_{aux} auxiliary basis functions η_p contains the elements

$$n_p = \frac{z_p}{|\mathbf{z}|}, \quad \mathbf{z} = (z_1, \dots, z_{N_{\text{aux}}}) \quad (74)$$

For $\mathbf{q} = \mathbf{0}$, $\eta_p^{\mathbf{L}}$ is replaced by $\eta_{\perp p}^{\mathbf{L}}$ in all equations of sec 2. In addition, the resulting projected Coulomb-metric matrix (compare with eq 42),

$$J_{\perp p\mathbf{Q}}(\mathbf{q}) = (\eta_{\perp}^0 | \tilde{h}_{\perp p\mathbf{Q}}^{\mathbf{L}}) \quad (75)$$

contains a zero eigenvalue and cannot be inverted. \mathbf{J}_{\perp} is thus modified by adding a complement projection matrix

$$\mathbf{P}_{\parallel} = \mathbf{nn}^T \quad (76)$$

which replaces the zero eigenvalue by 1 in the resulting Coulomb-metric matrix

$$\mathbf{J}(\mathbf{q}) = \mathbf{J}_{\perp}(\mathbf{q}) + \mathbf{P}_{\parallel} \quad (77)$$

It was shown in ref 91 that this modified \mathbf{J} does not change the solution of the fitting coefficients belonging to \mathbf{J}_{\perp} . This definition of \mathbf{J} can then be used in eq 41 for $\mathbf{q} = \mathbf{0}$. Within the charge projected basis, local functions $\eta_{\perp p}^0$ always are charge neutral and thus a quadrupole and second moments correction is never necessary.

For $\mathbf{q} \neq \mathbf{0}$, the charge projected basis destroys energy invariance under translation of the unit cell content, as can be simply proven with a quasi-isolated molecule crossing the boundary of a very large unit cell. Charge projection is, however, not necessary, if $\mathbf{q} = \mathbf{K}/n$ for $\mathbf{K} \neq \mathbf{0}$ and $|n| > 1$. In this case, the Bloch function is always charge neutral in each n -fold supercell while the corresponding local GTF may be charged. Therefore, lattice sums ϕ can be computed for an unprojected auxiliary basis, if necessary, corrected up to quadrupole and second moments.

Once the constraints on the Bloch functions are established, the lattice sum in eq 67 is decomposed into crystal near field (CNF) and crystal far field (CFF) terms. The CNF term contains contributions from \mathbf{L} within the CNF radius, R_{CNF} , about the center of the reference unit cell $\mathbf{0}$. The precise definition of R_{CNF} is found in ref 112 and depends on the extents of ζ^0 and ρ^0 . Contributions from \mathbf{L} outside the CNF radius belong to CFF. The CNF term is computed by direct integration. The CFF term,

$$\begin{aligned} \phi^{\text{CFF}} &= \sum_{\mathbf{L}}^{\text{CFF}} e^{i\mathbf{q}\cdot\mathbf{L}} (\zeta^0 \rho^{\mathbf{L}}) \\ &= \sum_{l=0}^{\infty} \sum_{m=-l}^l M_{lm}[\zeta^0] \times L_{lm} \left[\sum_{\mathbf{L}}^{\text{CFF}} e^{i\mathbf{q}\cdot\mathbf{L}} \rho^{\mathbf{L}} \right] \end{aligned} \quad (78)$$

is calculated with a multipole expansion about the center of cell $\mathbf{0}$. Definitions of multipole moments M_{lm} and local moments L_{lm} of point charges, GTF, and GTF products and schemes to

calculate the moments can be found in ref 148. The local moments of the entire CFF are obtained by a recursive scheme from a small set of shift operators¹⁴⁹ and multipole moments of the single cell content. The recursion scheme was published for $\mathbf{q} = \mathbf{0}$.¹⁰⁰ In the following, this recursion is used in an extended scheme for $\mathbf{q} \neq \mathbf{0}$.

Figure 9 illustrates the arrangement of \mathbf{L} in domains used for our periodic multipole algorithm to compute ϕ^{CFF} . There

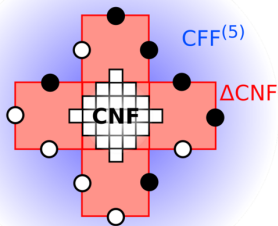


Figure 9. Domains of periodic FMM scheme. Circles represent positions of dangling fictitious charges from the dipole correction. See further explanation in text.

is the CNF of the unit cell $\text{UC} \equiv \text{UC}^{(1)}$ determined by R_{CNF} . The CNF is enclosed by and part of the $\text{CNF}^{(n)}$ consisting of n -fold supercells $\text{UC}^{(n)}$ within the radius $R_{\text{CNF}}^{(n)}$, that is, the crystal near-field radius based on the extent of the supercell distribution $\rho_{\text{UC}^{(n)}}^0$. The difference set $\text{CNF}^{(n)} \setminus \text{CNF}$ of \mathbf{L} defines ΔCNF . The set of \mathbf{L} outside $\text{CNF}^{(n)}$ is $\text{CFF}^{(n)}$, and the union of $\text{CFF}^{(n)}$ and ΔCNF is the CFF. Using the language of Kudin and Scuseria¹⁰⁰ the following steps define our revised multipole method that yields ϕ^{CFF} ,

- (1) Select n , to build a grid of wave vectors $\mathbf{q} = \mathbf{K}/n$ with reciprocal lattice points \mathbf{K} .
- (2) Form two sums of pristine multipole-to-multipole shift operators \mathcal{M} from $\mathbf{0}$ to all \mathbf{L} in the n -fold supercell. One sum includes the real part of the Bloch phase,

$$M^{\text{Re}} = \sum_{\mathbf{L}}^{\text{UC}^{(n)}} \cos(\mathbf{q} \cdot \mathbf{L}) \mathcal{M}(\mathbf{L}) \quad (79)$$

the other includes the imaginary part,

$$M^{\text{Im}} = \sum_{\mathbf{L}}^{\text{UC}^{(n)}} \sin(\mathbf{q} \cdot \mathbf{L}) \mathcal{M}(\mathbf{L}) \quad (80)$$

- (3) Apply $M^{\#}$ ($\# = \text{Re}, \text{Im}$) with a multipole-to-multipole shift operation, \triangleleft , to the multipole moments of the reference unit cell about its cell center,

$$M[\#\{\rho_{\text{UC}^{(n)}}^0(\mathbf{q})\}] = M^{\#} \triangleleft M[\rho_{\text{UC}}^0] \quad (81)$$

to obtain multipole moments of the supercell density.

- (4) For 3D systems, determine fictitious point charges, which cancel the dipole moments of real and imaginary parts of the supercell density,¹⁴⁶ and add the fictitious charge distribution to the supercell ($\# = \text{Re}, \text{Im}$),

$$M[\#\{\tilde{\rho}_{\text{UC}^{(n)}}^0(\mathbf{q})\}] = M[\#\{\rho_{\text{UC}^{(n)}}^0(\mathbf{q})\}] + M_{\text{dip}}^{\#} \quad (82)$$

- (5) Build M_* and L_* from pristine multipole-to-multipole and multipole-to-local shift operators, \mathcal{M} and \mathcal{L} , as devised by Kudin et al., however, using n -fold supercells \mathbf{S} ,

$$M_* = \sum_{\mathbf{S}}^{(\text{UC}^{(n)})^{(3)}} \mathcal{M}(\mathbf{S}) \quad (83)$$

$$L_* = \sum_{\mathbf{S}}^{\text{FF}'(\text{UC}^{(n)})} \mathcal{L}(\mathbf{S}) \quad (84)$$

where $(\text{UC}^{(n)})^{(3)}$ and $\text{FF}'(\text{UC}^{(n)})$ represent the 3-fold of the n -fold supercell and the first FMM zone of $\text{UC}^{(n)}$, respectively. Compute the final lattice operator S from M_* and L_* by recursion (eq 24 in ref 100).

- (6) Calculate local moments $L_{\text{dip}}^{\#}$ of fictitious inverted charges to cancel dangling charges at the $\text{CNF}^{(n)}/\text{CFF}^{(n)}$ boundary from step 4 (see also Figure 9).^{146,150}
- (7) Calculate local moments of the $\text{CFF}^{(n)}$ domain using the results from steps 4, 5, and 6 ($\# = \text{Re}, \text{Im}$),

$$L^{\#}(\#\text{CFF}^{(n)}) = S \otimes M[\#\{\tilde{\rho}_{\text{UC}^{(n)}}^0(\mathbf{q})\}] + L_{\text{dip}}^{\#} \quad (85)$$

where \otimes represents the multipole-to-local shift operation.

- (8) Form two sums, for real and imaginary parts, of pristine multipole-to-local shift operators from $\mathbf{0}$ to all \mathbf{L} in the ΔCNF domain,

$$L^{\text{Re}} = \sum_{\mathbf{L}}^{\Delta\text{CNF}} \cos(\mathbf{q} \cdot \mathbf{L}) \mathcal{L}(\mathbf{L}) \quad (86)$$

$$L^{\text{Im}} = - \sum_{\mathbf{L}}^{\Delta\text{CNF}} \sin(\mathbf{q} \cdot \mathbf{L}) \mathcal{L}(\mathbf{L}) \quad (87)$$

- (9) Calculate local moments of the entire CFF ($\# = \text{Re}, \text{Im}$),

$$L^{\#}(\#\text{CFF}) = L^{\#}(\#\text{CFF}^{(n)}) + L^{\#} \otimes M[\rho_{\text{UC}}^0] \quad (88)$$

- (10) Perform contraction between multipole moments of ζ^0 and local moments from step 9 as shown in eq 78; however, do it separately for real and imaginary parts of the CFF distribution. Add real and imaginary parts after contraction to obtain the complete complex valued interaction ϕ^{CFF} .

If the real and imaginary parts of $\exp[i(\mathbf{q} \cdot \mathbf{L})] \rho^{\text{L}}$ are treated separately in the multipole methods, then the moments maintain the properties of real densities, for example,

$$M_{lm} = (-1)^m M_{lm}^* \quad (89)$$

If ζ^0 is charged in 3D systems, then the quadrupole and second moments correction must be applied in steps 4 and 6, too. For the dipole correcting terms, $M_{\text{dip}}^{\#}$ and $L_{\text{dip}}^{\#}$, \mathbf{q} -independent moments of unit point charge distributions are precalculated once and rescaled for the actual $\rho_{\text{UC}^{(n)}}^0(\mathbf{q})$.

APPENDIX B

Translation-Symmetry Adapted RI Hartree Kernel

This appendix outlines the derivation of eq 49 starting from the RI approximation

$$V_{11, I \mathcal{A} \sigma \mathcal{J} \mathcal{B} \tau}(\mathbf{q}, \mathbf{q}') \equiv (\mathcal{A} | \sigma | \Omega_{\mathcal{J} \mathcal{B} \tau}) \approx (\mathcal{A} | \sigma | \tilde{\Omega}_{\mathcal{J} \mathcal{B} \tau}) \quad (90)$$

by inserting the ansatz of eq 36,

$$V_{11, I, \mathcal{A}\sigma, \mathcal{J}\mathcal{B}\tau}^{\text{RI}}(\mathbf{q}, \mathbf{q}') = (\mathcal{A}\mathcal{I}\sigma) \sum_P d_P^{\mathcal{J}\mathcal{B}\tau} \eta_{P\mathbf{q}} \quad (91)$$

With the use of the density fit, eq 46, minor rearrangements yield

$$V_{11, I, \mathcal{A}\sigma, \mathcal{J}\mathcal{B}\tau}^{\text{RI}}(\mathbf{q}, \mathbf{q}') = \sum_Q (\mathcal{A}\mathcal{I}\sigma) \sum_P (\Lambda^{-1}(\mathbf{q}'))_{PQ} \eta_{P\mathbf{q}'} \times \left(\sum_R (\Lambda^{-1}(\mathbf{q}'))_{RQ}^* \tilde{\eta}_{R\mathbf{q}'}^* |\tilde{\varphi}_{jk, \tau}^*| \phi_{bk, +\mathbf{q}'}^0 \right) \quad (92)$$

Next, the first ERI in each product is reduced to the reference cell $\mathbf{L} = \mathbf{0}$ (cf. eq 30),

$$V_{11, I, \mathcal{A}\sigma, \mathcal{J}\mathcal{B}\tau}^{\text{RI}}(\mathbf{q}, \mathbf{q}') = \frac{1}{N_{\text{UC}}} \delta_{\mathbf{q}\mathbf{q}'} \times \sum_Q (\phi_{ak_i + \mathbf{q}\sigma}^{0*} \tilde{\varphi}_{jk, \sigma}^*) \sum_P (\Lambda^{-1}(\mathbf{q}))_{PQ} \tilde{\eta}_{P\mathbf{q}} \times (\phi_{bk_j + \mathbf{q}\tau}^{0*} \tilde{\varphi}_{jk, \tau}^*) \sum_R (\Lambda^{-1}(\mathbf{q}))_{RQ} \tilde{\eta}_{R\mathbf{q}}^* \quad (93)$$

This result represents eq 47 employing the definition of \mathbf{B} , eq 48. In summary, one \mathbf{q} -block in the RI-approximated \mathbf{V}_{11} submatrix (cf. Fig. 1) is

$$\mathbf{V}_{11}^{\text{RI}}(\mathbf{q}, \mathbf{q}') = \frac{1}{N_{\text{UC}}} \mathbf{B}(\mathbf{q}) \delta_{\mathbf{q}\mathbf{q}'} \mathbf{B}^\dagger(\mathbf{q}') \quad (94)$$

and the entire submatrix is given by

$$\mathbf{V}_{11}^{\text{RI}} = \frac{1}{N_{\text{UC}}} \mathbf{B} \mathbf{1} \mathbf{B}^\dagger \quad (95)$$

where the structure of \mathbf{B} is illustrated in Figure 1 and the unit matrix $\mathbf{1}$ is of the order $N_k \times N_{\text{aux}}$. Conducting this derivation for all submatrices $\mathbf{V}_{11}^{\text{RI}}$, $\mathbf{V}_{12}^{\text{RI}}$, and their complex conjugates yields the Hartree kernel of eq 22 in the translation-symmetry adapted RI form

$$\mathbf{V}^{\text{RI}} = \frac{1}{N_{\text{UC}}} \begin{pmatrix} \mathbf{B} \mathbf{1} \mathbf{B}^\dagger & \mathbf{B} \bar{\mathbf{1}} (\mathbf{B}^\dagger)^* \\ \mathbf{B}^* \bar{\mathbf{1}} \mathbf{B}^\dagger & \mathbf{B}^* \mathbf{1} (\mathbf{B}^\dagger)^* \end{pmatrix} \quad (96)$$

with $\bar{\mathbf{1}}$ defined in eq 51. Using the relations $\bar{\mathbf{1}} = \bar{\mathbf{1}} \mathbf{1}$ and $\mathbf{1} = \bar{\mathbf{1}} \bar{\mathbf{1}}$, the Hartree kernel can be entirely factorized as defined by eq 49.

APPENDIX C

Unit Cell Decomposition of the RPA Correlation Energy

This appendix shows that the RPA correlation energy of the total system decomposes into equal contributions from all unit cells of the crystal. Inserting the translation-symmetry adapted RI Hartree kernel, eq 49, into the RPA correlation energy, eq 19, and expanding the logarithm into powers of $\mathbf{V}^{\text{RI}} \mathbf{\Pi}_0$, we may investigate individual traces, eq 18, and may perform cyclic permutation,

$$\text{Tr} \left\{ (\mathbf{V}^{\text{RI}} \mathbf{\Pi}_0(iu))^n \right\} = \text{Tr} \left\{ \left(\frac{1}{N_{\text{UC}}} \mathbf{B}^\dagger \mathbf{\Pi}_0(iu) \mathbf{B} \right)^n \right\} \quad (97)$$

The matrix multiplication is conducted using the definitions of \mathbf{B} and $\mathbf{\Pi}_0$, eqs 50 and 13,

$$\text{Tr} \left\{ (\mathbf{V}^{\text{RI}} \mathbf{\Pi}_0(iu))^n \right\} = \text{Tr} \left\{ \left(\frac{1}{N_{\text{UC}}} [\mathbf{Q}^-(iu) + \bar{\mathbf{1}} \mathbf{Q}^{*-}(iu) \bar{\mathbf{1}}] \right)^n \right\} \quad (98)$$

with

$$\mathbf{Q}^-(iu) = \mathbf{B}^\dagger \boldsymbol{\pi}^-(iu) \mathbf{B} \quad (99)$$

As \mathbf{B} and $\boldsymbol{\pi}^-$ are \mathbf{q} -block diagonal, the product matrix \mathbf{Q}^- is also \mathbf{q} -block diagonal and of order $N_k \times N_{\text{aux}}$. Multiplying \mathbf{Q}^- with $\bar{\mathbf{1}}$ from left and right leads to a switch between \mathbf{q} - and $-\mathbf{q}$ -blocks in the result, $\bar{\mathbf{1}} \mathbf{Q}^- \bar{\mathbf{1}}$ (cf. Fig. 1). Therefore, the trace in eq 98 is split into a sum over \mathbf{q} and the trace of the remaining matrix index P ,

$$\text{Tr} \left\{ (\mathbf{V}^{\text{RI}} \mathbf{\Pi}_0(iu))^n \right\} = \sum_{\mathbf{q}} \text{Tr} \left\{ \left(\frac{1}{N_{\text{UC}}} [\mathbf{Q}^-(iu, \mathbf{q}) + \mathbf{Q}^{*-}(iu, -\mathbf{q})] \right)^n \right\} \quad (100)$$

where the summation over \mathbf{q} can be decoupled from order n . The summation of wave vectors \mathbf{k} in diagonal \mathbf{q} -blocks of \mathbf{Q}^- is then converted to a numerical integration on a finite grid via eqs 56 and 57,

$$\mathbf{Q}_{PQ}^-(iu, \mathbf{q}) = \frac{N_{\text{UC}}}{N_k} \sum_{ika\sigma} B_{ika\sigma P}^*(\mathbf{q}) \pi_{ika\sigma, ika\sigma}^-(iu, \mathbf{q}) B_{ika\sigma Q}(\mathbf{q}) \quad (101)$$

where the dimension of the matrices \mathbf{B} and $\boldsymbol{\pi}^-$ for index \mathbf{k} is reduced to the number of \mathbf{k} vectors, N_k , on the finite grid. The definition of \mathbf{Q}^- , eq 99, is left unchanged for finite \mathbf{k} grids, if the weights $1/N_k$ are introduced into eq 100,

$$\text{Tr} \left\{ (\mathbf{V}^{\text{RI}} \mathbf{\Pi}_0(iu))^n \right\} = \frac{N_{\text{UC}}}{N_k} \sum_{\mathbf{q}} \text{Tr} \left\{ \left(\frac{1}{N_k} [\mathbf{Q}^-(iu, \mathbf{q}) + \mathbf{Q}^{*-}(iu, -\mathbf{q})] \right)^n \right\} \quad (102)$$

where the sum over \mathbf{q} is also reduced to a finite grid. The two different contributions from the \mathbf{q} and $-\mathbf{q}$ vectors can be further summarized, if the inversion symmetry of orbital coefficients and energies in reciprocal space is employed,

$$C_{\mu p, -\mathbf{k}\sigma} = C_{\mu p \mathbf{k}\sigma}^* \quad (103)$$

$$\varepsilon_{p, -\mathbf{k}\sigma} = \varepsilon_{p \mathbf{k}\sigma} \quad (104)$$

If blocks belonging to \mathbf{k} and $-\mathbf{k}$ are interchanged in matrices \mathbf{B} and $\boldsymbol{\pi}^-$ and complex conjugation is applied to \mathbf{B} , then the diagonal blocks of \mathbf{q} and $-\mathbf{q}$ are equal using eqs 103 and 104,

$$\mathbf{Q}^-(iu, -\mathbf{q}) = [\mathbf{B}^\dagger(\mathbf{q}) \boldsymbol{\pi}^+(iu, \mathbf{q}) \mathbf{B}(\mathbf{q})]^* \quad (105)$$

This leads to

$$\mathbf{Q}(u, \mathbf{q}) \equiv -\frac{1}{N_k} [\mathbf{Q}^-(iu, \mathbf{q}) + \mathbf{Q}^{*-}(iu, -\mathbf{q})] = \frac{2}{N_k} \mathbf{B}^\dagger(\mathbf{q}) \mathbf{G}(u, \mathbf{q}) \mathbf{B}(\mathbf{q}) \quad (106)$$

with

$$\boldsymbol{\pi}^-(iu, \mathbf{q}) + \boldsymbol{\pi}^+(iu, \mathbf{q}) = -2\mathbf{G}(u, \mathbf{q}) \quad (107)$$

G is derived by expanding $\pi^\pm = -(\Delta \pm iu1)^{-1}$ in a Taylor series with respect to iu and analyzing the real and imaginary contributions. If the result, eq 106, is inserted into the trace expression, eq 102, and the traces of all orders n are contracted to the logarithm, then it follows

$$E_{UC}^{CRPA} \approx N_{UC} \times E_{UC}^{CRIRPA} \quad (108)$$

with the total RPA correlation energy from eq 19 and the RI-approximated RPA correlation energy per unit cell as defined in eq 52.

■ ASSOCIATED CONTENT

📄 Supporting Information

The Supporting Information is available free of charge on the ACS Publications website at DOI: 10.1021/acs.jctc.6b01146.

Unit cell definitions and coordinates of the model systems (TXT)

■ AUTHOR INFORMATION

✉ Corresponding Author

*E-mail: Asbjorn.Burow@cup.lmu.de.

ORCID

Asbjörn M. Burow: 0000-0003-3651-6650

Funding

This work was supported by the German Fund of Chemical Industry (Liebig Fellowship, Li 194/07).

Notes

The authors declare no competing financial interest.

■ ACKNOWLEDGMENTS

We thank Andreas Irmeler and Fabian Pauly from University of Konstanz for providing their Fock exchange in a prototype implementation for periodic 1D systems. A.M.B. thanks Arne Lünser from Ludwig-Maximilians Universität (LMU) Munich for fruitful discussions.

■ REFERENCES

- Jiang, H.; Engel, E. *J. Chem. Phys.* **2007**, *127*, 184108.
- Zhu, W.; Toulouse, J.; Savin, A.; Ángyán, J. G. *J. Chem. Phys.* **2010**, *132*, 244108.
- Mussard, B.; Szalay, P. G.; Ángyán, J. G. *J. Chem. Theory Comput.* **2014**, *10*, 1968–1979.
- Bleiziffer, P.; Krug, M.; Görling, A. *J. Chem. Phys.* **2015**, *142*, 244108.
- Grimme, S.; Steinmetz, M. *Phys. Chem. Chem. Phys.* **2016**, *18*, 20926–20937.
- Heßelmann, A.; Görling, A. *Mol. Phys.* **2011**, *109*, 2473–2500.
- Eshuis, H.; Bates, J. E.; Furche, F. *Theor. Chem. Acc.* **2012**, *131*, 1084.
- Ren, X.; Rinke, P.; Joas, C.; Scheffler, M. *J. Mater. Sci.* **2012**, *47*, 7447–7471.
- Bohm, D.; Pines, D. *Phys. Rev.* **1951**, *82*, 625–634.
- Pines, D.; Bohm, D. *Phys. Rev.* **1952**, *85*, 338–353.
- Bohm, D.; Pines, D. *Phys. Rev.* **1953**, *92*, 609–625.
- Pines, D. *Phys. Rev.* **1953**, *92*, 626–636.
- Gell-Mann, M.; Brueckner, K. A. *Phys. Rev.* **1957**, *106*, 364–368.
- Sawada, K. *Phys. Rev.* **1957**, *106*, 372–383.
- Sawada, K.; Brueckner, K. A.; Fukuda, N.; Brout, R. *Phys. Rev.* **1957**, *108*, 507–514.
- Nozières, P.; Pines, D. *Phys. Rev.* **1958**, *111*, 442–454.
- Langreth, D. C.; Perdew, J. P. *Phys. Rev. B* **1977**, *15*, 2884–2901.
- Langreth, D. C.; Perdew, J. P. *Solid State Commun.* **1975**, *17*, 1425–1429.

- Gunnarsson, O.; Lundqvist, B. I. *Phys. Rev. B* **1976**, *13*, 4274–4298.
- Callen, H. B.; Welton, T. A. *Phys. Rev.* **1951**, *83*, 34–40.
- Kubo, R. *Rep. Prog. Phys.* **1966**, *29*, 255–284.
- Nozières, P.; Pines, D. *The Theory of Quantum Liquids: Volume 1 & 2*, 3rd ed.; Advanced Books Classics; Perseus Books Publishing, 1999.
- Mussard, B.; Rocca, D.; Jansen, G.; Ángyán, J. G. *J. Chem. Theory Comput.* **2016**, *12*, 2191–2202.
- Oddershede, J.; Jørgensen, P.; Yeager, D. L. *Comput. Phys. Rep.* **1984**, *2*, 33–92.
- Salpeter, E. E.; Bethe, H. A. *Phys. Rev.* **1951**, *84*, 1232–1242.
- Fetter, A. L.; Walecka, J. D. *Quantum Theory of Many-Particle Systems*; Dover Publications: Mineola, NY, 1971; Chapter 4.
- Furche, F. *J. Chem. Phys.* **2001**, *114*, 5982–5992.
- Furche, F. *Phys. Rev. B: Condens. Matter Mater. Phys.* **2001**, *64*, 195120.
- Fuchs, M.; Gonze, X. *Phys. Rev. B: Condens. Matter Mater. Phys.* **2002**, *65*, 235109.
- Niquet, Y. M.; Fuchs, M.; Gonze, X. *Phys. Rev. A: At, Mol., Opt. Phys.* **2003**, *68*, 032507.
- Furche, F.; van Voorhis, T. *J. Chem. Phys.* **2005**, *122*, 164106.
- Furche, F. *J. Chem. Phys.* **2008**, *129*, 114105.
- Hellgren, M.; von Barth, U. *Phys. Rev. B: Condens. Matter Mater. Phys.* **2007**, *76*, 075107.
- Heßelmann, A.; Görling, A. *Mol. Phys.* **2010**, *108*, 359–372.
- Eshuis, H.; Furche, F. *J. Chem. Phys.* **2012**, *136*, 084105.
- Heßelmann, A. *Phys. Rev. A: At, Mol., Opt. Phys.* **2012**, *85*, 012517.
- Paier, J.; Ren, X.; Rinke, P.; Scuseria, G. E.; Grüneis, A.; Kresse, G.; Scheffler, M. *New J. Phys.* **2012**, *14*, 043002.
- Burow, A. M.; Bates, J. E.; Furche, F.; Eshuis, H. *J. Chem. Theory Comput.* **2014**, *10*, 180–194.
- Waitt, C.; Ferrara, N. M.; Eshuis, H. *J. Chem. Theory Comput.* **2016**, *12*, 5350–5360.
- Harl, J.; Kresse, G. *Phys. Rev. B: Condens. Matter Mater. Phys.* **2008**, *77*, 045136.
- Harl, J.; Schimka, L.; Kresse, G. *Phys. Rev. B: Condens. Matter Mater. Phys.* **2010**, *81*, 115126.
- Del Ben, M.; Hutter, J.; VandeVondele, J. *J. Chem. Theory Comput.* **2013**, *9*, 2654–2671.
- Gould, T.; Dobson, J. F.; Lebegue, S. *Phys. Rev. B: Condens. Matter Mater. Phys.* **2013**, *87*, 165422.
- Kaoui, F.; Rocca, D. *J. Phys.: Condens. Matter* **2016**, *28*, 035201.
- Ren, X.; Rinke, P.; Scheffler, M. *Phys. Rev. B: Condens. Matter Mater. Phys.* **2009**, *80*, 045402.
- Eshuis, H.; Furche, F. *J. Phys. Chem. Lett.* **2011**, *2*, 983–989.
- Olsen, T.; Yan, J.; Mortensen, J. J.; Thygesen, K. S. *Phys. Rev. Lett.* **2011**, *107*, 156401.
- Björkman, T.; Gulans, A.; Krashennnikov, A. V.; Nieminen, R. M. *Phys. Rev. Lett.* **2012**, *108*, 235502.
- Yan, J.; Li, L.; O’Grady, C. *Comput. Phys. Commun.* **2013**, *184*, 2728–2733.
- Karlický, F.; Lazar, P.; Dubecký, M.; Otyepka, M. *J. Chem. Theory Comput.* **2013**, *9*, 3670–3676.
- Kaltak, M.; Klimeš, J.; Kresse, G. *Phys. Rev. B: Condens. Matter Mater. Phys.* **2014**, *90*, 054115.
- Del Ben, M.; Schütt, O.; Wentz, T.; Messmer, P.; Hutter, J.; VandeVondele, J. *Comput. Phys. Commun.* **2015**, *187*, 120–129.
- Rekkedal, J.; Coriani, S.; Iozzi, M. F.; Teale, A. M.; Helgaker, T.; Pedersen, T. B. *J. Chem. Phys.* **2013**, *139*, 081101.
- Kühn, M. *J. Chem. Theory Comput.* **2014**, *10*, 623–633.
- Kaltak, M.; Klimeš, J.; Kresse, G. *J. Chem. Theory Comput.* **2014**, *10*, 2498–2507.
- Moussa, J. E. *J. Chem. Phys.* **2014**, *140*, 014107.
- Kállay, M. *J. Chem. Phys.* **2015**, *142*, 204105.
- Schurkus, H. F.; Ochsenfeld, C. *J. Chem. Phys.* **2016**, *144*, 031101.

- (59) Wilhelm, J.; Seewald, P.; Del Ben, M. D.; Hutter, J. *J. Chem. Theory Comput.* **2016**, *12*, 5851–5859.
- (60) Grüneis, A.; Marsman, M.; Harl, J.; Schimka, L.; Kresse, G. *J. Chem. Phys.* **2009**, *131*, 154115.
- (61) Heßelmann, A. *J. Chem. Phys.* **2011**, *134*, 204107.
- (62) Gould, T. *J. Chem. Phys.* **2012**, *137*, 111101.
- (63) Ren, X.; Rinke, P.; Scuseria, G. E.; Scheffler, M. *Phys. Rev. B: Condens. Matter Mater. Phys.* **2013**, *88*, 035120.
- (64) Bates, J. E.; Furche, F. *J. Chem. Phys.* **2013**, *139*, 171103.
- (65) Maggio, E.; Kresse, G. *Phys. Rev. B: Condens. Matter Mater. Phys.* **2016**, *93*, 235113.
- (66) Bates, J. E.; Laricchia, S.; Ruzsinszky, A. *Phys. Rev. B: Condens. Matter Mater. Phys.* **2016**, *93*, 045119.
- (67) Dion, M.; Rydberg, H.; Schröder, E.; Langreth, D. C.; Lundqvist, B. I. *Phys. Rev. Lett.* **2004**, *92*, 246401.
- (68) Otero-de-la-Roza, A.; Johnson, E. R. *J. Chem. Phys.* **2012**, *137*, 054103.
- (69) Tkatchenko, A. *Adv. Funct. Mater.* **2015**, *25*, 2054–2061.
- (70) Grimme, S.; Antony, J.; Ehrlich, S.; Krieg, H. *J. Chem. Phys.* **2010**, *132*, 154104.
- (71) Perdew, J.; Schmidt, K. In *Density Functional Theory and Its Application to Materials*; Doren, V. V., Alsenoy, C. V., Geerlings, P., Eds.; AIP Conference Proceedings; AIP: Melville, NY, 2001; Vol. 577, pp 1–20.
- (72) Scuseria, G. E.; Henderson, T. M.; Sorensen, D. C. *J. Chem. Phys.* **2008**, *129*, 231101.
- (73) Eshuis, H.; Yarkony, J.; Furche, F. *J. Chem. Phys.* **2010**, *132*, 234114.
- (74) Ren, X.; Rinke, P.; Blum, V.; Wieferink, J.; Tkatchenko, A.; Sanfilippo, A.; Reuter, K.; Scheffler, M. *New J. Phys.* **2012**, *14*, 053020.
- (75) Halkier, A.; Helgaker, T.; Jørgensen, P.; Klopper, W.; Koch, H.; Olsen, J.; Wilson, A. K. *Chem. Phys. Lett.* **1998**, *286*, 243–252.
- (76) Ten-no, S.; Noga, J. *WIREs Comput. Mol. Sci.* **2012**, *2*, 114–125.
- (77) Kong, L.; Bischoff, F. A.; Valeev, E. F. *Chem. Rev.* **2012**, *112*, 75–107.
- (78) Hättig, C.; Klopper, W.; Köhn, A.; Tew, D. P. *Chem. Rev.* **2012**, *112*, 4–74.
- (79) Hehn, A.-S.; Klopper, W. *J. Chem. Phys.* **2013**, *138*, 181104.
- (80) Hehn, A.-S.; Tew, D. P.; Klopper, W. *J. Chem. Phys.* **2015**, *142*, 194106.
- (81) Marini, A.; García-González, P.; Rubio, A. *Phys. Rev. Lett.* **2006**, *96*, 136404.
- (82) Lu, D.; Li, Y.; Rocca, D.; Galli, G. *Phys. Rev. Lett.* **2009**, *102*, 206411.
- (83) Nguyen, H.-V.; de Gironcoli, S. *Phys. Rev. B: Condens. Matter Mater. Phys.* **2009**, *79*, 205114.
- (84) Ihrig, A. C.; Wieferink, J.; Zhang, I. Y.; Ropo, M.; Ren, X.; Rinke, P.; Scheffler, M.; Blum, V. *New J. Phys.* **2015**, *17*, 093020.
- (85) Whitten, J. L. *J. Chem. Phys.* **1973**, *58*, 4496–4501.
- (86) Baerends, E. J.; Ellis, D. E.; Ros, P. *Chem. Phys.* **1973**, *2*, 41–51.
- (87) Dunlap, B. I.; Connolly, J. W. D.; Sabin, J. R. *J. Chem. Phys.* **1979**, *71*, 3396–3402.
- (88) Vahtras, O.; Almlöf, J.; Feyereisen, M. *Chem. Phys. Lett.* **1993**, *213*, 514–518.
- (89) Feyereisen, M.; Fitzgerald, G.; Komornicki, A. *Chem. Phys. Lett.* **1993**, *208*, 359–363.
- (90) Rendell, A. P.; Lee, T. J. *J. Chem. Phys.* **1994**, *101*, 400–408.
- (91) Burow, A. M.; Sierka, M.; Mohamed, F. *J. Chem. Phys.* **2009**, *131*, 214101.
- (92) Maschio, L.; Usvyat, D.; Manby, F. R.; Casassa, S.; Pisani, C.; Schütz, M. *Phys. Rev. B: Condens. Matter Mater. Phys.* **2007**, *76*, 075101.
- (93) Mintmire, J. W.; Sabin, J. R. *Int. J. Quantum Chem.* **1980**, *18*, 707–713.
- (94) Mintmire, J. W.; Sabin, J. R.; Trickey, S. B. *Phys. Rev. B: Condens. Matter Mater. Phys.* **1982**, *26*, 1743–1753.
- (95) Dunlap, B. I.; Rösch, N.; Trickey, S. B. *Mol. Phys.* **2010**, *108*, 3167–3180.
- (96) Jaffe, J. E.; Hess, A. C. *J. Chem. Phys.* **1996**, *105*, 10983–10998.
- (97) Maschio, L.; Usvyat, D. *Phys. Rev. B: Condens. Matter Mater. Phys.* **2008**, *78*, 073102.
- (98) Lorenz, M.; Usvyat, D.; Schütz, M. *J. Chem. Phys.* **2011**, *134*, 094101.
- (99) Varga, Š. *J. Chem. Phys.* **2007**, *127*, 114108.
- (100) Kudin, K. N.; Scuseria, G. E. *J. Chem. Phys.* **2004**, *121*, 2886–2890.
- (101) Ullrich, C.-A. *Time-Dependent Density-Functional Theory—Concepts and Applications*; Oxford University Press: Oxford, 2012.
- (102) Akritas, A. G.; Akritas, E. K.; Malaschonok, G. I. *Math. Comput. Simul.* **1996**, *42*, 585–593.
- (103) Linderberg, J.; Öhrn, Y. *Propagators in Quantum Chemistry*, 2nd ed.; John Wiley & Sons: Hoboken, NJ, 2004.
- (104) van Setten, M. J.; Weigend, F.; Evers, F. *J. Chem. Theory Comput.* **2013**, *9*, 232–246.
- (105) Ashcroft, N. W.; Mermin, N. D. *Solid State Physics*; Thomson Learning, 1976; Chapter 8.
- (106) Pisani, C.; Dovesi, R. *Int. J. Quantum Chem.* **1980**, *17*, 501–516.
- (107) Sun, J.; Bartlett, R. J. *J. Chem. Phys.* **1996**, *104*, 8553–8565.
- (108) Ashcroft, N. W.; Mermin, N. D. *Solid State Physics*; Thomson Learning, 1976; Chapter F.
- (109) Casida, M. E. In *Recent Advances in Density Functional Methods, Part I*; Chong, D. P., Ed.; Recent Advances in Computational Chemistry; World Scientific Publishing, 1995; Vol. 1, pp 155–192.
- (110) Hirata, S.; Head-Gordon, M.; Bartlett, R. J. *J. Chem. Phys.* **1999**, *111*, 10774–10786.
- (111) Stolarczyk, L. Z.; Piela, L. *Int. J. Quantum Chem.* **1982**, *22*, 911–927.
- (112) Łazarski, R.; Burow, A. M.; Sierka, M. *J. Chem. Theory Comput.* **2015**, *11*, 3029–3041.
- (113) TURBOMOLE V7.1 2016, a development of University of Karlsruhe and Forschungszentrum Karlsruhe GmbH, 1989–2007, and TURBOMOLE GmbH, since 2007; <http://www.turbomole.com>.
- (114) Häser, M.; Almlöf, J. *J. Chem. Phys.* **1992**, *96*, 489–494.
- (115) Doser, B.; Lambrecht, D. S.; Kussmann, J.; Ochsenfeld, C. *J. Chem. Phys.* **2009**, *130*, 064107.
- (116) Peintinger, M. F.; Oliveira, D. V.; Bredow, T. *J. Comput. Chem.* **2013**, *34*, 451–459.
- (117) Grüneis, A.; Heß, B. A. *Theor. Chem. Acc.* **1998**, *100*, 253–263.
- (118) Kresse, G.; Furthmüller, J. *Comput. Mater. Sci.* **1996**, *6*, 15–50.
- (119) Blöchl, P. E. *Phys. Rev. B: Condens. Matter Mater. Phys.* **1994**, *50*, 17953–17979.
- (120) Blöchl, P. E. *J. Chem. Phys.* **1995**, *103*, 7422–7428.
- (121) Møller, C.; Plesset, M. S. *Phys. Rev.* **1934**, *46*, 618.
- (122) Perdew, J. P.; Burke, K.; Ernzerhof, M. *Phys. Rev. Lett.* **1996**, *77*, 3865–3868.
- (123) Weigend, F.; Häser, M.; Patzelt, H.; Ahlrichs, R. *Chem. Phys. Lett.* **1998**, *294*, 143–152.
- (124) Schäfer, A.; Huber, C.; Ahlrichs, R. *J. Chem. Phys.* **1994**, *100*, 5829–5835.
- (125) Rappoport, D.; Furche, F. *J. Chem. Phys.* **2010**, *133*, 134105.
- (126) Dunning, T. H., Jr. *J. Chem. Phys.* **1989**, *90*, 1007–1023.
- (127) Kendall, R. A.; Dunning, T. H., Jr.; Harrison, R. J. *J. Chem. Phys.* **1992**, *96*, 6796–6806.
- (128) Eichkorn, K.; Weigend, F.; Treutler, O.; Ahlrichs, R. *Theor. Chem. Acc.* **1997**, *97*, 119–124.
- (129) Weigend, F. *Phys. Chem. Chem. Phys.* **2006**, *8*, 1057–1065.
- (130) Hellweg, A.; Hättig, C.; Höfener, S.; Klopper, W. *Theor. Chem. Acc.* **2007**, *117*, 587–597.
- (131) Hättig, C.; Schmitz, G.; Kößmann, J. *Phys. Chem. Chem. Phys.* **2012**, *14*, 6549–6555.
- (132) Burow, A. M.; Sierka, M. *J. Chem. Theory Comput.* **2011**, *7*, 3097–3104.
- (133) Irmiler, A. et al., University of Konstanz, unpublished, 2016.
- (134) Monkhorst, H. J.; Pack, J. D. *Phys. Rev. B* **1976**, *13*, 5188–5192.
- (135) Gauss, J.; Stanton, J. F. *J. Phys. Chem. A* **2000**, *104*, 2865–2868.

- (136) Boys, S. F.; Bernardi, F. *Mol. Phys.* **1973**, *25*, 35–44.
- (137) Řezáč, J.; Hobza, P. *J. Chem. Theory Comput.* **2013**, *9*, 2151–2155.
- (138) Grimme, S. *J. Comput. Chem.* **2006**, *27*, 1787–1799.
- (139) Sinnokrot, M. O.; Sherrill, C. D. *J. Phys. Chem. A* **2004**, *108*, 10200.
- (140) Janowski, T.; Pulay, P. *Chem. Phys. Lett.* **2007**, *447*, 27–32.
- (141) Janowski, T.; Pulay, P. *J. Am. Chem. Soc.* **2012**, *134*, 17520–17525.
- (142) Lebègue, S.; Harl, J.; Gould, T.; Ángyán, J. G.; Kresse, G.; Dobson, J. F. *Phys. Rev. Lett.* **2010**, *105*, 196401.
- (143) Burow, A. M.; Sierka, M.; Döbler, J.; Sauer, J. *J. Chem. Phys.* **2009**, *130*, 174710.
- (144) Euwema, R. N.; Surratt, G. T. *J. Phys. Chem. Solids* **1975**, *36*, 67–71.
- (145) Redlack, A.; Grindlay, J. *J. Phys. Chem. Solids* **1975**, *36*, 73–82.
- (146) Burow, A. M. Methoden zur Beschreibung von chemischen Strukturen beliebiger Dimensionalität mit der Dichtefunktionaltheorie unter periodischen Randbedingungen (Methods for the description of chemical structures of arbitrary dimensionality with the density functional theory under periodic boundary conditions). Ph.D. Thesis, Humboldt-Universität zu Berlin, 2011.
- (147) Challacombe, M.; White, C.; Head-Gordon, M. *J. Chem. Phys.* **1997**, *107*, 10131–10140.
- (148) Sierka, M.; Hogekamp, A.; Ahlrichs, R. *J. Chem. Phys.* **2003**, *118*, 9136–9148.
- (149) White, C. A.; Head-Gordon, M. *J. Chem. Phys.* **1994**, *101*, 6593–6605.
- (150) Kudin, K. N.; Scuseria, G. E. *Chem. Phys. Lett.* **1998**, *283*, 61–68.

Supplementary information for 'Random Phase Approximation for Periodic Systems Employing Direct Coulomb Lattice Summation'

```
#methane coordinates in bohr for the 3D cubic cell and cell
↪ parameter a=10 bohr
$cell
 10.0000000000 10.0000000000 10.0000000000 90. 90. 90.
$coord
 5.0000000000000000 5.0000000000000000 5.0000000000000000
↪ c
 5.0000000000000000 5.0000000000000000 7.07191462935715
↪ h
 6.95347604397854 5.0000000000000000 4.30927864226444
↪ h
 4.02331772493165 6.69162236292298 4.30939202583241
↪ h
 4.02339898315536 3.30812063432295 4.30930698815643
↪ h
$end

#benzene coordinates in bohr for the 1D periodic chain and d=6 bohr
$cell
 6.0
$coord
 0.0000000000000000 2.27726048004030 1.31477695116610
↪ c
 0.0000000000000000 0.0000000000000000 2.62955390233230
↪ c
 0.0000000000000000 -2.27726048004030 1.31477695116610
↪ c
 0.0000000000000000 -2.27726048004030 -1.31477695116610
↪ c
 0.0000000000000000 0.0000000000000000 -2.62955390233230
↪ c
 0.0000000000000000 2.27726048004030 -1.31477695116610
↪ c
 0.0000000000000000 4.04473537651420 2.33522905843130
↪ h
 0.0000000000000000 0.0000000000000000 4.67045811686260
↪ h
```

```
0.0000000000000000 -4.04473537651420 2.33522905843130
↪ h
0.0000000000000000 -4.04473537651420 -2.33522905843130
↪ h
0.0000000000000000 0.0000000000000000 -4.67045811686260
↪ h
0.0000000000000000 4.04473537651420 -2.33522905843130
↪ h
$end

#naphthalene coordinates in bohr for the 1D periodic chain and d=6
↪ bohr
$cell
6.0
$coord
0.0000000000000000 4.60200356035142 1.33767554986132
↪ c
0.0000000000000000 4.60200356035142 -1.33767554986132
↪ c
0.0000000000000000 2.35125643289747 -2.65180941166365
↪ c
0.0000000000000000 0.0000000000000000 -1.35771086264751
↪ c
0.0000000000000000 0.0000000000000000 1.35771086264751
↪ c
0.0000000000000000 2.35125643289747 2.65180941166365
↪ c
0.0000000000000000 -2.35125643289747 2.65180941166365
↪ c
0.0000000000000000 -4.60200356035142 1.33767554986132
↪ c
0.0000000000000000 -4.60200356035142 -1.33767554986132
↪ c
0.0000000000000000 -2.35125643289747 -2.65180941166365
↪ c
0.0000000000000000 6.39458306443460 2.35792746179659
↪ h
0.0000000000000000 6.39458306443460 -2.35792746179659
↪ h
```

0.0000000000000000	2.34633678839078	-4.71676640487692
↔ h		
0.0000000000000000	2.34633678839078	4.71676640487692
↔ h		
0.0000000000000000	-2.34633678839078	4.71676640487692
↔ h		
0.0000000000000000	-6.39458306443460	2.35792746179659
↔ h		
0.0000000000000000	-6.39458306443460	-2.35792746179659
↔ h		
0.0000000000000000	-2.34633678839078	-4.71676640487692
↔ h		





\$end

ARTICLE

DOI: 10.1038/s41467-018-04979-y

OPEN

Topochemical conversion of an imine- into a thiazole-linked covalent organic framework enabling real structure analysis

Frederik Haase ^{1,2}, Erik Troschke³, Gökçen Savasci ^{1,2}, Tanmay Banerjee ¹, Viola Duppel¹, Susanne Dörfler⁴, Martin M.J. Grunde², Asbjörn M. Burow², Christian Ochsenfeld², Stefan Kaskel^{3,4} & Bettina V. Lotsch ^{1,2}

Stabilization of covalent organic frameworks (COFs) by post-synthetic locking strategies is a powerful tool to push the limits of COF utilization, which are imposed by the reversible COF linkage. Here we introduce a sulfur-assisted chemical conversion of a two-dimensional imine-linked COF into a thiazole-linked COF, with full retention of crystallinity and porosity. This post-synthetic modification entails significantly enhanced chemical and electron beam stability, enabling investigation of the real framework structure at a high level of detail. An in-depth study by electron diffraction and transmission electron microscopy reveals a myriad of previously unknown or unverified structural features such as grain boundaries and edge dislocations, which are likely generic to the in-plane structure of 2D COFs. The visualization of such real structural features is key to understand, design and control structure–property relationships in COFs, which can have major implications for adsorption, catalytic, and transport properties of such crystalline porous polymers.

¹Max Planck Institute for Solid State Research, Heisenbergstraße 1, 70569 Stuttgart, Germany. ²Department of Chemistry, Ludwig-Maximilians-Universität München, Butenandtstr. 5-13, 81377 Munich, Germany. ³Department of Inorganic Chemistry 1, TU Dresden, Bergstraße 66, 01069 Dresden, Germany. ⁴Fraunhofer Institute for Material and Beam Technology (IWS), Winterbergstr. 28, 01277 Dresden, Germany. Correspondence and requests for materials should be addressed to B.V.L. (email: b.lotsch@fkf.mpg.de)

Covalent organic frameworks (COFs) distinguish themselves from conventional polymers by three defining features: covalent connectivity, porosity, and crystallinity. This generation of two- (2D) and three-dimensional (3D) polymers is synthesized under solvothermal conditions by reversible covalent bond forming reactions^{1–3}. Reversibility of the COF linkage is key to obtain ordered materials by error correction and defect healing^{4–6}, but at the same time makes COFs inherently unstable and rich in defects. This dilemma can be circumvented by performing a reversible order-inducing step under thermodynamic control and subsequently arresting this order via a post-synthetic treatment, a concept that has been explored for the synthesis of crystalline, “unfeasible” zeolites⁷ as well as to stabilize the molecular cages formed by dynamic covalent chemistry⁸. In order to arrest COFs in their crystalline state (arrested linkage COFs: ALCOFs) the chemical linkage of the COF needs to be converted² from a reversible to an irreversible type of bond in a topochemical fashion.

The competition between reversibility and stability, which is dominated by subtle changes in the reaction conditions, often leads to COFs with only moderate chemical stability and low crystallinity. As a result, nanocrystalline COFs with ubiquitous structural disorder are obtained. Such structural disorder is difficult to probe or even quantify by conventional diffraction methods such as X-ray powder diffraction (XRPD), while imaging with transmission electron microscopy (TEM) is difficult due to the sensitivity of COFs – similar to most soft matter systems – to the electron beam in comparison to inorganic crystalline materials^{1,4,9}. In spite of these challenges, analysis of the ideal and real structure of COFs has been in the focus since the very beginning of the field, and it continues to attract attention as the field^{1,4,9–12}.

In 2D COFs, various kinds of out-of-plane disorder are prevalent, such as random or poorly defined stacking sequences^{4,13,14}. In-plane defects, which also impact the electronic transport properties of COFs, have been invoked to explain the low crystallinity of many COFs¹⁵. In closely related systems such as on-surface grown, monolayer 2D polymers, rings with five or seven edges in an otherwise hexagonal system have been observed as defects by scanning tunneling microscopy^{16,17}, very similar to the formation of defects in graphene¹⁸. While often detrimental, such defects can be highly beneficial, for example in (electro) catalysis where they act as high-energy binding sites for the adsorption of reaction intermediates¹⁹. In addition, the typically limited size of the crystallites of COFs leads to grain boundaries and domain intergrowth, which can drastically influence the long-range charge carrier percolation in COFs²⁰ as well as influence ion conduction^{21,22}. These examples show that disorder can have a significant influence on the chemical, structural and (opto-)electronic properties of COFs. However, such defects were never directly imaged. Hence, it is of paramount importance to understand the types of defects and disorder present in COFs and to elucidate and control their influence on the properties of the material.

In this work, we investigate the topochemical conversion of the triphenyl triazine imine COF (TTI-COF)^{4,23} with elemental sulfur into a thiazole-linked COF through a post-synthetic locking strategy, thereby establishing a class of thiazole-based COFs. This type of post-synthetic modification is fundamentally different from previous examples, such as the introduction of functionalities by tethering side groups²⁴ or heterogeneous linker exchange.²⁵ These approaches either do not change the reversible bond of the starting COFs, or they even utilize the reversibility to introduce functionality. The post-synthetic oxidation of an imine COF linkage to an amide, as reported recently, provides a direct transformation of the reversible bond of the COF,² however it

was recently shown that even amides are, in principle, reversible enough to be used for the synthesis of COFs²⁶. Modification of the imine linkage of the TTI-COF leads to excellent contrast and high electron beam stability of the sulfur-modified TTI-COF (triphenyl triazine thiazole COF; TTT-COF), which enables imaging and analysis of in-plane defects with TEM, thus revealing details of real structure effects that have not been amenable to direct observation in any COF so far.

Results

Post-synthetic locking by imine to thiazole conversion. As pointed out by Yaghi et al.,² the promise of COFs lies in the fact that COFs, though being extended solids, are amenable to the versatile toolbox of molecular synthesis. While this concept is particularly useful at the precursor level and hence formation of COFs, strategies for modifying the backbone of COFs once they are formed are extremely scarce². We thus explored the post-synthetic reaction of COFs with elemental sulfur. At high temperatures, elemental sulfur reacts with aromatic imines to first oxidize the imine to a thioamide, and subsequently oxidatively cyclizes the thioamide group to form a thiazole ring (Fig. 1)²⁷. Thus, sulfur serves as an oxidant (being reduced to H₂S) and as a nucleophile, attaching first to the imine carbon and afterwards to the phenyl ring on the nitrogen side of the imine.

Transferring this reaction scheme to imine-linked TTI-COF, which was previously reported by us to show high thermal and chemical stability^{4,23}, we synthesized TTT-COF in two successive steps: First, TTI-COF was infiltrated with molten sulfur at 155 °C. At this temperature, sulfur has minimum viscosity, enabling mixing with the COF material. Subsequently, by using a thermal treatment at higher temperature (350 °C), the conversion of the TTI-COF to the TTT-COF took place. After removal of the excess sulfur by Soxhlet extraction and under high vacuum, the obtained material was investigated by ¹³C and ¹⁵N solid state NMR (ssNMR) to probe the imine to thiazole conversion and retention of the framework structure (Fig. 2).

Framework characterization. As depicted in Fig. 2a, b, the ssNMR spectra of TTT-COF shows significant and well-defined changes as compared to the TTI-COF precursor. The loss of the carbon 3 and 4 signals at 151 ppm and 115 ppm (in TTI-COF) in the ¹³C ssNMR spectra, together with the appearance of the 3' signal at 156 ppm for the TTT-COF, indicate the conversion of the nitrogen bearing phenyl ring to the thiazole in TTT-COF. Small residual intensity at 151 ppm might indicate some unreacted TTI-COF. Furthermore, the characteristic imine carbon 2 is shifted in the thiazole 2' as a shoulder to the triazine carbon 1^{28,29}. Also, the absence of a ¹³C signal between 210 and 180 ppm^{29,30} hints at the conversion of the imine to the thiazole and the absence of thioamide. ¹⁵N ssNMR shows the triazine nitrogen, 6 and 6', at the same position for TTT-COF as for TTI-COF and a shift of the imine nitrogen 5 from –55 ppm to the thiazole 5' at –71 ppm. As additional confirmation of the determined thiazole structure of the TTT-COF, the calculated NMR chemical shifts of excised fragments (Fig. 2a, b, Supplementary Table 1, 2, 3, 4) are in good agreement with the experimental NMR spectra. ¹³C and ¹⁵N NMR chemical shifts were calculated with density functional theory (DFT) on the B97-2/3/pcS-2//PBE-D3/def2-TZVP level of theory (Supplementary Figs. 1, 2, 3, 4, 5), as we already applied this method successfully to other COF building blocks³¹.

The Fourier-transform infrared spectroscopy (FT-IR) spectra further confirm the conversion of TTI-COF to TTT-COF, as evident by the disappearance of the characteristic imine (N=C) vibration at 1627 cm⁻¹ and the appearance of a new N=C

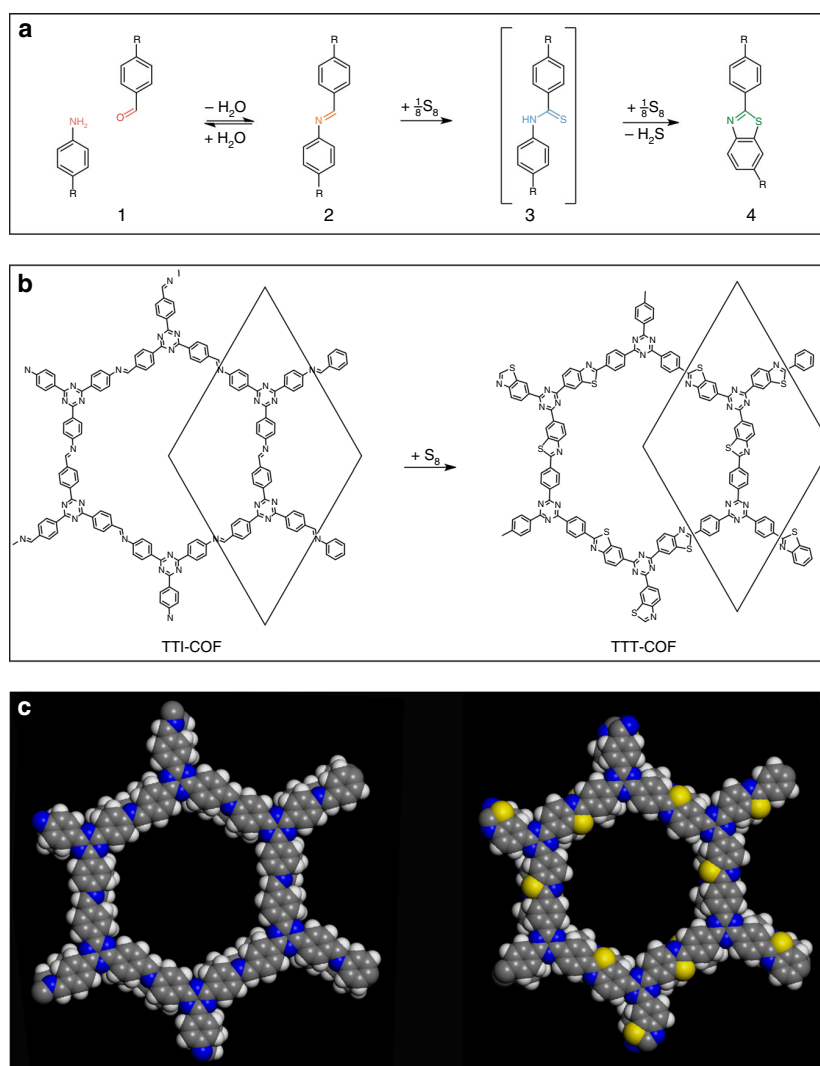


Fig. 1 Schematic of the imine to thiazole transformation in the TTI-COF. **a** Schematic of the reaction of an amine and an aldehyde (1) to form an imine (2), then a thioamide as an intermediate (3) by the action of elemental sulfur, and finally a thiazole (4). **b** Schematic drawing of the sulfuration reaction of the TTI-COF to form the thiazole-based TTT-COF. **c** Space filling model of one pore of the TTI-COF (left) and the TTT-COF (right)

vibration²⁸ of the thiazole at 1609 cm^{-1} (Fig. 2d, Supplementary Fig. 8). Elemental analysis shows the presence of sulfur with an elemental composition close to the composition that would be expected from the thiazole model (Supplementary Table 5). In addition, energy dispersive X-ray spectroscopy scanning electron microscopy (EDX/SEM; Supplementary Fig. 10) of TTT-COF indicates homogeneous distribution of sulfur in all parts of the sample, thus verifying a uniform and regular incorporation of sulfur in the COF backbone. The XRPD confirms the complete absence of reflections originating from elemental sulfur, further validating that only chemically bound sulfur is present (Supplementary Fig. 16).

Sorption analysis reveals retention of the porosity of the TTT-COF after sulfuration (Fig. 2e), the Brunauer–Emmett–Teller (BET) surface area of $1431\text{ m}^2\text{ g}^{-1}$ for the TTT-COF (theoretical surface area $1609\text{ m}^2\text{ g}^{-1}$) being close to the BET surface area of $1362\text{ m}^2\text{ g}^{-1}$ for the precursor TTI-COF (theoretical surface area $1970\text{ m}^2\text{ g}^{-1}$) (Supplementary Fig. 11). The ratio of experimental BET to theoretical surface area is seen to be improved upon sulfur incorporation. This not only indicates that the pores have not been blocked by sulfur deposits, but also that previously blocked

pores might have been cleaned by oxidative or evaporative removal of guests in the pores. The pore size distribution was calculated from Argon isotherms using the quenched solid state functional theory (QSDFT) cylindrical pore model, which shows a reduction in the pore size from 2.3 nm in the TTI-COF to 2.2 nm in the TTT-COF (Supplementary Fig. 12). This change in the pore size matches well with the reduction in lattice parameters observed in the XRPD and the expected pore size reduction by the bending of the linkers upon formation of the thiazole.

Structural analysis of TTI-COF and TTT-COF. The structure and crystallinity of TTT-COF was then assessed with XRPD, revealing a crystalline material with a hexagonal unit cell ($P6_3/m$) and a higher symmetry than derived for the precursor TTI-COF ($P1$) (Supplementary Fig. 13)⁴. However, TTT-COF is quite similar to the randomly stacked TTI-COF (*rs*-TTI-COF, $P6_3/m$) (Fig. 3a), which is identical to the TTI-COF in terms of molecular connectivity, but shows random orientation of the stacking vector of the layers due to the altered synthesis conditions (see Methods section), and hence a higher apparent symmetry⁴. TTT-COF has

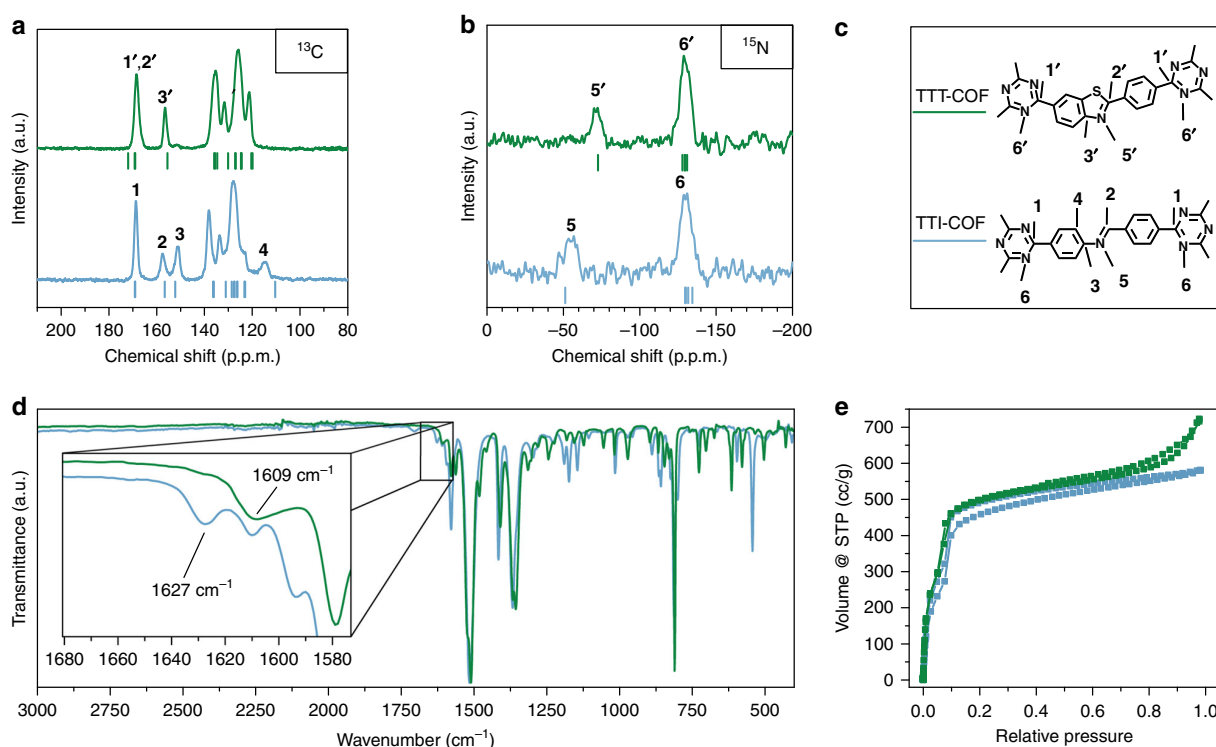


Fig. 2 Characterization of the TTI-COF (blue) and TTT-COF (green). **a** ^{13}C ssNMR demonstrating the conversion of the imine linkage to the corresponding thiazole. **b** ^{15}N ssNMR showing a shift in the imine nitrogen position (**5** \rightarrow **5'**). Calculated $\Delta\delta$ values for the TTT and TTI-COF on B97-2/pcS-2 level of theory are shown as red and black dashes, respectively. **c** Assignment of the ^{13}C and the ^{15}N ssNMR signals to the respective ^{13}C and ^{15}N nuclei in the structures. **d** FT-IR spectra of TTI-COF (black) and TTT-COF (red). The inset shows an enlargement of the region characteristic for $\text{N}=\text{C}$ vibrations. **e** Argon sorption isotherms of TTI-COF and TTT-COF showing retention of porosity

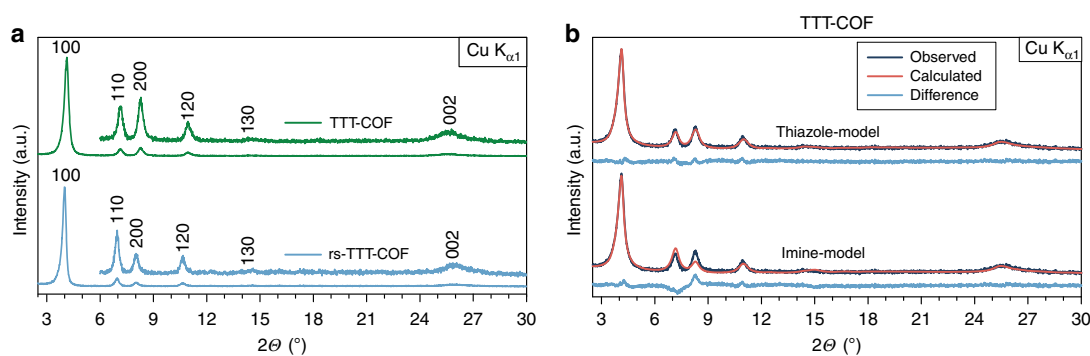


Fig. 3 XRPD and modeling of the TTI- and TTT-COF. **a** XRPD patterns of the rs-TTI-COF and the TTT-COF showing retention of crystallinity upon transformation. **b** Comparison of the imine and thiazole models that were applied during Rietveld refinement of the XRPD TTT-COF. The thiazole model (top) shows a better fit than the imine model (bottom)

reduced in-plane unit cell dimensions (24.478(5) Å vs 25.244(8) Å), and a larger interlayer stacking distance ($c = 7.002(5)$ Å) than rs-TTI-COF ($c = 6.905(7)$ Å) as is evident from Rietveld refinement (Supplementary Table 6, Supplementary Fig. 14). The smaller a and b axis of the unit cell can be understood by the contraction induced by bending of the linker upon formation of the five-membered thiazole ring (Supplementary Fig. 15). The larger stacking distance likely stems from the introduction of sulfur into the layers, also signaling a somewhat weaker interlayer interaction. This may explain the loss of the ordered slip-stacking that is present in TTI-COF (Supplementary Fig. 13). Rietveld refinement of the XRPD pattern of TTT-COF was done using an imine model and a thiazole model; a significantly better fit was

obtained for the thiazole model, which further confirms this structural feature in TTT-COF (Fig. 3b, Supplementary Table 7).

Generalizing the imine locking with a pyrene based COF. To demonstrate that the concept of imine to thiazole conversion in COFs can be generalized and transferred also to other COF systems, we performed the reaction on the Pyrene tetra(phenyl) biphenyl imine-COF (PBI-COF, Supplementary Fig. 6)³², which was transformed to the Pyrene tetra(phenyl) biphenyl thiazole-COF (PBT-COF, Supplementary Fig. 6). In the PBI- and PBT-COFs the conversion is clearly evidenced by ^{13}C ssNMR as well, which shows the appearance of two peaks at 153.3 ppm and 166.8

ppm, with the latter corresponding to the characteristic thiazole carbon between the nitrogen and the sulfur (Supplementary Fig. 7). Note that in the TTI- and TTT-COFs, this region is obstructed by the presence of the triazine carbon (1 & 1', Fig. 2a). Similar to the TTI- to TTT-COF conversion, the PBI to PBT-COF conversion is evidenced by the disappearance of the vibration at 1622 cm^{-1} that corresponds to the characteristic imine stretch, and by the presence of a vibration at 1602 cm^{-1} in the PBT-COF that can be assigned to the thiazole moiety (Supplementary Fig. 9).

As in the TTI-to-TTT transformation, crystallinity was retained during the transformation of the PBI- to PBT-COF (Supplementary Fig. 17), while the in-plane lattice parameters a and b of the Rietveld-refined structures differ less between PBI- and PBT-COF (Supplementary Table 8) as compared to the TTI- and TTT-COF (0.60 Å and 1.58 Å for the PB and the TT system, respectively). This effect is attributed to the lower degree of structural distortion during the sulfurization reaction, as seen in Supplementary Fig. 18.

Chemical stability screening. As the transformation of the imine-based TTI-COF to the thiazole-based TTT-COF is expected to significantly improve the chemical stability, we assessed the possibility of locking the reversible bond by comparing the crystallinity before and after chemical treatment. Both materials were exposed to identical and extremely harsh conditions, to test the limits of stability of both COFs (Fig. 4). Initially both COFs were treated with concentrated hydrochloric acid, after which both COFs showed no signs of degradation, testifying to the already excellent resistance to acids of TTI-COF. In contrast, other imine-based COFs have previously been reported to be labile under strongly acidic conditions². The treatment of TTI-COF with potassium hydroxide solution lead to a near complete loss of crystallinity, while the TTT-COF remained unaffected. Next, we tested reagents that are known to alter imine bonds: hydrazine is a particularly good nucleophile that enters the imine bond and replaces the amine, which then leads to a loss of order; sodium borohydride, a reagent that is used to reduce imine bonds could lead to a loss of rigidity, followed by a collapse of the structural order. In both cases the TTT-COF remains essentially unaffected, while the TTI-COF turns completely amorphous. This

result shows that the imine bond has been locked as a thiazole, while the ordered structure of the TTT-COF is retained. The resilience of the TTT-COF to reactive conditions and reagents could enable a range of applications that were previously not accessible due to the lability of COFs.

Real structure and defect analysis by TEM. TEM investigations in COFs have so far primarily been used to confirm the periodic structure of COFs^{4,11,23,33,34}, their nano- and micron-scale morphology¹², and the presence of inorganic guests^{33,35}. However, the low contrast in COFs and their low electron beam stability generally render a detailed analysis of COFs with TEM highly challenging as the samples easily decompose before useful information can be extracted. The destruction of COFs in the electron beam can be ascribed to different damaging mechanisms: one of the defining features of COFs is their composition out of light elements, which makes them difficult to image since such atoms can be significantly affected by atom displacement, electron-beam sputtering, electron-beam heating, electrostatic charging, and radiolysis³⁶.

The TTI- and TTT-COF were analyzed by electron microscopy, where TEM and SEM revealed a morphology of intergrown crystallites with a slightly anisotropic shape in both COFs (Supplementary Fig. 19). Imaging TTI- and TTT-COF by TEM suggests significantly increased electron contrast for TTT-COF and improved electron beam stability as compared to TTI-COF and other COFs^{4,33}. First, we quantified the stability of the TTI- and the TTT-COF in the electron beam by taking images at defined time intervals, under otherwise identical conditions. Visual inspection of the images revealed gradual decomposition of the TTI-COF upon electron beam exposure as evident by shrinking of the structure as well as diminished lattice fringes (Supplementary Fig. 20). Quantitative analysis of these images by means of their fast Fourier transform (FFT) showed a continued broadening and shift to smaller d -spacings for the peak corresponding to the 100 reflection in the XRPD. The continuous shift in d -spacing can be fitted by an exponential decay from which half-lives can be extracted. TTI-COF has an average half-life of 1.22 min, while TTT-COF displays a significantly increased half-life in the electron beam of 2.83 min (Supplementary Fig. 21), thus clearly pointing to the higher stability of TTT-COF in the electron beam (Fig. 5). While the higher electron contrast in the TEM images of the TTT-COF results from the regular incorporation of sulfur into the lattice, the improved stabilization is likely due to the aromatization of the imine bond in the form of a thiazole and the lower number of hydrogen atoms in the structure, which are most susceptible to electron beam damage³⁶. This improved stability is crucial for exploring the real structure of the TTT-COF with TEM as described in the following.

TEM images of TTT-COF reveal an overall retention of the crystallite size compared to the precursor TTI-COF (50–200 nm); likewise, the crystallinity seen already for the TTI-COF is clearly retained as well⁴. The hexagonal symmetry of the structure is visible from the real space images (along the [001] zone axis, Fig. 6a), which also show the presence of continuous pore channels when viewed along $[hk0]$ (Fig. 6b). Both real space images and selected area electron diffraction (SAED) patterns (Fig. 6c) are in agreement with the structural model developed with Rietveld refinement (see also Supplementary Figs. 22, 23, 24).

In addition, TEM reveals a host of real structure details of TTT-COF, including many forms of defects such as disorder, twin, and grain boundaries. Several observed grains of the COF have co-aligned c -axes but are rotated against each other in the ab -plane (Fig. 6d). Two main types of boundaries are visible

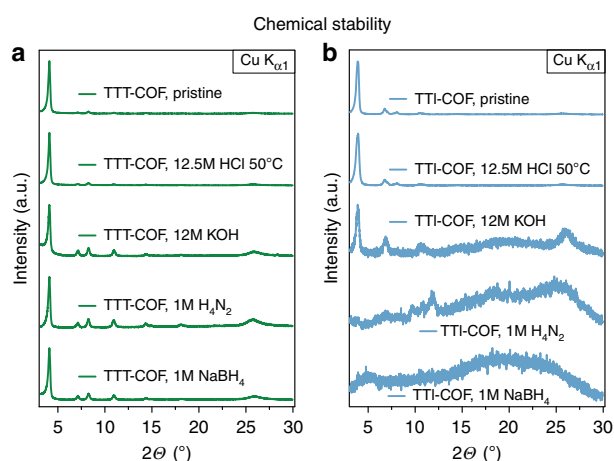


Fig. 4 Chemical stability tests of the TTI- and TTT-COFs. Stability is judged by the crystallinity of the frameworks after exposure to various aggressive chemicals. The TTI- and TTT-COF samples were each exposed to identical conditions for 16 h, which showed a substantially higher stability of the TTT-COF (a) against reactive conditions than the corresponding TTI-COF (b)

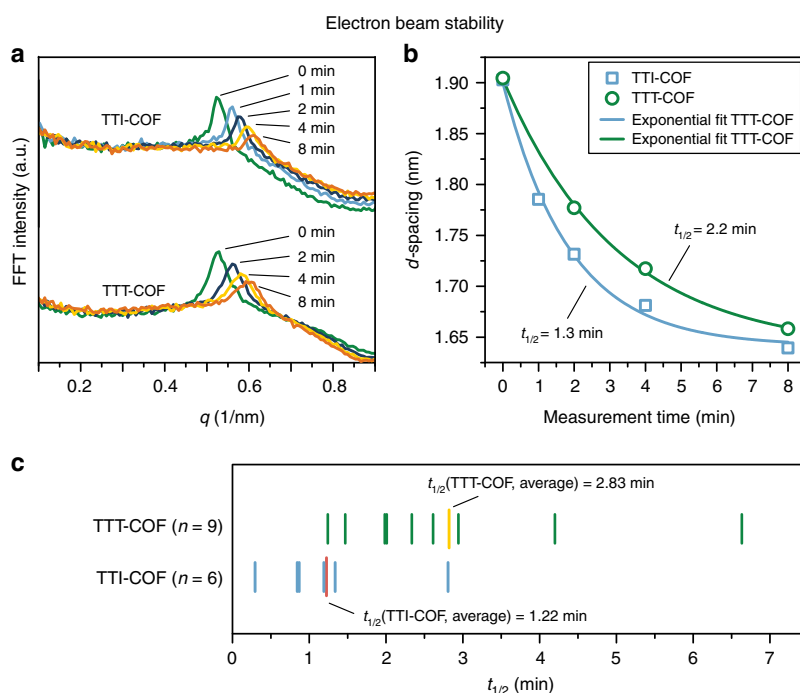


Fig. 5 Electron beam stability tests of the TTI- and TTT-COFs. **a** Electron beam damage seen by the broadening and a shift of the peak in the FFT, corresponding to the 100 reflection in XRPD, of TEM images taken after different exposure times. **b** Plotting the exposure time against the peak shift in the FFT shows a decay that can be fitted with an exponential (fit parameters shown in Supplementary Table 10). **c** Several sets of images were analyzed this way and the results are depicted graphically for better comparison. The average half-life of each system reveals the higher stability of the TTT-COF as compared to TTI-COF

between grains: high angle grain boundaries (HAGB) and low angle grain boundaries (LAGB). HAGB are formed by a corrugated interface of adjacent five and seven membered rings in contrast to the normal six membered rings in the ordered TTT-COF, as shown in Fig. 6f. Some crystallites have an angle of 29° between them, previously observed by TEM in covalently connected grain boundaries of single-layer graphene showing quilt-like structures³⁷, similar to the co-aligned crystallites of TTT-COF. It was not possible to discern unambiguously whether a covalent interface exists between the grains due to increased radiation damage at higher magnifications. However, having this many different crystallites in such an oriented way and intimate contact between the different domains suggests an alignment of these domains during synthesis, which is likely induced by covalent connections.

Discussion

A likely mechanism for the formation of the observed grain boundaries is the crystallization of grains from an initially amorphous imine gel (Fig. 7) as has been proposed as a formation mechanism for imine COFs by Dichtel and coworkers³⁸. This mechanism implies that the covalent connectivity between the different grains is present from the initial formation of the polymer on and that the grain boundary is left as a remnant of this amorphous state.

The intergrowth is even more likely for LAGB as these present a nearly continuous transition from one crystallite to another. Inspection of the LAGB with different Fourier filters shows the presence of several edge dislocations (Fig. 6h–k). Details of such an edge dislocation with a Burgers vector of [100] are shown in Fig. 6l–o. At the molecular level, such a defect could be described by either a linker vacancy (Fig. 6p–q, and supplementary discussion) or an out-of-plane growth that resembles five- and

seven-membered rings such as spirals. Features such as five membered rings and the growth of spirals have similarly been described in the simulation of the crystallization of COF-5, thus predicting the presence of these features in a COF, which have been observed here³⁹.

The observed defects in TTT-COF might have important implications for the properties of the COF. The grain boundaries of the co-aligned crystallites would not obstruct the pore channels and therefore are not expected to influence properties that are primarily contingent on the porous nature of COFs, such as their use as a sorption material or membranes where continuous mass transport is important. The electronic or excitonic conductivity in COFs is assumed to require ordered π -stacking for charge carrier percolation perpendicular to the layers¹⁵, while the transport of charges is also possible within the *ab*-plane of the individual layers⁴⁰. In the latter case the covalent connection and co-alignment of the COF layers could still enable charge transport from one grain to another, rendering limitations through reduced grain boundary conductivity less severe. The presence of defects extending beyond one layer such as out-of-plane helices would essentially turn the 2D COF into a covalently connected 3D COF (Supplementary Fig. 26). This could have important implications for the feasibility of exfoliation of nominal 2D COFs, as covalent bonds would need to be broken in order to separate the individual “layers” of the COF. The presence of an isolated vacancy or a columnar vacancy line defect in the COF structure would influence not only the sorption properties of the COF by the presence of differently sized pores, but it would also present functional groups exposed to larger than regular pores in the COF. Furthermore, we note that size-selective properties such as sorption and catalysis⁴¹ would be influenced in terms of selectivity by the presence of defects, again emphasizing the importance of real structure effects for the properties of COFs.

The reaction of the TTI-COF with sulfur proceeds under conditions that should not allow opening of the imine bonds; the reaction is performed in neat sulfur and no water is present. Furthermore, special solvent mixtures are required to form a

porous crystalline COF while reversible bonds are formed and broken. Since these conditions are not met during the sulfurization reaction described, the formation of TTT-COF has to happen in a topochemical fashion with minimal structural disruption of

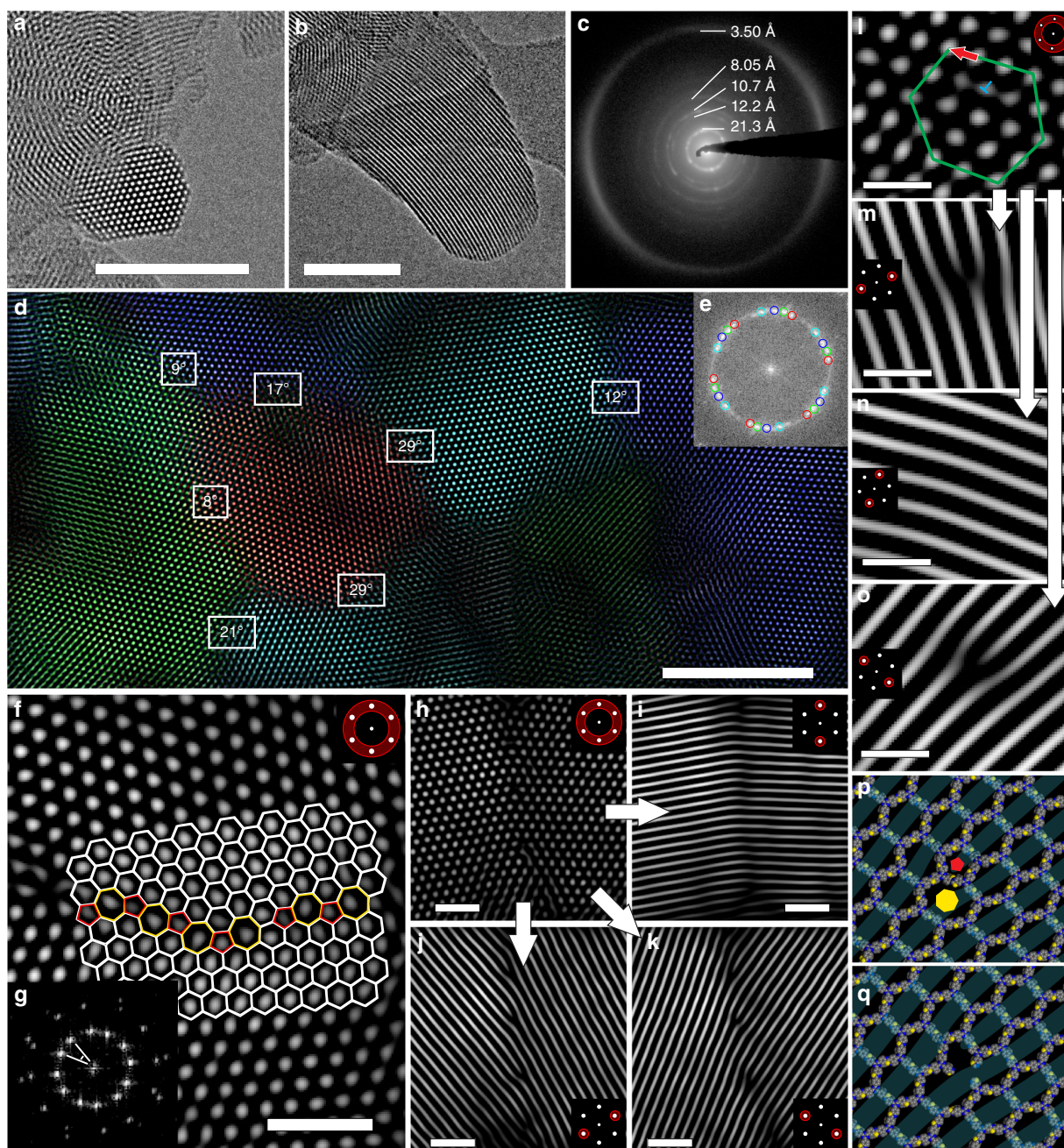


Fig. 6 TEM images and TEM analysis of TTT-COF. FFT filters applied to the image are indicated by a schematic inset. **a, b** Individual crystallites in different orientations. **c** SAED with logarithmic contrast showing diffraction rings, which are in agreement with the XRPD pattern. **d** Multiple inter-grown grains visible by TEM. Indicated angles show the relative orientation of neighboring crystallites. Color overlay indicating the individual grains generated by applying selective hexagonal Fourier filtration (**e**). **f** High angle grain boundary of crystallites with co-aligned *c* direction with an overlay indicating the interface consisting of five, six and seven membered rings. **g** FFT of image **f**. **h–k** Low angle grain boundary with different Fourier filters applied, visualizing the starting points of edge dislocations. **l** Close-up of the start of an edge dislocation. The beginning of the edge dislocation is indicated by the blue **T**, the Burgers vector (red arrow) is determined from the green hexagon to be [100]. **m–o** Visualization of the edge dislocation position from image **l** with different Fourier filters. **p, q** Modeling of an edge dislocation in Materials Studio utilizing a screw dislocation along the pentagonal (red pentagon) and the heptagonal channel (yellow heptagon) (**p**) and the edge dislocation visualized as a channel linker vacancy (**q**). Scale bars: **a, b, d**: 50 nm; **f, h–k**: 10 nm; **l–o**: 5 nm

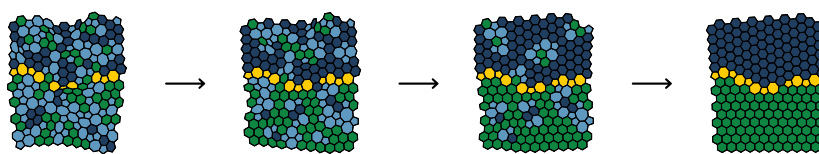


Fig. 7 Schematic of the proposed grain boundary formation mechanism. An initially amorphous gel slowly crystallizes to form the interface between two grains, which implies covalent connectivity between grains as a remnant of the amorphous state

the covalent molecular backbone and the retention of the hexagonal structure of the material. While oxidative conditions during the thiazole formation might cause the scission of the covalent backbone, it cannot explain the presence of the observed defects such as grain boundaries and edge dislocations. We thus note that the observed defects in TTT-COF have to be present already in TTI-COF and likely in other COFs as well, especially 2D COFs based on the same topology.

In summary, the reaction of an imine COF with elemental sulfur leads to the topochemical formation of aromatic thiazole moieties as a robust linkage group, which causes a change in the symmetry of the COF crystal, but not of its topology or its connectivity. This reaction therefore adds to the synthetic toolbox of post-synthetic locking of COFs, which helps to circumvent the inherent limitations imposed by the presence of reversible bonds. The effect of this locking strategy was exemplified by the significantly improved chemical stability of the resulting thiazole COF. In addition, sulfur-assisted generation of thiazoles increases the number of possible COF structures and at the same time opens the door to new COFs with chemical properties not attainable in materials synthesized by reversible reactions.

While crystallinity and porosity of the TTT-COF are fully retained, it shows significantly improved electron contrast compared to the parent COF in addition to improved stability to the electron beam, thus making this system amenable to a study of its real structure by TEM. Close inspection of the structure of the TTT-COF allowed us to extract valuable information on both its long-range and local structure, including the nature of defects and disorder present in the system. While locked in during TTT-COF formation, these defects have been introduced already during the (reversible) synthesis of the precursor TTI-COF and thus can be considered as lasting fingerprints of the COF formation process. In particular, we find prevalent one-dimensional defects such as edge dislocations as well as co-aligned COF grains with grain boundaries that are likely covalently connected. Unraveling the nature of defects in COFs is not only key to better understand their impact on the optical, electronic and catalytic properties of COFs, but also to control and design new COFs by targeting properties imbued by such defects.

Methods

Synthesis. Triazine triphenyl thiazole COF (TTT-COF) and Pyrene tetra(phenyl) biphenyl thiazole (PBT-COF): The respective imine COF was activated under high vacuum at 150 °C and subsequently mixed with the 15-fold amount (by weight) of sulfur in a ball mill. The resulting homogeneous mixture was transferred to a quartz boat in a horizontal tubular furnace and purged at 60 °C under flowing argon. The temperature was increased to 155 °C (60 K h⁻¹ heating rate) and maintained there for 3 h. Subsequently, the temperature was raised to 350 °C (100 K h⁻¹ heating rate) and kept for 3 h. After cooling down, the resulting material was washed via Soxhlet extraction with toluene and THF for 24 h, respectively. The samples were dried at 70 °C in an oven and then at 150 °C under high vacuum.

Randomly stacked Triazine triazine triphenyl imine COF (rs-TTI-COF): TT-CHO (0.0254 mmol, 10.0 mg), TT-NH₂ (0.0254 mmol, 9.01 mg), di(*n*-octyl) phthalate (1 ml), triphenyl phosphate (1 ml), aqueous acetic acid (0.318 mmol, 6 M, 0.053 ml) were added successively to a Biotage® precision glass vial, sealed and heated under autogenous pressure at 120 °C for 72 h. The rs-TTI-COF was worked up in the same manner as TTI-COF.

Chemical stability tests. Chemical stability of the TTI- and TTT-COF was assessed by immersing ~20 mg of the COF in an aqueous solution of each 12.5 M hydrochloric acid (HCl) (50 °C), 12 M potassium hydroxide (KOH), 1 M hydrazine (H₂NNH₂) and 1 M sodium borohydride (NaBH₄) for 16 h at room temperature unless denoted otherwise. Afterwards, the sample was filtered off and washed thoroughly with water, ethanol, THF, chloroform and DCM. After drying at ambient conditions, the crystallinity was assessed by XRPD.

Structure building. The structural models were built successively and based on each other starting from the well defined TTI-COF model⁴. The rs-TTI-COF and the TTT-COF showed no symmetry reduction from a hexagonal to a triclinic unit cell, therefore the highest reasonable symmetry supported by the molecular geometry is *P6₃/m* which was used to build a unit cell model in BIOVIA Materials Studio 2017 (17.1.0.48. Copyright © 2016 Dassault Systèmes). Molecular connectivity was based on geometric considerations and the obtained evidence from FT-IR and ssNMR. The structures and the unit cell was relaxed using force fields (Forcite, universal force fields with Ewald electrostatic and van der Waals summations method). These models were then used to refine the unit cell parameters by Rietveld refinement.

TEM and SAED. TEM was performed with a Philips CM30 ST (300 kV, LaB₆ cathode). The samples were suspended in *n*-butanol and drop-cast onto a lacey carbon film (Plano). Processing of TEM and SAED images was performed with the help of ImageJ 1.47 v.

Stability measurements were performed by taking images of the sample after defined time intervals in-between pictures, relative to the first image ($t = 0$ min).

XRPD. XRPD patterns were collected on a Stoe Stadi P diffractometer (Cu-K_{α1}, Ge (111)) in Debye-Scherrer geometry. The sample was measured inside a sealed glass capillary (1.0 mm) that was spun for improved particle statistics.

The powder patterns were analyzed by Rietveld⁴² and Pawley⁴³ refinement using the range from 2–30° 2θ with TOPAS V5, while keeping the atom coordinates fixed. The peak profile was described by applying the fundamental parameter⁴⁴ approach as implemented in TOPAS. The background was modeled with a 6th order Chebyshev polynomial. Lattice parameters were refined as constrained by the symmetry. The peak broadening was modeled with asymmetry adopted phenomenological model for microstrain⁴⁵. The plotted XRPD patterns were normalized to compare relative peak intensities.

ssNMR. The ssNMR spectra were recorded on a Bruker Avance III 400 MHz spectrometer ($B_0 = 9.4$ T) at the frequencies of 400.1, 100.6 and 40.8 MHz, for ¹H, ¹³C and ¹⁵N, respectively. The ssNMR experiments were performed on a Bruker double resonance 4 mm MAS probe with the COF samples packed in ZrO₂ rotors. The ¹H-¹³C and ¹H-¹⁵N cross-polarization (CP) MAS spectra were recorded with a rotation frequency of 10–12 kHz using a ramped-amplitude (RAMP) spin-locking pulse on the proton channel. The contact time for both nuclei was set to 5 ms, which was found to be optimal. The recycle delay in the CP-experiments was 2 s, defined primarily by the spin-lattice relaxation of protons. All solid-state experiments were carried out using SPINAL64 composite-pulse proton decoupling with radio frequency power between 70 and 80 kHz. The reported ¹H and ¹³C chemical shifts were referenced to tetramethylsilane (TMS), while the ¹⁵N shifts were referenced to nitromethane.

Quantum-chemical calculations. Atom positions and lattices of periodic structures were optimized on PBE-D3/def2-TZVP^{46,47} level of theory using an acceleration scheme based on the resolution of the identity (RI) technique and the continuous fast multipole method (CFMM)⁴⁸ in a developer version of Turbomole⁴⁹.

The CFMM uses multipole moments of maximum order 20 together with a well-separateness value 3 and a basis function extent threshold of 10⁻⁹ a.u. Grid 7 was used for the numerical integration of the exchange-correlation term. The norm of the gradient was converged to 10⁻⁴ a.u. and the total energy is converged to 10⁻⁸ Hartree within the structure optimization using an equidistant 5 × 5 k-point grid.

NMR chemical shifts were obtained on B97-2/pcS-2//PBE-D3/def2-TZVP level of theory^{46,47,50,51} using the Turbomole program package in version 7.0.2 for geometries and the FermiONS++^{52,53} program package for the calculation of NMR chemical shifts performed on excised sections (Supplementary Figs. 3, 4;

distinction shown in Supplementary Fig. 5) of the TTT- and TTI-COF models. Chemical shifts were then referenced to the experimentally obtained spectra with the triazine peak 1/1' and 6,6'.

Data availability. All relevant data are available from the authors upon reasonable request.

Received: 21 December 2017 Accepted: 8 May 2018

Published online: 03 July 2018

References

1. Cote, A. P. et al. Porous, crystalline, covalent organic frameworks. *Science* **310**, 1166–1170 (2005).
2. Waller, P. J. et al. Chemical conversion of linkages in covalent organic frameworks. *J. Am. Chem. Soc.* **138**, 15519–15522 (2016).
3. Dalapati, S. et al. An azine-linked covalent organic framework. *J. Am. Chem. Soc.* **135**, 17310–17313 (2013).
4. Haase, F. et al. Tuning the stacking behaviour of a 2D covalent organic framework through non-covalent interactions. *Mater. Chem. Front.* **1**, 1354–1361 (2017).
5. Ding, S. Y. et al. Construction of covalent organic framework for catalysis: Pd/COF-LZU1 in Suzuki-Miyaura coupling reaction. *J. Am. Chem. Soc.* **133**, 19816–19822 (2011).
6. Kandambeth, S. et al. Construction of crystalline 2D covalent organic frameworks with remarkable chemical (acid/base) stability via a combined reversible and irreversible route. *J. Am. Chem. Soc.* **134**, 19524–19527 (2012).
7. Mazur, M. et al. Synthesis of 'unfeasible' zeolites. *Nat. Chem.* **8**, 58–62 (2016).
8. Hu, X.-Y. et al. Transforming a chemically labile [2 + 3] imine cage into a robust carbamate cage. *Chem. Commun.* **53**, 8616–8619 (2017).
9. Haase, F., Banerjee, T., Savasi, G., Ochsenfeld, C. & Lotsch, B. V. Structure-property-activity relationships in a pyridine containing azine-linked covalent organic framework for photocatalytic hydrogen evolution. *Faraday Discuss.* **201**, 247–264 (2017).
10. Spitzer, E. L. et al. A 2D covalent organic framework with 4.7-nm pores and insight into its interlayer stacking. *J. Am. Chem. Soc.* **133**, 19416–19421 (2011).
11. Liu, Y. et al. Weaving of organic threads into a crystalline covalent organic framework. *Science* **351**, 365–369 (2016).
12. Kandambeth, S. et al. Self-templated chemically stable hollow spherical covalent organic framework. *Nat. Commun.* **6**, 6786 (2015).
13. Lukose, B., Kuc, A. & Heine, T. The structure of layered covalent-organic frameworks. *Chem. Eur. J.* **17**, 2388–2392 (2011).
14. Alahakoon, S. B. et al. Experimental and theoretical insight into the effect of fluorine substituents on the properties of azine linked covalent organic frameworks. *CrystEngComm* **19**, 4882–4885 (2017).
15. Bertrand, G. H. V., Michaelis, V. K., Ong, T.-C., Griffin, R. G. & Dinca, M. Thiophene-based covalent organic frameworks. *Proc. Natl Acad. Sci. USA* **110**, 4923–4928 (2013).
16. Zwaneveld, N. A. et al. Organized formation of 2D extended covalent organic frameworks at surfaces. *J. Am. Chem. Soc.* **130**, 6678–6679 (2008).
17. Gutzler, R. et al. Surface mediated synthesis of 2D covalent organic frameworks: 1,3,5-tris(4-bromophenyl)benzene on graphite(001), Cu(111), and Ag(110). *Chem. Commun.* **29**, 4456–4458 (2009).
18. Vicarelli, L., Heerema, S. J., Dekker, C. & Zandbergen, H. W. Controlling defects in graphene for optimizing the electrical properties of graphene nanodevices. *ACS Nano* **9**, 3428–3435 (2015).
19. Lau, W. L. et al. Rational design of carbon nitride photocatalysts by identification of cyanamide defects as catalytically relevant sites. *Nat. Commun.* **7**, 12165 (2016).
20. Patwardhan, S., Kocherzhenko, A. A., Grozema, F. C. & Siebbeles, L. D. A. Delocalization and mobility of charge carriers in covalent organic frameworks. *J. Phys. Chem. C* **115**, 11768–11772 (2011).
21. Chandra, S. et al. Phosphoric acid loaded azo (–N=N–) based covalent organic framework for proton conduction. *J. Am. Chem. Soc.* **136**, 6570–6573 (2014).
22. Du, Y. et al. Ionic covalent organic frameworks with spiroborate linkage. *Angew. Chem. Int. Ed. Engl.* **55**, 1737–1741 (2016).
23. Vyas, V. S. et al. Exploiting noncovalent interactions in an imine-based covalent organic framework for quercetin delivery. *Adv. Mater.* **28**, 8749–8754 (2016).
24. Xu, H., Gao, J. & Jiang, D. Stable, crystalline, porous, covalent organic frameworks as a platform for chiral organocatalysts. *Nat. Chem.* **7**, 905–912 (2015).
25. Qian, C. et al. Toward covalent organic frameworks bearing three different kinds of pores: the strategy for construction and COF-to-COF transformation via heterogeneous linker exchange. *J. Am. Chem. Soc.* **139**, 6736–6743 (2017).
26. Stewart, D. et al. Stable and ordered amide frameworks synthesised under reversible conditions which facilitate error checking. *Nat. Commun.* **8**, 1102 (2017).
27. Böttcher, B. & Bauer, F. Über die Einwirkung von Schwefel auf Schiffsbasen. *Justus Liebigs Ann. Chem.* **568**, 218–227 (1950).
28. Rabbani, M. G., Islamoglu, T. & El-Kaderi, H. M. Benzothiazole- and benzoxazole-linked porous polymers for carbon dioxide storage and separation. *J. Mater. Chem. A* **5**, 258–265 (2017).
29. Zhu, X. et al. Thiazolothiazole-linked porous organic polymers. *Chem. Commun.* **50**, 15055–15058 (2014).
30. Soñnicki, J. G., Jagodziński, T. S., Nowak-Wydra, B. & Hansen, P. E. Complete assignment of 1H and 13C NMR spectra and conformational analysis of thioamide cannabinoids. *Magn. Reson. Chem.* **34**, 667–674 (1996).
31. Stegbauer, L. et al. Tunable water and CO₂ sorption properties in isostructural azine-based covalent organic frameworks through polarity engineering. *Chem. Mater.* **27**, 7874–7881 (2015).
32. Leng, W. et al. Sophisticated design of covalent organic frameworks with controllable bimetallic docking for a cascade reaction. *Chem. Eur. J.* **22**, 9087–9091 (2016).
33. Vyas, V. S. et al. A tunable azine covalent organic framework platform for visible light-induced hydrogen generation. *Nat. Commun.* **6**, 8508 (2015).
34. Zhang, J. et al. Nitrogen ligands in two-dimensional covalent organic frameworks for metal catalysis. *Chin. J. Catal.* **37**, 468–475 (2016).
35. Mullangi, D. et al. Low-overpotential electrocatalytic water splitting with noble-metal-free nanoparticles supported in a sp³ N-rich flexible COF. *Adv. Energy Mater.* **6**, 1600110 (2016).
36. Egerton, R. F., Li, P. & Malac, M. Radiation damage in the TEM and SEM. *Micron* **35**, 399–409 (2004).
37. Huang, P. Y. et al. Grains and grain boundaries in single-layer graphene atomic patchwork quilts. *Nature* **469**, 389–392 (2011).
38. Smith, B. J., Overholts, A. C., Hwang, N. & Dichtel, W. Insight into the crystallization of amorphous imine-linked polymer networks to 2D covalent organic frameworks. *Chem. Commun.* **52**, 3690–3693 (2016).
39. Nguyen, V. & Gruenwald, M. Microscopic origins of poor crystallinity in the synthesis of covalent organic framework COF-5. *J. Am. Chem. Soc.* **140**, 3306–3311 (2018).
40. Gutzler, R. & Perepichka, D. F. pi-Electron conjugation in two dimensions. *J. Am. Chem. Soc.* **135**, 16585–16594 (2013).
41. Fang, Q. et al. 3D Microporous base-functionalized covalent organic frameworks for size-selective catalysis. *Angew. Chem. Int. Ed.* **53**, 2878–2882 (2014).
42. Rietveld, H. A profile refinement method for nuclear and magnetic structures. *J. Appl. Crystallogr.* **2**, 65–71 (1969).
43. Pawley, G. Unit-cell refinement from powder diffraction scans. *J. Appl. Crystallogr.* **14**, 357–361 (1981).
44. Coelho, A. Whole-profile structure solution from powder diffraction data using simulated annealing. *J. Appl. Crystallogr.* **33**, 899–908 (2000).
45. Stephens, P. Phenomenological model of anisotropic peak broadening in powder diffraction. *J. Appl. Crystallogr.* **32**, 281–289 (1999).
46. Perdew, J. P., Burke, K. & Ernzerhof, M. Generalized gradient approximation made simple. *Phys. Rev. Lett.* **77**, 3865–3868 (1996).
47. Grimme, S., Antony, J., Ehrlich, S. & Krieg, H. A consistent and accurate ab initio parametrization of density functional dispersion correction (DFT-D) for the 94 elements H-Pu. *J. Chem. Phys.* **132**, 154104 (2010).
48. Łazarski, R., Burów, A. M., Grajciar, L. & Sierka, M. Density functional theory for molecular and periodic systems using density fitting and continuous fast multipole method: analytical gradients. *J. Comput. Chem.* **37**, 2518–2526 (2016).
49. TURBOMOLE (Developer version based on version V7.1 2017). University of Karlsruhe and Forschungszentrum Karlsruhe GmbH, 1989–2007, TURBOMOLE GmbH, since 2007. Available at <http://www.turbomole.com>.
50. Wilson, P. J., Bradley, T. J. & Tozer, D. J. Hybrid exchange-correlation functional determined from thermochemical data and ab initio potentials. *J. Chem. Phys.* **115**, 9233–9242 (2001).
51. Jensen, F. Segmented contracted basis sets optimized for nuclear magnetic shielding. *J. Chem. Theory Comput.* **11**, 132–138 (2015).
52. Kussmann, J. & Ochsenfeld, C. Preselective screening for linear-scaling exact exchange-gradient calculations for graphics processing units and general strong-scaling massively parallel calculations. *J. Chem. Theory Comput.* **11**, 918–922 (2015).
53. Kussmann, J. & Ochsenfeld, C. Pre-selective screening for matrix elements in linear-scaling exact exchange calculations. *J. Chem. Phys.* **138**, 134114 (2013).

Acknowledgements

We would like to thank Marie-Luise Schreiber for help in the synthesis of precursor materials and for elemental analysis, Claudia Kamella for EDX measurements, Igor Moudrakovski for measuring the ssNMR and Kerstin Gottschling for performing the sorption measurements. This work has been funded by the Federal Ministry of Education and Research (BMBF, Germany) in the project StickLiS (FKZ: 03XP0030C). B.V.L. acknowledges financial support by an ERC Starting Grant (project COFLeaf, grant number 639233), the Max Planck Society as well as by the Cluster of Excellence Nanosystems Initiative Munich (NIM, DFG) and the Center for Nanoscience (CeNS). C. O. is grateful for financial support by the Cluster of Excellence CIPSM (EXC114, DFG).

Author contributions

F.H. synthesized the precursors and the TTI-COF, interpreted all the data, lead the project, and wrote the manuscript. E.T. performed the sulfur loading experiments. T.B. synthesized PBI-COF, helped in data interpretation, and writing of the manuscript. V.D. recorded the TEM and SAED data. G.S., M.M.J.G., A.M.B., and C.O. performed the quantum-chemical calculations. S.D., S.K., and B.V.L. proposed the idea, initiated the project, and supervised the research. All authors wrote and commented on the manuscript.

Additional information

Supplementary Information accompanies this paper at <https://doi.org/10.1038/s41467-018-04979-y>.

Competing interests: The authors declare no competing interests.

Reprints and permission information is available online at <http://npg.nature.com/reprintsandpermissions/>

Publisher's note: Springer Nature remains neutral with regard to jurisdictional claims in published maps and institutional affiliations.



Open Access This article is licensed under a Creative Commons Attribution 4.0 International License, which permits use, sharing, adaptation, distribution and reproduction in any medium or format, as long as you give appropriate credit to the original author(s) and the source, provide a link to the Creative Commons license, and indicate if changes were made. The images or other third party material in this article are included in the article's Creative Commons license, unless indicated otherwise in a credit line to the material. If material is not included in the article's Creative Commons license and your intended use is not permitted by statutory regulation or exceeds the permitted use, you will need to obtain permission directly from the copyright holder. To view a copy of this license, visit <http://creativecommons.org/licenses/by/4.0/>.

© The Author(s) 2018

3.3 Additional project: Implementation of the periodic electrostatic potential using local basis functions and the continuous fast multipole method

Many empirical methods from computational chemistry are calibrated employing the ESP of density functional theory (DFT) calculations. In order to represent a valuable alternative to other periodic DFT programs from the perspective of many users, it is thus important that TURBOMOLE [73] provides the ESP also in calculations of surfaces and crystals. This section introduces the *electrostatic potential* (ESP) of self-consistent field (SCF) electron densities for molecules and solids in the RIPER program using atom-centered Gaussian-type orbitals (GTOs) and the *continuous fast multipole method* (CFMM) from section 2.2. The implemented method evaluates the ESP on a given set of sampling points. Using grids which adequately grow as $\mathcal{O}(N)$ with system size N , the computational demand for evaluation of the ESP exhibits an asymptotically linear scaling ($\mathcal{O}(N)$). In addition, this approach yields a well-defined ESP for 0D-2D periodic systems. The ESP of 3D systems is obtained by using an additional dipole correction (see section 2.2.4) and thus is determined up to a constant potential shift that depends on quadrupole moments of the unit cell. The ESP implementation employs already implemented techniques in RIPER such as the CFMM, sparse density matrix storage, and prescreening of shell pairs (see section 2.2) [25, 27]. This method extends the conventional ESP implementation provided in the RIDFT program and may enable COSMO implementations [36, 37] for tubes, surfaces, and solids.

The *electrostatic potential*(ESP) itself is defined as the Coulomb interaction between a positive unit point charge and the charge density of this system (and additional external electric fields) while neglecting polarization [108]. The ESP allows to characterize systems, where electrostatic interactions between subsystems play an important role. One prominent case is the use of ESP maps to identify critical regions of electrophilic nature, e.g., in nanotubes [109, 110]. ESP maps can also be used to align band structures for 3D systems [38, 39] and assist the prescreening of organic molecules for cocrystallization [111, 112] and may help in predicting the stability of organic cations [40]. In biochemistry, the ESP may be used to characterize the nature of the active site in proteins and is thus part of enzyme–substrate docking methods [113]. Calculation of the ESP on surfaces, e.g., isodensity surfaces, van der Waals surfaces, solvent accessible and solvent excluding surfaces is also a crucial step in force field construction [114] and in implicit solvent models such as the polarizable continuum model [115] and the conductor-like screening model [36]. The analysis of covalent bonds may be based on the σ -hole which is defined in terms of the ESP [116] and the strength of hydrogen bonds may be predicted on the basis of ESP data [112, 117]. The ESP can also be used to

derive atomic charges; this was previously demonstrated for 3D crystals using the REPEAT method in CP2K [41].

State of the art

The ESP is a basic feature of virtually every quantum chemistry package. Periodic implementations based on plane wave basis sets are, e.g., available in VASP [23, 93], ABINIT [118], and CPMD [119–121]. The periodic ESP is also available from methods based exclusively on local atom-centered basis functions, e.g., CRYSTAL [122, 123], BAND(ADF) [124, 125], DMol³ [126], SIESTA [127, 128], FHI-aims [91], FreeON [102]. A mixed Gaussian Plane wave hybrid scheme is used in CP2K [41, 129, 130] and PYSCF [131]. In contrast to these methods, (1) the periodic DFT implementation in TURBOMOLE still does not provide the ESP, and (2) the molecular ESP implementation in the conventional TURBOMOLE programs exhibits a quadratic scaling of the computational cost with increasing system size provided that the ESP sampling grid grows linearly with system size. The implementation of ESP in RIPER is not based on fundamentally new methods compared to other DFT implementations based on GTOs but TURBOMOLE’s ESP functionality will be again state of the art. This will be mainly accomplished by the use of CFMM from RIPER [27], which will lead to a linear scaling of the ESP evaluation in TURBOMOLE. This ESP evaluation will not make use of the fit density, as it was not optimized for electrostatic potential on every point in space but for total Coulomb energy [24].

Theory

The ESP calculation takes place after a converged electron density ρ is obtained from the self-consistent field (SCF) procedure. A test version of the ESP for all numbers of periodic dimensions in RIPER already exists. It supports the xyz and cube file outputs.

The ESP without any external fields and external charges is defined as

$$V(\mathbf{R}_P) = \underbrace{- \int \frac{\rho_0(\mathbf{r})}{|\mathbf{r} - \mathbf{R}_P|} d^3r}_{\text{density-point-interaction}} + \underbrace{\sum_A \frac{Z_A}{|\mathbf{R}_A - \mathbf{R}_P|}}_{\text{nuclei-point-interaction}} \left(+ \underbrace{\mathbf{R}_P \times \mathbf{E}}_{\text{field-point-interaction}} + \underbrace{\sum_Q \frac{Z_Q}{|\mathbf{R}_Q - \mathbf{R}_P|}}_{\text{add. charges}} \right), \quad (3.1)$$

where R_P represents a position on the sampling grid for the Dirac delta function δ_P as point probe charge. \mathbf{E} is a generic electric field and Z_A the charge of atom A . Along periodic directions, the grid is only defined within a reference unit cell. The electron density of the

crystal is expanded in a set of local GTOs ϕ , [27, 28]

$$\rho_0(\mathbf{r}) = \sum_{\mathbf{L}} \rho^{\mathbf{L}}(\mathbf{r}) \text{ with } \rho^{\mathbf{L}}(\mathbf{r}) = \sum_{\mu\nu\sigma\mathbf{L}'} D_{\mu\nu\sigma}^{\mathbf{L}'} \phi_{\mu}^{\mathbf{L}}(\mathbf{r}) \phi_{\nu}^{\mathbf{L}-\mathbf{L}'}(\mathbf{r}) \quad (3.2)$$

employing elements of the density matrix D . μ and ν index basis functions of the reference cell and lattice vectors \mathbf{L} and \mathbf{L}_0 represent cell translations. The spin index for unrestricted calculations is denoted by σ . A similar summation in terms of Dirac delta functions can be written for the nuclear charge distribution ρ_n^{crystal} and thus a total charge distribution for each unit cell may be defined as

$$\rho_{\text{tot}}^{\mathbf{L}} = \rho^{\mathbf{L}} - \rho_n^{\mathbf{L}} \quad (3.3)$$

Since the total charge distribution is charge neutral, the ESP in eq. 3.1 represents a Coulomb interaction between a local probe charge with a lattice sum of a charge neutral distribution. The evaluation of this lattice sum is well-defined and can be evaluated in direct space with published acceleration and corrections schemes. These are the continuous fast multipole method [27–35] (CFMM) and the dipole correction [97, 132, 133], respectively.

Implementation

This ESP implementation adopts the evaluation of the Coulomb lattice sums from the existing density fitting (DF) accelerated CFMM present in RIPER (see section 2.2.5 and 2.2.6) [27]. More precisely, the FORTRAN subroutines for the Coulomb term including interactions between auxiliary basis functions and the total periodic charge distribution may be modified such that Coulomb interactions between local point probe charges P and the total periodic charge distribution from eq 3.1 are calculated. In this implementation, the electron density ρ^{crystal} formed from shell products and the nuclear charges constitute the total uncharged periodic charge distribution, while the charge distribution ρ_n^{crystal} is treated as a local charge distribution of point probe charges in the reference unit cell. Application of the charge projection scheme (see section 2.2.5) is thus not necessary.

The CFMM follows the procedure reviewed in section 2.2.6. It partitions the lattice sum in eq 3.1 into crystal near field (CNF) and crystal far field (CFF) contributions (see figure 3.1). The lattice vectors \mathbf{L} are assigned to the CFF, if the total charge distribution of \mathbf{L} , $\rho_n^{\mathbf{L}}$, is well-separated from the set of probe point charges δ_P within the reference cell, $\mathbf{L} = \mathbf{0}$. Contributions to the CFF are evaluated by a recursive multipole method [31] that scales as $\mathcal{O}(1)$ with the number of grid points and basis functions, N , once the multipole moments of the unit cell are calculated with fast $\mathcal{O}(N)$.

The CNF contributions to the ESP are further decomposed into local far fields and local near fields. In order to achieve this decomposition, a single hierarchical octree of cubic boxes is constructed. The octree encloses only a single unit cell [27]. All basic charge distributions

- | | |
|--|---|
| <p>(a) ESP, CFF contribution (see section 2.2.6)</p> <ul style="list-style-type: none"> • Multipole moments of shellpairs $M[\mu\nu\mathbf{L}] \rightarrow M[\rho_{\text{tot}}^0]$ • Multipole moments of nuclei $M[A] \rightarrow M[\rho_{\text{tot}}^0]$ • If 3D: dipole correction [27, 97] • construct \mathcal{L}^{CFF} • calculate $\mathcal{L}^{\text{CFF}} \otimes M[\rho_{\text{tot}}^0] \rightarrow L[\rho_{\text{tot}}^{\text{CFF}}]$ • Loop ESP point P <ul style="list-style-type: none"> – calculate $M[P]$ – calculate $M[P] \odot L[\rho_{\text{tot}}^{\text{CFF}}] \rightarrow \text{ESP}[P]$ | <p>(b) ESP, CNF contribution (see section 2.2.6)</p> <ul style="list-style-type: none"> • FF contribution <ul style="list-style-type: none"> – octree construction – Pass 1a: calculation of $M[\rho_{\text{tot}}]$ and $M[P]$ – Pass 1b: upward translation of $M[\rho_{\text{tot}}]$ – Pass 2a: local expansion $M2L \odot M[\rho_{\text{tot}}] \rightarrow L[\rho_{\text{tot}}]$ – Pass 2b: downward shift $L2L \odot L[\rho_{\text{tot}}] \rightarrow L_{\text{box}}[\rho_{\text{tot}}]$ – Pass 3: contraction $L_{\text{box}}[\rho_{\text{tot}}] \otimes M[P] \rightarrow V[P]$ • NF contribution (Pass 4, here $\mathbf{L} \in NF$) <ul style="list-style-type: none"> – loop $P^0, \mu\nu\mathbf{L}$: $(P \mu\nu\mathbf{L}) \times D_{\mu\nu\mathbf{L}} \rightarrow V[P]$ – loop P^0, Q^L: $(P Q^L)Z_Q \rightarrow V[P]$ |
|--|---|

Figure 3.1: Algorithm for ESP calculation at the Γ -point ($\mathbf{k} = \mathbf{0}$). $\mu\nu\mathbf{L} \sim \mu_0(\mathbf{r})\nu_0(\mathbf{r} - \mathbf{L})$ indicate screened shellpairs, A nuclei and P ESP grid points. M and L are the multipole and Taylor moments as defined in section 2.2.6. Refer to this chapter for details on the construction of \mathcal{L}^{CFF} , the hierarchical octree, and the multipole to local (M2L) operator and local to local (L2L) operators .

such as point probe charges, nuclear charges, and shell products are sorted into boxes of this single octree. Interactions between charge distributions sorted into well separated boxes of the octree represent contributions to the local far fields. These are evaluated employing multipole expansions. Remaining interactions represent contributions to local near fields and are calculated by recursive integral methods. The use of octree-based CFMM reduces the scaling of the CNF evaluation to $\mathcal{O}(N)$ resulting in an overall $\mathcal{O}(N)$ scaling of the entire ESP calculation. The bottleneck of the calculation is the recursive integral evaluation of shell pairâpoint charge interactions in the local near fields and is implemented OpenMP-parallel. A detailed overview over the algorithm is given in figure 3.1

Computational details

With this ESP prototype version, tests have been performed on molecules and 2D solids. The test results shown are obtained with the functional of Perdew, Burke and Enzerhof (PBE) [134] together with split valence, triple- ζ valence, and quadruple- ζ valence basis sets with polarization functions (SVP, TZVP, and QZVP)[135]. Converged densities are obtained with the RI-SCF method presented in reference [27] using appropriate RI basis sets [136]. For the exchange-correlation term, grid size 7 is used, if not stated otherwise. DFT energies and densities are tightly converged, the FMM well-separateness parameter is set to 3, the basis function extent parameter `epsbext` is set to 10^{-9} , and the radius cutoff criterion for integration partition functions is 50 bohr (see [27] and the TURBOMOLE7.2 manual [137] for further details on these settings). For the tests, the target number of particles per lowest level CFMM box must be raised from 10 to a maximum of 30 particles according to the density of the employed ESP grids that represent particles in the octree. Calculations of crystal far field contributions use a maximum multipole order of 20. All timings were performed on an

Intel Xeon E5-2667 3.2 GHz processors with 25 MB cache and 256 GB memory on a CentOS 7.2 system working with a Samsung SM863 series solid state drive. The code was compiled with the Intel FORTRAN compiler 2015. All calculations were done with a TURBOMOLE developer version.

Results

First, calculations are performed for the A24 set of weakly bound dimers [138] for comparison between the existing molecular ESP in RIDFT and the implementation in RIPER. These calculations use grid 5 for the exchange-correlation term. The molecular ESP grid in RIPER is constructed in analogy to the grids for density plots already available in RIPER. The converged density from RIPER is taken directly for the ESP calculation in RIDFT for comparison. The ESP between RIPER and RIDFT agree within 10^{-8} hartree for calculations employing SVP and TZVP basis sets. As initial validation for periodic systems, the ESP is calculated for selected points in distances ranging from 1.5 to 500 bohr on top of a boron nitride monolayer as depicted in figure 3.2. The convergence of calculated ESP values for different k -point meshes and cell sizes are shown in table 3.1. On each probe point, the ESP converges quickly with the number of k -points for each probe charge. Repeating the calculations for a change of the well-separateness from 3 to 5 does not alter the results beyond 10^{-7} hartree. The scaling of the computational demand of the ESP is shown in figure 3.3 for linear alkanes using QZVP basis sets. Simple alkane models were build using perfect tetrahedral angles, generic C-C bond lengths of 1.54 Å and C-H bond lengths of 1.10 Å. The number of ESP sampling points increases linearly with the number of C atoms by setting each C-atom into a box with a uniform sampling mesh of 30 points perpendicular to and 5 points along the chain direction. As expected for the CFMM method in RIPER, the scaling reduces to $\mathcal{O}(N)$ with a bottleneck in the direct integral evaluation of the local near fields. Steps visible in the graph of figure 3.3 arise due to changes in the octree for growing alkane chain lengths. These steps do not alter the overall $\mathcal{O}(N_P)$ scaling. In contrast, the RIDFT implementation exhibits a quadratic scaling for the ESP calculation. A similar scaling behavior is obtained for RIPER when switching off the CFMM (technically this is done by setting an extremely large local well-separateness locally in the CFMM code). In this ESP prototype implementation, the direct integral evaluation of the electron density–point probe interaction term turns out to be the dominant computational part. Therefore only parallelisation of this term was tested. For a 2D sheet of a TTI-COF [139] and two layers of 200×200 sampling points shown in figure 3.4, speedups of up to 13 are observed, see table 3.2.

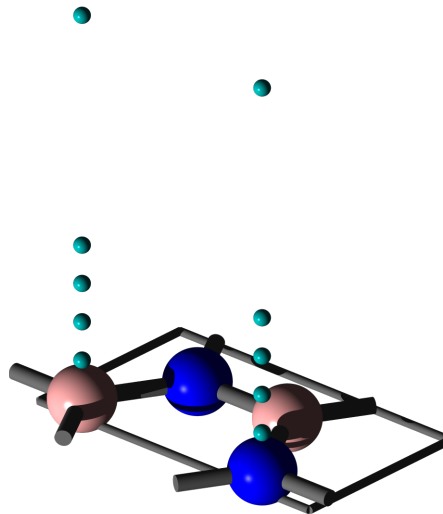


Figure 3.2: 2D unit cell of the boron nitride sheet. The turquoise spheres represent the first ESP points up to $10 b$ above the monolayer.

Table 3.1: Electrostatic potential for the boron nitride cell shown in figure 3.2 and its 3×3 supercell. ΔV_{max} represents the maximum absolute deviation between corresponding ESP probe charges at the described level of accuracy (k -points and cell) and the charges for the 21×21 k -points unit cell.

cell	k -points	ΔV_{max}
1×1	1×1	1.47×10^{-2}
	2×2	1.23×10^{-2}
	3×3	1.21×10^{-3}
	4×4	3.99×10^{-4}
	5×5	2.40×10^{-4}
	6×6	3.10×10^{-5}
	7×7	7.27×10^{-6}
	9×9	2.09×10^{-6}
	10×10	4.70×10^{-7}
	11×11	1.20×10^{-7}
	14×14	1.00×10^{-8}
3×3	1×1	1.21×10^{-3}
	2×2	2.82×10^{-5}

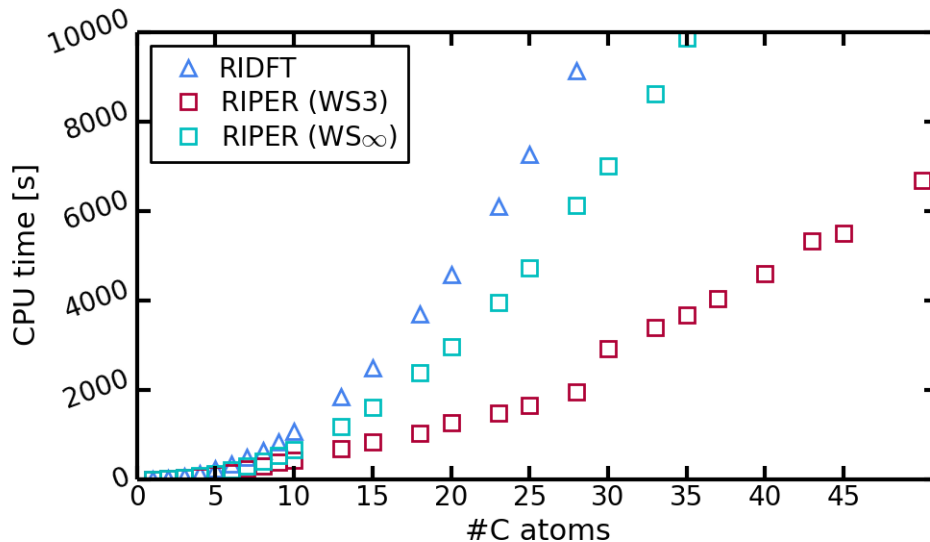


Figure 3.3: CPU time for ESP calculation of linear alkanes. Direct integral evaluation (WS_{∞}) was compared to the FMM (WS_3). Results from the already implemented molecular ESP from RIDFT are plotted for comparison (RIDFT).

Table 3.2: Parallel efficiency for the ESP for the TTI-COF shown in figure 3.4. The first double column V depicts the timings for the complete ESP, the last double column $\sum_{L,P}(P|\rho^L)$ the timings for the probe charge-shell pair interaction.

#cores	V		$\sum_{L,P}(P \rho^L)$	
	CPU time [s]	speedup	CPU time [s]	speedup
1	882.6	1	867.2	1.00
2	448.7	1.97	440.3	1.97
3	301.7	2.93	295.6	2.93
4	227.9	3.88	223.0	3.89
6	157.3	5.61	153.6	5.65
8	121.9	7.24	118.9	7.29
10	100.3	8.80	97.6	8.89
12	87.5	10.09	85.0	10.20
14	78.3	11.27	76.1	11.40
16	66.7	13.23	64.6	13.42

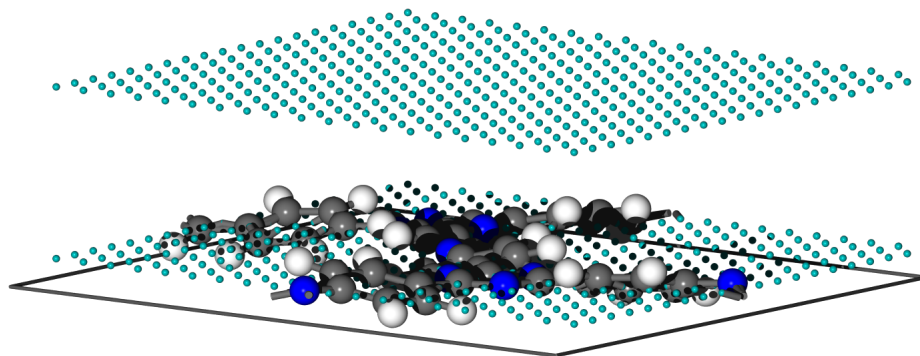


Figure 3.4: 2D unit cell of a sheet of the TTI-COF. The two layers of ESP points are marked by turquoise spheres. Be aware that only every 100th point is plotted within a layer

Conclusion

Some features are still missing. For example basis sets in combination with *effective core potentials* (ECPs) are not supported at the moment. The same is true for binary file format output. Additional testing may be required for 3D systems. The constant shift of the ESP for 3D systems stemming from the dipole correction must as well be addressed, as the 'landscape' of the ESP is returned correctly but not its absolute value. Possible future applications involve the implementation of charge fitting through REPEAT [41] similar to CP2K, periodic force-field calculations employing the COSMO module [36, 37] and fitting of binding strengths. ESP grid evaluation could additionally be done on GPU cores and adjustment for the GPU driven direct integral evaluations should be possible.

4

Conclusion and outlook

This work introduces a robust RPA method to compute ground state energies for molecules and solids on an equal footing. The translation symmetry adapted Hartree kernel in its supermatrix representation is derived using Bloch functions of local, atom-centered Gaussian-type basis functions and resolution of the identity (RI) factorization. The recursive continuous fast multipole method CFMM was modified to allow the calculation of long-range Coulomb sums for irreducible representations different from the Γ -Point. At the Γ -point, charge projection is necessary to avoid divergent terms in the Coulomb Sums from charged basis functions. Overall scaling is $\mathcal{O}(N^4 \log(N))$ with system size N and N_k^2 with the number of reciprocal points k . The calculated models prove that both the Γ -point supercell approach and corresponding wave-vector calculations yield the same results with a significant speedup for the latter method of typically 10-100 times. This method accurately predicts structural parameters of weakly bound dimers and binding energies at the basis set extrapolation CBS limit. The revised CFMM method opens the door for all types of RI-based post-SCF methods under PBCs such as MP2 and coupled cluster, as well as RPA-based approaches like RPA-SOSEX [20, 140, 141].

Additional unpublished work is presented in the form of a scheme for calculation of the periodic electrostatic potential (ESP) for the periodic DFT code RIPER in TURBOMOLE. A proof of concept implementation of the electrostatic potential for the RIPER module in TURBOMOLE is given in this work containing a revised form of the CFMM method. This method is valid and implemented for both molecules and crystals. Overall scaling is, regardless of periodicity, constant for every ESP grid point and scales as $\mathcal{O}(N)$ with system size. It may be used for charge fitting or for COSMO solvation models extended for periodic systems. Test calculations are performed for the A24 set of weakly bound dimers. The ESP between the RIPER and RIDFT implementation agree within 10^{-8} hartree for calculations employing SVP

and TZVP basis sets, verifying the implementation. It may be used for charge fitting as well as COSMO solvation models [36, 37] extended for periodic systems.

The main work of adapting periodic DFT-formalism to RPA was accompanied by characterizing a conversion process of an imine- into a thiazole-linked COF. The examined imine- and thiazole-linked COFs in this work consisted of 2D sheets stacked and kept in place by means of dispersion forces. The examined conversion enables a novel insight into the crystalline nature of the material. The TTT-COF exhibits various structural defects, in particular one-dimensional defects such as edge-dislocations as well as co-aligned COF grains. These defects can be assumed to stem directly from the formation of the TTI-COFS, therefore allowing a deeper insight in the formation process of such COFs, which may be exploited in future synthesis approaches.

Bibliography

- [1] Jensen, F. *Introduction to Computational Chemistry*, 2nd ed.; John Wiley & Sons, Incorporated: Chichester [i.a.], 2007.
- [2] Kohn, W.; Sham, L. J. Self-Consistent Equations Including Exchange and Correlation Effects. *Phys. Rev.* **1965**, *140*, A1133–A1138.
- [3] Parr, W.; Young, R. G. *Density functional theory of atoms and molecules*; Oxford University Press: New York, 1994.
- [4] Engel, E.; Dreizler, R. M. In *Density functional theory*; Beiglböck, W., Chrusciel, P., Eckmann, J.-P., Grosse, H., Kupiainen, A., Löwen, H., Loss, M., Nekrasov, N. A., Salmhofer, M., Smirnov, S., Takhtajan, L., Yngvason, J., Eds.; Springer-Verlag Berlin Heidelberg: Heidelberg [i.a.], 2011.
- [5] Eschrig, H. *The Fundamentals of Density Functional Theory*, 2nd ed.; Eag.Le, Ed. am Gutenbergplatz: Leipzig, 2003.
- [6] Helgaker, T.; Jørgensen, P.; Olsen, J. *Molecular Electronic-Structure Theory*; John Wiley & Sons, LTD: Chichester [i.a.], 2000.
- [7] Ullrich, C. A. *Time-Dependent Density-Functional Theory - Concepts and Applications*; Oxford University Press: Oxford, 2012.
- [8] Bohm, D.; Pines, D. A Collective Description of Electron Interactions. I. Magnetic Interactions. *Phys. Rev.* **1951**, *82*, 625–634.
- [9] Pines, D.; Bohm, D. A Collective Description of electron interactions: II. Collective vs Individual Particle Aspects of the Interactions. *Phys. Rev.* **1952**, *85*, 338–353.
- [10] Bohm, D.; Pines, D. A Collective Description of Electron Interactions. III. Coulomb Interactions in a Degenerate Electron Gas. *Phys. Rev.* **1953**, *92*, 609–625.
- [11] Furche, F. On the density matrix based approach to time-dependent density functional response theory. *J. Chem. Phys.* **2001**, *114*, 5982–5992.
- [12] Fetter, A. L.; Walecka, J. D. *Quantum theory of many-particle systems*; Dover Publications: Mineola, NY, 1971.

- [13] Schurkus, H. F. Highly Accurate Random Phase Approximation Methods With Linear Time Complexity. Ph.D. thesis, LMU Munich, 2017.
- [14] Giuliani, G. F.; Vignale, G. *Quantum Theory of the Electron Liquid*, 1st ed.; Cambridge University Press: New York, 2005.
- [15] Kaltak, M.; Klimeš, J.; Kresse, G. Low Scaling Algorithms for the Random Phase Approximation: Imaginary Time and Laplace Transformations. *J. Chem. Theory Comput.* **2014**, *10*, 2498–2507.
- [16] Kaltak, M.; Klimeš, J.; Kresse, G. Cubic scaling algorithm for the random phase approximation: Self-interstitials and vacancies in Si. *Phys. Rev. B* **2014**, *90*, 054115.
- [17] Ramalho, J. P. P.; Gomes, J. R. B.; Illas, F. Accounting for van der Waals interactions between adsorbates and surfaces in density functional theory based calculations: selected examples. *RSC Adv.* **2013**, *3*, 13085.
- [18] Grimme, S. Semiempirical GGA-Type Density Functional Constructed with a Long-Range Dispersion Correction. *J. Comput. Chem.* **2006**, *27*, 1787–1799.
- [19] Grimme, S.; Antony, J.; Ehrlich, S.; Krieg, H. A consistent and accurate ab initio parametrization of density functional dispersion correction (DFT-D) for the 94 elements H-Pu. *J. Chem. Phys.* **2010**, *132*, 154104.
- [20] Chen, G. P.; Voora, V. K.; Agee, M. M.; Balasubramani, S. G.; Furche, F. Random-Phase Approximation Methods. *Annu. Rev. of Physical Chem.* **2017**, *68*, 421–445.
- [21] Ashcroft, N. W.; Mermin, N. D. *Solid State Physics*; Thomson Learning, 1976.
- [22] Jones, W.; March, N. H. *Theoretical Solid State Physics Volume 1*; Dover Publications, Inc.: New York, 1973.
- [23] Kresse, G.; Furthmüller, J. Efficient iterative schemes for *ab initio* total-energy calculations using a plane-wave basis set. *Phys. Rev. B* **1996**, *54*, 11169–11186.
- [24] Burow, A. M.; Sierka, M.; Mohamed, F. Resolution of identity approximation for the Coulomb term in molecular and periodic systems. *J. Chem. Phys.* **2009**, *131*, 214101.
- [25] Burow, A. M.; Sierka, M. Linear Scaling Hierarchical Integration Scheme for the Exchange-Correlation Term in Molecular and Periodic Systems. *J. Chem. Theory Comput.* **2011**, *7*, 3097–3104.
- [26] Grajciar, L. Low-Memory Iterative Density Fitting. *J. Comput. Chem.* **2015**, *36*, 1521–1535.

- [27] Łazarski, R.; Burow, A. M.; Sierka, M. Density Functional Theory for Molecular and Periodic Systems Using Density Fitting and Continuous Fast Multipole Methods. *J. Chem. Theory Comput.* **2015**, *11*, 3029–3041.
- [28] Łazarski, R.; Burow, A. M.; Grajciar, L.; Sierka, M. Density Functional Theory for Molecular and Periodic Systems Using Density Fitting and Continuous Fast Multipole Method: Analytical Gradients. *J. Comput. Chem.* **2016**, *37*, 2518–2526.
- [29] White, C. A.; Head-Gordon, M. Derivation and efficient implementation of the fast multipole method. *J. Chem. Phys.* **1994**, *101*, 6593–6605.
- [30] White, C. A.; Johnson, B. G.; Gill, P. M. W.; Head-Gordon, M. The continuous fast multipole method. *Chem. Phys. Lett.* **1994**, *230*, 8–16.
- [31] Kudin, K. N.; Scuseria, G. E. Revisiting infinite lattice sums with the periodic fast multipole method. *J. Chem. Phys.* **2004**, *121*, 2886–2890.
- [32] Kudin, K. N.; Scuseria, G. E. Linear-scaling density-functional theory with Gaussian orbitals and periodic boundary conditions: Efficient evaluation of energy and forces via the fast multipole method. *Phys. Rev. B* **2000**, *61*, 16440–16453.
- [33] Kudin, K. N.; Scuseria, G. E. A fast multipole method for periodic systems with arbitrary unit cell geometries. *Chem. Phys. Lett.* **1998**, *283*, 61–68.
- [34] Kudin, K. N.; Scuseria, G. E. A fast multipole algorithm for the efficient treatment of the Coulomb problem in electronic structure calculations of periodic systems with Gaussian orbitals. *Chem. Phys. Lett.* **1998**, *289*, 611–616.
- [35] Challacombe, M.; White, C.; Head-Gordon, M. Periodic boundary conditions and the fast multipole method. *J. Chem. Phys.* **1997**, *107*, 10131–10140.
- [36] Klamt, A.; Schüürmann, G. COSMO: A New Approach to Dielectric Screening in Solvents with Explicit Expressions for the Screening Energy and its Gradient. *J. Chem. Soc. Perkin Trans. 2* **1993**, *2*, 799–805.
- [37] Tomasi, J.; Persico, M. Molecular Interactions in Solution: An Overview of Methods Based on Continuous Distributions of the Solvent. *Chem. Rev.* **1994**, *94*, 2027–2094.
- [38] Hellström, M.; Spångberg, D.; Hermansson, K.; Broqvist, P. Band-filling Correction Method for Accurate Adsorption Energy Calculations: A Cu/ZnO Case Study. *J. Chem. Theory Comput.* **2013**, *9*, 4673–4678.
- [39] Butler, K. T.; Hendon, C. H.; Walsh, A. Electronic Chemical Potentials of Porous Metal-Organic Frameworks. *J. Am. Chem. Soc.* **2014**, *136*, 2703–2706.

- [40] Robbins, A. M.; Jin, P.; Brinck, T.; Murray, J. S.; Politzer, P. Electrostatic Potential as a Measure of Gas Phase Carbocation Stability. *Int. J. Quantum Chem.* **2006**, *106*, 2904–2909.
- [41] Campañá, C.; Mussard, B.; Woo, T. K. Electrostatic Potential Derived Atomic Charges for Periodic Systems Using a Modified Error Functional. *J. Chem. Theory Comput.* **2009**, *5*, 2866–2878.
- [42] Furche, F. Molecular tests of the random phase approximation to the exchange-correlation energy functional. *Phys. Rev. B* **2001**, *64*, 195120.
- [43] Furche, F.; Van Voorhis, T. Fluctuation-dissipation theorem density-functional theory. *J. Chem. Phys.* **2005**, *122*, 164106.
- [44] Furche, F. Developing the random phase approximation into a practical post-Kohn-Sham correlation model. *J. Chem. Phys.* **2008**, *129*, 114105.
- [45] Eshuis, H.; Yarkony, J.; Furche, F. Fast computation of molecular random phase approximation correlation energies using resolution of the identity and imaginary frequency integration. *J. Chem. Phys.* **2010**, *132*, 234114.
- [46] Eshuis, H.; Furche, F. Basis set convergence of molecular correlation energy differences within the random phase approximation. *J. Chem. Phys.* **2012**, *136*, 084105.
- [47] Eshuis, H.; Bates, J. E.; Furche, F. Electron correlation methods based on the random phase approximation. *Theor. Chem. Acc.* **2012**, *131*, 1084.
- [48] Bates, J. E.; Furche, F. Communication: Random phase approximation renormalized many-body perturbation theory. *J. Chem. Phys.* **2013**, *139*, 171103.
- [49] Burow, A. M.; Bates, J. E.; Furche, F.; Eshuis, H. Analytical First-Order Molecular Properties and Forces within the Adiabatic Connection Random Phase Approximation. *J. Chem. Theory Comput.* **2014**, *10*, 180–194.
- [50] Burow, A. M. *Lecture Notes*; 2019.
- [51] Dobson, J. F. Dispersion (Van Der Waals) Forces and TDDFT. *Lect. Notes Phys.* **2006**, *706*, 443–462.
- [52] Langreth, D. C.; Perdew, J. P. The exchange-correlation energy of a metallic surface. *Solid State Commun.* **1975**, *17*, 1425–1429.
- [53] Langreth, D. C.; Perdew, J. P. Exchange-correlation energy of a metallic surface: Wave-vector analysis. *Phys. Rev. B* **1977**, *15*, 2884–2901.

- [54] Gunnarsson, O.; Lundqvist, B. I. Exchange and correlation in atoms, molecules, and solids by the spin-density-functional formalism. *Phys. Rev. B* **1976**, *13*, 4274–4298.
- [55] Szabo, A.; Ostlund, N. S. *Modern Quantum Chemistry: Introduction to Advanced Electronic Structure Theory*; Dover Publications, Inc.: New York, 1996.
- [56] Gross, E. K. U.; Kohn, W. Time-Dependent Density Functional Theory. *Adv. Quantum Chem.* **1990**, *21*, 255–291.
- [57] Marques, M. A. L., Maitra, N. T., Nogueira, F. M. S., Gross, E. K. U., Rubio, A., Eds. *Fundamentals of Time-Dependent Density Functional Theory*; Lect. Notes Phys.; 2012; Vol. 837.
- [58] Gross, E. K. U.; Kohn, W. Local Density-Functional Theory of Frequency-Dependent Linear Response. *Phys. Rev. Lett.* **1985**, *55*, 2850–2852.
- [59] Petersilka, M.; Gossmann, U. J.; Gross, E. K. U. Excitation Energies from Time-Dependent Density-Functional Theory. *Phys. Rev. Lett.* **1996**, *76*, 1212–1215.
- [60] Lein, M.; Gross, E. K. U.; Perdew, J. Electron correlation energies from scaled exchange-correlation kernels: Importance of spatial versus temporal nonlocality. *Phys. Rev. B* **2000**, *61*, 13431–13437.
- [61] Callen, H. B.; Welton, T. A. Irreversibility and Generalized Noise. *Phys. Rev.* **1951**, *83*, 34–40.
- [62] Freitag, E.; Busam, R. *Complex Analysis*, 2nd ed.; Springer-Verlag Berlin Heidelberg: Heidelberg, 2009.
- [63] Wilhelm, J.; Seewald, P.; Del Ben, M.; Hutter, J. Large-Scale Cubic-Scaling Random Phase Approximation Correlation Energy Calculations Using a Gaussian Basis. *J. Chem. Theory Comput.* **2016**, *12*, 5851–5859.
- [64] Gell-Mann, M.; Brueckner, K. A. Correlation Energy of an Electron Gas at High Density. *Phys. Rev.* **1957**, *106*, 364–368.
- [65] Chen, G. P.; Agee, M. M.; Furche, F. Performance and Scope of Perturbative Corrections to Random-Phase Approximation Energies. *J. Chem. Theory Comput.* **2018**, *14*, 5701–5714.
- [66] Onida, G.; Reining, L.; Rubio, A. Electronic excitations: density-functional versus many-body Green's-function approaches. *Rev. Mod. Phys.* **2002**, *74*, 601–659.

- [67] Salpeter, E. E.; Bethe, H. A. A Relativistic Equation for Bound-State Problems. *Phys. Rev.* **1951**, *84*, 1232–1242.
- [68] Freeman, D. L. Coupled-cluster expansion applied to the electron gas: Inclusion of ring and exchange effects. *Phys. Rev. B* **1977**, *15*, 5512–5521.
- [69] Scuseria, G. E.; Henderson, T. M.; Sorensen, D. C. The ground state correlation energy of the random phase approximation from a ring coupled cluster doubles approach. *J. Chem. Phys.* **2008**, *129*, 231101.
- [70] Raghavachari, K.; Trucks, G. W.; Pople, J. A.; Head-Gordon, M. A Fifth-Order Perturbation Comparison Of Electron Correlation Theories. *Chem. Phys. Lett.* **1989**, *157*, 479–483.
- [71] Srinivasadesikan, V.; Raghunath, P.; Lin, M. C. Quantum chemical investigation on the role of Li adsorbed on anatase (101) surface nano-materials on the storage of molecular hydrogen. *J. Mol. Model.* **2015**, *21*, 142.
- [72] Gao, J.; Zheng, Y.; Tang, Y.; Jehng, J.-M.; Grybos, R.; Handzlik, J.; Wachs, I. E.; Podkolzin, S. G. Spectroscopic and Computational Study of CR Oxide Structures and Their Anchoring Sites on ZSM-5 Zeolites. *ACS Catal.* **2015**, *5*, 3078–3092.
- [73] TURBOMOLE, development of the University of Karlsruhe and Forschungszentrum Karlsruhe GmbH, 1989-2007, TURBOMOLE GmbH, since 2007.
- [74] Kratzer, P.; Neugebauer, J. The Basics of Electronic Structure Theory for Periodic Systems. *Front. Chem.* **2019**, *7*, 106.
- [75] Burow, A. M. Methoden zur Beschreibung von chemischen Strukturen beliebiger Dimensionalität mit der Dichtefunktionaltheorie unter periodischen Randbedingungen. Ph.D. thesis, Humboldt-Universität zu Berlin, 2011.
- [76] Sierka, M.; Hogeckamp, A.; Ahlrichs, R. Fast evaluation of the Coulomb potential for electron densities using multipole accelerated resolution of identity approximation. *J. Chem. Phys.* **2003**, *118*, 9136–9148.
- [77] Eichkorn, K.; Treutler, O.; Öhm, H.; Häser, M.; Ahlrichs, R. Auxiliary basis sets to approximate Coulomb potentials. *Chem. Phys. Lett.* **1995**, *240*, 283–289.
- [78] Vahtras, O.; Almlöf, J.; Feyereisen, M. W. Integral approximations for LCAO-SCF calculations. *Chem. Phys. Lett.* **1993**, *213*, 514–518.
- [79] Hohenberg, P.; Kohn, W. Inhomogeneous Electron Gas. *Phys. Rev.* **1964**, *136*, B864 – B871.

- [80] Bloch, F. Über die Quantenmechanik der Elektronen in Kristallgittern. *Zeitschrift für Phys.* **1929**, *52*, 555–600.
- [81] Blöchl, P. E. Projector augmented-wave method. *Phys. Rev. B* **1994**, *50*, 17953–17979.
- [82] Payne, M. C.; Teter, M. P.; Allan, D. C.; Arias, T. A.; Joannopoulos, J. D. Iterative minimization techniques for *ab initio* total-energy calculations: Molecular dynamics and conjugate gradients. *Rev. Mod. Phys.* **1992**, *64*, 1045–1097.
- [83] Kresse, G.; Hafner, J. Norm-conserving and ultrasoft pseudopotentials for first-row and transition elements. *J. Phys. Condens. Matter* **1994**, *6*, 8245–8257.
- [84] Kresse, G.; Joubert, D. From ultrasoft pseudopotentials to the projector augmented-wave method. *Phys. Rev. B* **1999**, *59*, 1758–1775.
- [85] Vanderbilt, D. Soft self-consistent pseudopotentials in a generalized eigenvalue formalism. *Phys. Rev. B* **1990**, *41*, 7892–7895.
- [86] Pisani, C.; Dovesi, R.; Roetti, C. In *Lect. notes Chem.*; Berthier, G., Dewar, M. J. S., Fischer, H., Fukui, K., Hall, G. G., Hinze, J., Jáffe, H. H., Jortner, J., Kutzelnigg, W., Ruedenberg, K., Tomasi, J., Eds.; Springer-Verlag: Berlin [i.a.], 1988; Vol. 48.
- [87] Tosoni, S.; Tuma, C.; Sauer, J.; Civalleri, B.; Ugliengo, P. A comparison between plane wave and Gaussian-type orbital basis sets for hydrogen bonded systems: Formic acid as a test case. *J. Chem. Phys.* **2007**, *127*, 154102.
- [88] Grüneich, A.; Heß, B. A. Choosing GTO basis sets for periodic HF calculations. *Theor. Chem. Acc.* **1998**, *100*, 253–263.
- [89] Peintinger, M. F.; Oliveira, D. V.; Bredow, T. Consistent Gaussian Basis Sets of Triple-Zeta Valence with Polarization Quality for Solid-State Calculations. *J. Comput. Chem.* **2013**, *34*, 451–459.
- [90] Köster, A. M.; Del Campo, J. M.; Janetzko, F.; Zuniga-Gutierrez, B. A MinMax self-consistent-field approach for auxiliary density functional theory. *J. Chem. Phys.* **2009**, *130*, 114106.
- [91] Blum, V.; Gehrke, R.; Hanke, F.; Havu, P.; Havu, V.; Ren, X.; Reuter, K.; Scheffler, M. *Ab initio* molecular simulations with numeric atom-centered orbitals. *Comput. Phys. Commun.* **2009**, *180*, 2175–2196.
- [92] Schütt, O.; VandeVondele, J. Machine Learning Adaptive Basis Sets for Efficient Large Scale DFT Simulation. *J. Chem. Theory Comput.* **2018**, *14*, 4168–4175.

- [93] Kresse, G.; Furthmüller, J. Efficiency of ab-initio total energy calculations for metals and semiconductors using a plane-wave basis set. *Comput. Mater. Sci.* **1996**, *6*, 15–50.
- [94] Dovesi, R.; Orlando, R.; Erba, A.; Zicovich-Wilson, C. M.; Civalleri, B.; Casassa, S.; Maschio, L.; Ferrabone, M.; De La Pierre, M.; D’Arco, P.; Noël, Y.; Causà, M.; Rérat, M.; Kirtman, B. CRYSTAL14: A Program for the *Ab Initio* Investigation of Crystalline Solids. *Int. J. Quantum Chem.* **2014**, *114*, 1287–1317.
- [95] Monkhorst, H. J.; Pack, J. D. Special points for Brillouin-zone integrations. *Phys. Rev. B* **1976**, *13*, 5188–5192.
- [96] Pack, J. D.; Monkhorst, H. J. "Specials points for Brillouin-zone integration" – a reply. *Phys. Rev. B* **1977**, *16*, 1748–1749.
- [97] Stolarczyk, L. Z.; Piela, L. Direct Calculation of Lattice Sums. A Method to Account for the Crystal Field Effects. *Int. J. Quantum Chem.* **1982**, *22*, 911–927.
- [98] Eichkorn, K.; Weigend, F.; Treutler, O.; Ahlrichs, R. Auxiliary basis sets for main row atoms and transition metals and their use to approximate Coulomb potentials. *Theor. Chem. Acc.* **1997**, *97*, 119–124.
- [99] Irmeler, A.; Burow, A. M.; Pauly, F. Robust Periodic Fock Exchange with Atom-Centered Gaussian Basis Sets. *J. Chem. Theory Comput.* **2018**, *14*, 4567–4580.
- [100] Sundararaman, R.; Arias, T. A. Regularization of the Coulomb singularity in exact exchange by Wigner-Seitz truncated interactions: Towards chemical accuracy in nontrivial systems. *Phys. Rev. B* **2013**, *87*, 165122.
- [101] Guidon, M.; Hutter, J.; VandeVondele, J. Robust Periodic Hartree-Fock Exchange for Large-Scale Simulations Using Gaussian Basis Sets. *J. Chem. Theory Comput.* **2009**, *5*, 3010–3021.
- [102] Tymczak, C. J.; Challacombe, M. Linear scaling computation of the Fock matrix. VII. Periodic density functional theory at the Γ point. *J. Chem. Phys.* **2005**, *122*, 134102.
- [103] Baerends, E.; Ellis, D.; Ros, P. Self-consistent molecular Hartree-Fock-Slater calculations I. The computational procedure. *Chem. Phys.* **1973**, *2*, 41–51.
- [104] Dunlap, B. I.; Connolly, J. W. D.; Sabin, J. R. On some approximations in applications of $X\alpha$ theory. *J. Chem. Phys.* **1979**, *71*, 3396–3402.
- [105] Oliveira, D. V.; Laun, J.; Peintinger, M. F.; Bredow, T. BSSE-Correction Scheme for Consistent Gaussian Basis Sets of Double- and Triple-Zeta Valence with Polarization Quality for Solid-State Calculations. *J. Comput. Chem.* **2019**, *40*, 2364–2376.

- [106] Dunlap, B. I. Robust and variational fitting: Removing the four-center integrals from center stage in quantum chemistry. *J. Mol. Struct. THEOCHEM* **2000**, 529, 37–40.
- [107] White, C. A.; Head-Gordon, M. Fractional tiers in fast multipole method calculations. *Chem. Phys. Lett.* **1996**, 257, 647–650.
- [108] Levine, I. N. In *Quantum Chemistry*, 7th ed.; Jaworski, A., Ed.; Pearson: Boston, 2014; p 700 ff.
- [109] Dinadayalane, T. C.; Murray, J. S.; Concha, M. C.; Politzer, P.; Leszczynski, J. Reactivities of Sites on (5,5) Single-Walled Carbon Nanotubes with and without a Stone-Wales Defect. *J. Chem. Theory Comput.* **2010**, 6, 1351–1357.
- [110] Wang, D.-L.; Xu, H.-L.; Hu, Y. Y.; Su, Z.-M. Comparative study of the electrostatic potential of perfect and defective single-walled carbon nanotubes. *Comput. Theor. Chem.* **2011**, 966, 1–8.
- [111] Musumeci, D.; Hunter, C. A.; Prohens, R.; Scuderi, S.; McCabe, J. F. Virtual cocrystal screening. *Chem. Sci.* **2011**, 2, 883–890.
- [112] Aakeröy, C. B.; Epa, K.; Forbes, S.; Schultheiss, N.; Desper, J. Ranking Relative Hydrogen-Bond Strengths in Hydroxybenzoic Acids for Crystal-Engineering Purposes. *Chem. - A Eur. J.* **2013**, 19, 14998–15003.
- [113] Kavitha, T.; Velraj, G. Molecular structure, spectroscopic and docking analysis of 1,3-diphenylpyrazole-4-propionic acid: A good prostaglandin reductase inhibitor. *J. Mol. Struct.* **2018**, 1155, 819–830.
- [114] Walker, R. C.; Crowley, M. F.; Case, D. A. The Implementation of a Fast and Accurate QM/MM Potential Method in Amber. *J. Comput. Chem.* **2009**, 29, 1019–1031.
- [115] Miertuš, S.; Scrocco, E.; Tomasi, J. Electrostatic interaction of a solute with a continuum. A direct utilization of ab initio molecular potentials for the prevision of solvent effects. *J. Chem. Phys.* **1981**, 55, 117–129.
- [116] Politzer, P.; Murray, J. S.; Clark, T.; Resnati, G. The σ -hole revisited. *Phys. Chem. Chem. Phys.* **2017**, 19, 32166–32178.
- [117] Aakeröy, C. B.; Wijethunga, T. K.; Desper, J. Molecular electrostatic potential dependent selectivity of hydrogen bonding. *New J. Chem.* **2015**, 39, 822–828.
- [118] Gonze, X. et al. Recent developments in the ABINIT software package. *Comput. Phys. Commun.* **2016**, 205, 106–131.

- [119] CPMD, copyright IBM Corp 1990-2017, copyright MPI für Festkörperforschung Stuttgart 1997-2001, <http://www.cpmd.org/>.
- [120] Hirshfeld, F. L. Bonded-Atom Fragments for Describing Molecular Charge Densities. *Theor. Chim. Acta* **1977**, *44*, 129–138.
- [121] Singh, U. C.; Kollman, P. A. An Approach to Computing Electrostatic Charges for Molecules. *J. Comput. Chem.* **1984**, *5*, 129–145.
- [122] Erba, A.; Baima, J.; Bush, I.; Orlando, R.; Dovesi, R. Large-Scale Condensed Matter DFT Simulations: Performance and Capabilities of the CRYSTAL Code. *J. Chem. Theory Comput.* **2017**, *13*, 5019–5027.
- [123] CRYSTAL17, Dovesi, R. and Saunders, V. R. and Roetti, C. and Orlando, R. and Zicovich-Wilson, C. M. and Pascale, F. and Civalleri, B. and Doll, K. and Harrison, N. M. and Bush, I. J. and D’Arco, P. and Llunell, M. and Causà, M. and Noël, Y. and Maschio, L. and Erba, A. and Rerat, M. and Casassa, S., University of Torino, Torino, **2017**.
- [124] BAND2017, SCM. Philipsen, P.H.T. Velde, G. te Baerends, E.J. Berger, J.A. Boeij, P.L. de Franchini, M. Groeneveld, J.A. Kadantsev, E.S. Klooster, R. Kootstra, F. Romaniello, P. Raupach, M. Skachkov, D.G. Snijders, J.G. Verzijl, C.J.O. Gil, J.A. Celis Thij, Theoretical Chemistry, Vrije Universiteit, Amsterdam, The Netherlands, **2017**.
- [125] ADF2017, SCM, Baerends, E.J. Ziegler, T. Atkins, A.J. Autschbach, J. Baseggio, O. Bashford, D. Bérces, A. Bickelhaupt, F.M. Bo, C. Boerrigter, P.M. Cavallo, L. Daul, C. Chong, D.P. Chulhai, D.V. Deng, L. Dickson, R.M. Dieterich, J.M. Ellis, D.E. Faassen, M, Theoretical Chemistry, Vrije Universiteit, Amsterdam, The Netherlands, **2017**, <http://www.scm.com>.
- [126] dmol³, Copyright Accelrys Software, Inc., <http://www.accelrys.com>, **2017**.
- [127] Soler, J. M.; Artacho, E.; Gale, J. D.; García, A.; Junquera, J.; Ordejón, P.; Sánchez-Portal, D. The SIESTA method for *ab initio* order-N materials simulation. *J. Phys. Condens. Matter* **2002**, *14*, 2745–2779.
- [128] Artacho, E.; Anglada, E.; Diéguez, O.; Gale, J. D.; García, A.; Junquera, J.; Martín, R. M.; Ordejón, P.; Pruneda, J. M.; Sánchez-Portal, D.; Soler, J. M. The SIESTA method; Developments and applicability. *J. Phys. Condens. Matter* **2008**, *20*, 064208.
- [129] Bayly, C. I.; Cieplak, P.; Cornell, W. D.; Kollman, P. A. A Well-Behaved Electrostatic Potential Based Method Using Charge Restraints for Deriving Atomic Charges: The RESP Model. *J. Phys. Chem.* **1993**, *97*, 10269–10280.

- [130] Golze, D.; Hutter, J.; Iannuzzi, M. Wetting of water on hexagonal boron nitride@Rh(111): a QM/MM model based on atomic charges derived for nano-structured substrates. *Phys. Chem. Chem. Phys.* **2015**, *17*, 14307–14316.
- [131] Sun, Q.; Berkelbach, T. C.; Blunt, N. S.; Booth, G. H.; Guo, S.; Li, Z.; Liu, J.; McClain, J.; Sayfutyarova, E. R.; Sharma, S.; Wouters, S.; Chan, G. K.-L. PYSCF: The Python-based simulations of chemistry framework. *WIREs Comput. Mol. Sci.* **2017**, *8*:e1340, doi: 10.1002/wcms.1340.
- [132] Euwema, R. N.; Surratt, G. T. The absolute positions of calculated energy bands. *J. Phys. Chem. Solids* **1975**, *36*, 67–71.
- [133] Redlack, A.; Grindlay, J. Coulombic Potential Lattice Sums. *J. Phys. Chem. Solids* **1975**, *36*, 73–82.
- [134] Perdew, J. P.; Burke, K.; Ernzerhof, M. Generalized Gradient Approximation Made Simple. *Phys. Rev. Lett.* **1996**, *77*, 3865–3868.
- [135] Weigend, F.; Ahlrichs, R. Balanced basis sets of split valence, triple zeta valence and quadruple zeta valence quality for H to Rn: Design and assessment of accuracy. *Phys. Chem. Chem. Phys.* **2005**, *7*, 3297–3305.
- [136] Weigend, F. Accurate Coulomb-fitting basis sets for H to Rn. *Phys. Chem. Chem. Phys.* **2006**, *8*, 1057–1065.
- [137] TURBOMOLE 7.2, development of the University of Karlsruhe and Forschungszentrum Karlsruhe GmbH, 1989-2007, TURBOMOLE GmbH, since 2007.
- [138] Āezáč, J.; Hobza, P. Describing Noncovalent Interactions beyond the Common Approximations: How Accurate is the "Gold Standard," CCSD(T) at the Complete Basis Set Limit? *J. Chem. Theory Comput.* **2013**, *9*, 2151–2155.
- [139] Haase, F.; Gottschling, K.; Stegbauer, L.; Germann, L. S.; Gutzler, R.; Duppel, V.; Vyas, V. S.; Kern, K.; Dinnebier, R. E.; Lotsch, B. V. Tuning the stacking behaviour of a 2D covalent organic framework through non-covalent interactions. *Mater. Chem. Front.* **2017**, *1*, 1354–1361.
- [140] Grüneis, A.; Marsman, M.; Harl, J.; Schimka, L.; Kresse, G. Making the random phase approximation to electronic correlation accurate. *J. Chem. Phys.* **2009**, *131*, 154115.
- [141] Ángyán, J. G.; Liu, R.-F.; Toulouse, J.; Jansen, G. Correlation Energy Expressions from the Adiabatic-Connection Fluctuation–Dissipation Theorem Approach. *J. Chem. Theory Comput.* **2011**, *7*, 3116–3130.